Sister Rod Destructive Examinations (FY20)

Appendix F: Cyclic Integrated Reversible-Bending Fatigue Tests

Spent Fuel and Waste Disposition

Rose Montgomery,
Jy-An Wang, Hong Wang,
Bruce Bevard,
Darren Skitt, Oscar Martinez

SUMMARY

This report documents work performed under the Spent Fuel and Waste Disposition's Spent Fuel and Waste Science and Technology program for the US Department of Energy (DOE) Office of Nuclear Energy (NE). This work was performed to fulfill Level 2 Milestone M2SF-21OR010201032, "ORNL High Burnup Confirmatory Demo Sibling Rod Testing Results," within work package SF-21OR01020103 and is an update to the work reported in M2SF-19ORO010201026 and M2SF-19OR010201028.

As a part of DOE NE High Burnup Spent Fuel Data Project, Oak Ridge National Laboratory (ORNL) is performing destructive examinations (DEs) of high burnup (HBU) (>45 GWd/MTU) spent nuclear fuel (SNF) rods from the North Anna Nuclear Power Station operated by Dominion Energy. The SNF rods, called *sister rods* or *sibling rods*, are all HBU and include four different kinds of fuel rod cladding: standard Zircaloy-4 (Zirc-4), low-tin (LT) Zirc-4, ZIRLO, and M5. The DEs are being conducted to obtain a baseline of the HBU rod's condition before dry storage and are focused on understanding overall SNF rod strength and durability. Composite fuel and defueled cladding will be tested to derive material properties. Although the data generated can be used for multiple purposes, one primary goal for obtaining the post-irradiation examination data and the associated measured mechanical properties is to support SNF dry storage licensing and relicensing activities by (1) addressing identified knowledge gaps and (2) enhancing the technical basis for post-storage transportation, handling, and subsequent disposition.

This appendix documents the status of the ORNL Phase 1 DE activities related to tests of the sister rods using the Cyclic Integrated Reversible-Bending Fatigue Tester (CIRFT) in Phase 1 of the sister rod test program.

Table FS-1 provides the status of the CIRFT tests.

Table FS-1. DE.05 status.

Planned DE		P.I.	Status	Comments
DE.05	Perform CIRFT tests to determine static, dynamic, and cumulative effects and fatigue lifetime	J. A. Wang	In progress	Thirty-one tests using CIRFT were completed on 25 specimens. The preliminary results indicate that the baseline sister rod's fatigue lifetime is consistent with other rods of the same type that were tested in the past. The 17 × 17 sister rods fall on the lower side of the existing CIRFT database. The heat treatments applied to selected rods resulted in a shorter fatigue lifetime due to reduced flexural rigidity.
				The flexural rigidity measured for the baseline sister rods is consistent with, although on the lower side of, previously tested 17 × 17 specimens for M5-, ZIRLO-, and LT Zirc-4 clad specimens. The heat-treated rods have a lower flexural rigidity than the corresponding baseline rod, except the Zirc-4 clad specimens, which have a higher flexural rigidity possibly related to the

Planned DE	P.I.	Status	Comments
			design's longer pellet length. Since the results of the Zirc-4-clad rod are inconsistent with other sister rods, it is recommended that at least two more confirmatory tests be completed using Zirc-4-clad heat-treated specimens from F35P17.
			A test on a specimen with a grid-to-rod-fretting mark in the maximum strain location did not result in a reduced fatigue lifetime.
			One test remains to be completed on a specimen that has multiple pellet-pellet gaps. The specimen will be tested to determine whether the gaps have an impact on the fatigue lifetime.
			The cumulative effects test fixture is being evaluated out-of-cell.
Post-test imaging and dogbone characterization	Skitt	Complete	All completed test pairs characterized.
Finite element modeling of selected performance characteristics	Martinez	In progress	Modeling of the cumulative impact test to determine the appropriate fixture configuration is complete and indicates that applying an impact to a specimen mounted in a dogbone yield an impact load that is too high. If cumulative effects tests will be completed, then a different application must be researched.
			Simulations of flexural rigidity, pellet-pellet, pellet-clad bonding is underway to better understand test results and provide prediction capability.

ACKNOWLEDGMENTS

This page intentionally blank

CONTENTS

This page is intentionally blank

LIST OF FIGURES

LIST OF TABLES

This page is intentionally left blank.

REVISION HISTORY

Date	Changes
3/29/2019	Initial release
9/27/2019	Revised to include additional data and incorporate comments from the previously released report.
10/29/2020	The CIRFT detailed report was moved to Appendix F and updated to include the most recent information.
11/30/2020	Comments received on the draft were incorporated and the document numbering revised to reflect its M2 status.

This page is intentionally left blank.

ACRONYMS

ASME	American Society of Mechanical Engineers
BWR	boiling water reactor
CIRFT	cyclic integrated reversible-bending fatigue tester
DE	destructive examination
DOE	US Department of Energy
FEA	finite element analysis
FHT	full-length fuel rod heat treatment
GTRF	grid-to-rod fretting
HBU	high burnup
ID	inner diameter
LSTC	Livermore Software Technology Corporation
LT	low tin
NDE	nondestructive examination
NE	Office of Nuclear Energy
NRC	US Nuclear Regulatory Commission
OD	outer diameter
ORNL	Oak Ridge National Laboratory
PWR	pressurized water reactor
SNF	spent nuclear fuel

This page is intentionally left blank.

F-1. Introduction

Spent nuclear fuel (SNF) assemblies must be shipped to other sites for processing and disposal. During shipment, the fuel is typically oriented horizontally, and the fuel rods are subject to periodic alternating loads related to the movement of the vehicle that results in alternating bending of the SNF fuel rods. The number of bending cycles is related to the length of the shipping route with longer routes producing more cycles. Because it is well-known that cyclic loads can produce failures even when the stress and strain imposed are below the yield point of the material, investigating the SNF fatigue behavior is prudent.

This report discusses the results of fatigue testing at Oak Ridge National Laboratory (ORNL) using the Cyclic Integrated Reversible-Bending Fatigue Tester (CIRFT) created by the US Department of Energy (DOE) Office of Nuclear Energy (NE) for the High Burnup Spent Fuel Data Project and its sister rods [F-1, F-2, F-3]. The results of the tests are compared with results obtained over the last decade using the same CIRFT for the US Nuclear Regulatory Commission (NRC).

F-2. CIRFT Description

The CIRFT, shown in Figure F- 1, is hardware developed by ORNL [F-4, F-5] to test the fatigue lifetime of spent nuclear fuel (SNF) in postulated normal transportation vibration conditions. The machine oscillates 6-inch segments of high burnup SNF until fatigue failure occurs. The CIRFT uses a U-frame with two rigid arms that converts the motor's linear motion into a bending moment exerted on the rod segment. The two U-frame arms are driven by two electromagnetic-force–based motors. The motors (Bose model LM2) have a maximum load capacity of ±3,000 N and a maximum stroke of ±25.6 mm.

Each tested SNF segment is fitted with special end grips called "dogbones," which are epoxied onto both ends of the segment. When prepared this way, the SNF segment is referred to as a *dogbone*. The epoxy provides a compliant layer—in which thickness depends on the dimensions of the dogbone and segment—that is important in ensuring pure bending. When the dogbone is engaged with the U-frame, bending is imposed by the motor through the U-frame, as illustrated Figure F- 2, with a cycle defined as follows: the dogbone (1) begins in the neutral position (i.e., no bending), (2) is flexed laterally away from the front face of the machine, (3) is returned to the neutral position, (4) is flexed laterally toward the front face of the machine, and (5) is returned to the neutral position. The CIRFT can flex the rod specimen at 5–10 Hz during the dynamic test, with the sister rod tests performed at 5 Hz.

To ensure the desired motion, the CIRFT is specifically configured to test SNF rod segments that have diameters between 9.70 to 11.74 mm with a fixed segment length of 152.40 mm (6 in.). The test's gauge section is the 50.80 mm (2 in.) SNF rod length between the dogbones in which the maximum bending deflection occurs.

To date, two types of tests are performed: a static test and a dynamic test. A third test, the cumulative effects test, is still in the equipment development stage. The *dynamic test* is the standard fatigue test performed on the CIRFT. The SNF segment is flexed at a fixed frequency and motor stroke length until fracture is detected and the number of cycles is recorded. For the *static* test, the segment is flexed very slowly (0.05 Hz) to the maximum stroke of the machine, and the deflection is measured. The static test does not result in fracture of the specimen because the machine cannot impose enough deflection to cause fracture. Although the static test can be followed by a dynamic test, the flexure imposed during the static test is much higher than that imposed during the dynamic test, and the large deflection may reduce the flexural rigidity and fatigue lifetime, as discussed in later sections of this appendix. The cumulative test will impose impacts on the SNF segment before performing a dynamic test and is meant to determine whether periodic impacts of the rod with other rods or the packaging during transport are detrimental to the fatigue lifetime.
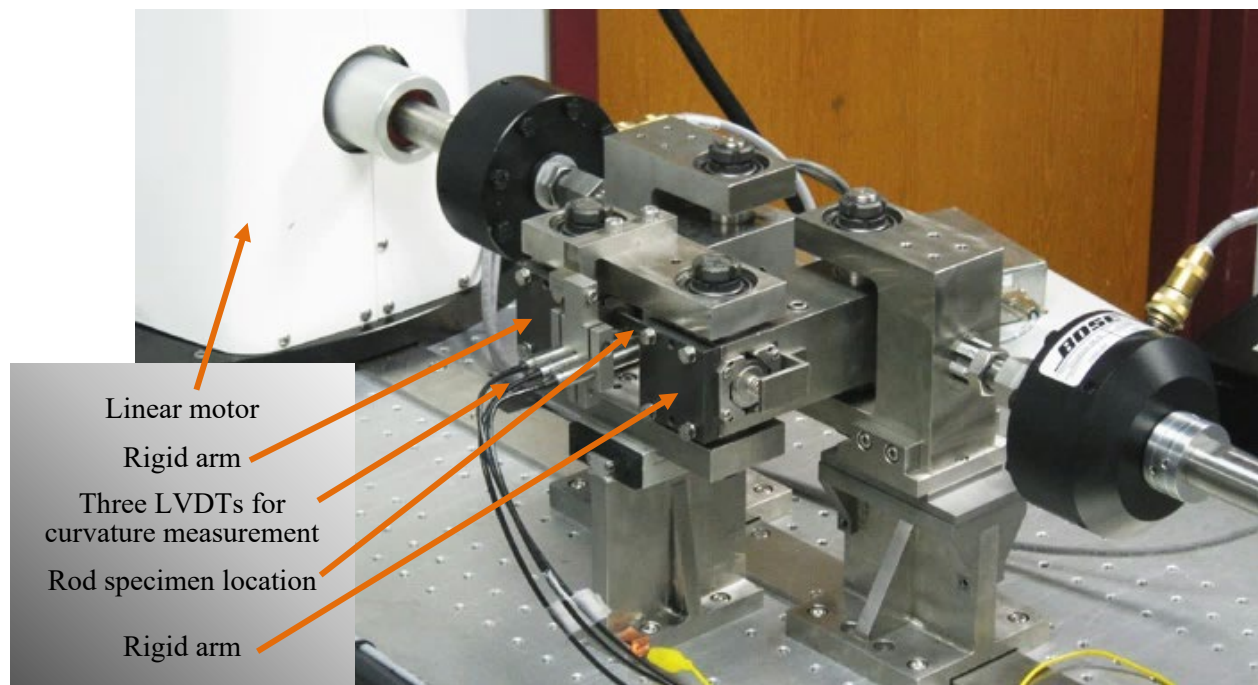
(a)
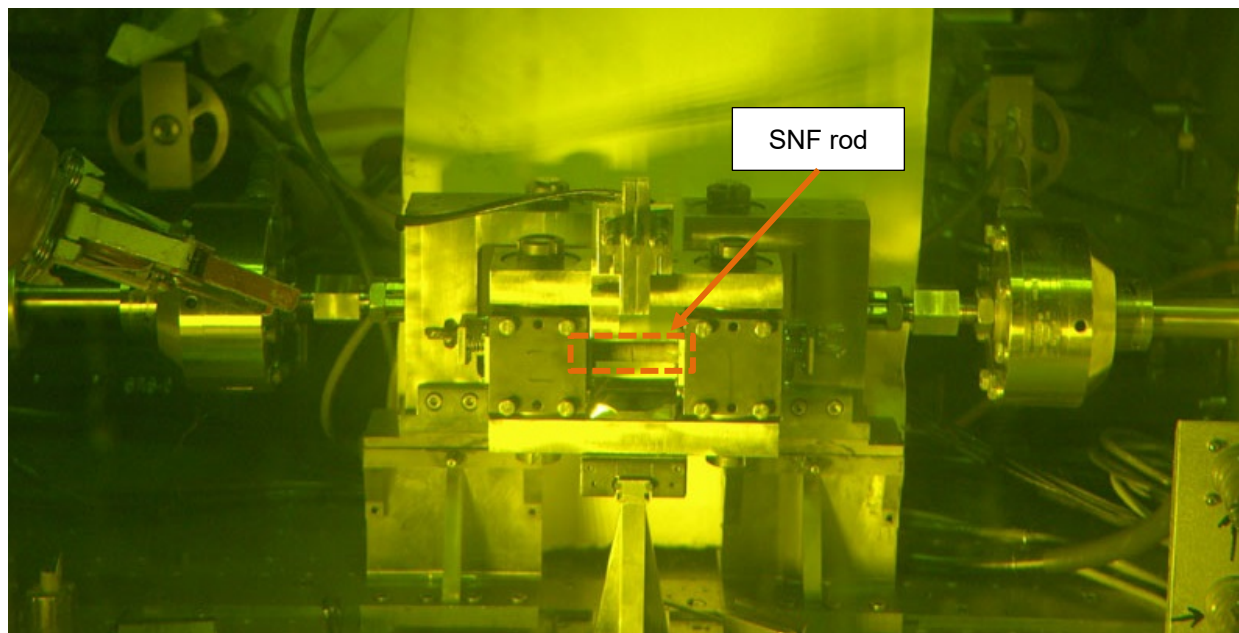
(b)

Figure F- 1. Two views of the ORNL CIRFT; (a) a surrogate rod specimen undergoing out-of-cell testing with three linear variable differential transducers (LVDTs) in place of curvature measurements and (b) an SNF rod being tested in the hot cell.
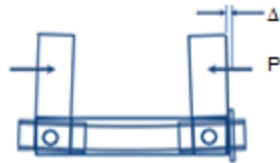
(a) Rigid arms are closing. The curvature is concave outward and designated with a negative sign.
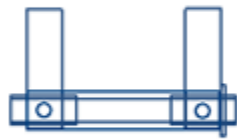
(b) Rigid arms are in neutral position.
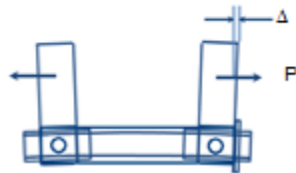
(c) Rigid arms are opening. The curvature concave inward and designated with a positive sign.

Figure F- 2. Schematic drawings of U-frame setup for reversal bending when rigid arms are (a) closing, (b) neutral, and (c) opening.

F-3. Data Acquisition, Data Processing, Basic Information, and Extended Information

This section summarizes the full discussion provided by Wang and Wang [F-4, F-5]. The key data acquired during the CIRFT test include the number of cycles to failure and the bending moment imposed. The bending moment is calculated based on the motor stroke length applied (set by the user) and the deflection of the SNF rod segment, which is measured using three LVDTs, as shown in Figure F- 3. A view of one end of a test specimen is shown in Figure F- 3 with the end-block removed, allowing a view of the LVDTs. Online monitoring of the calculated flexural rigidity is used to shut down the machine at the onset of failure.

Three LVDTs for curvature measurement

Linear roller bearing sets (behind the specimen) embedded in the end-face of the rigid arm, enabling free axial movement of specimen

Rod specimen
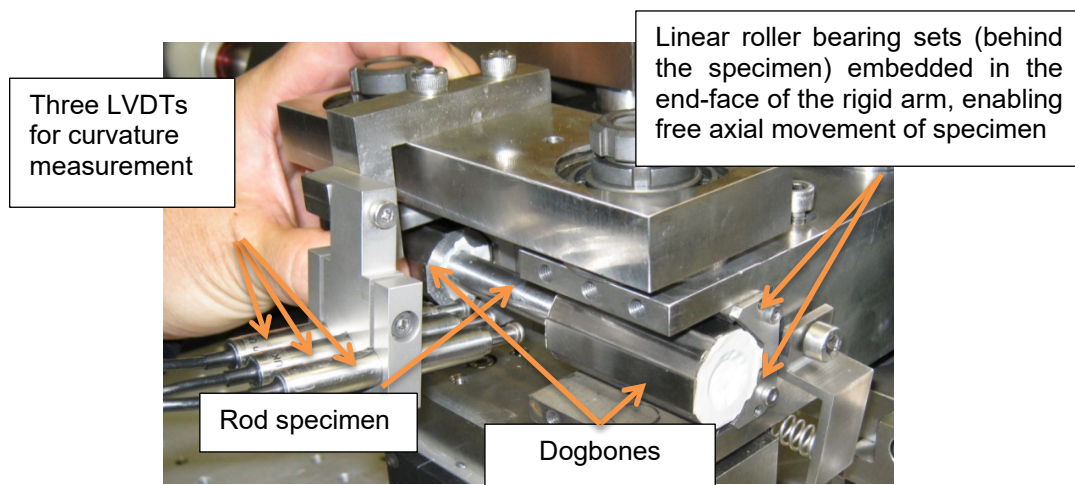
Dogbones

Figure F- 3. Image showing the grip design of CIRFT with one end-block removed.

The distances built into the CIRFT machine and the length of the segment dogbone are important because they are used to calculate all load, moment, and curvature values. Important fixed physical distances include the length of the U-frame arms (101.60 mm) and the location and contact geometry of the LVDTs. Also, the motor's recorded stroke length during the test is directly applied in the data reduction, and the SNF rod outer diameter (OD) is used to calculate strain and stress.
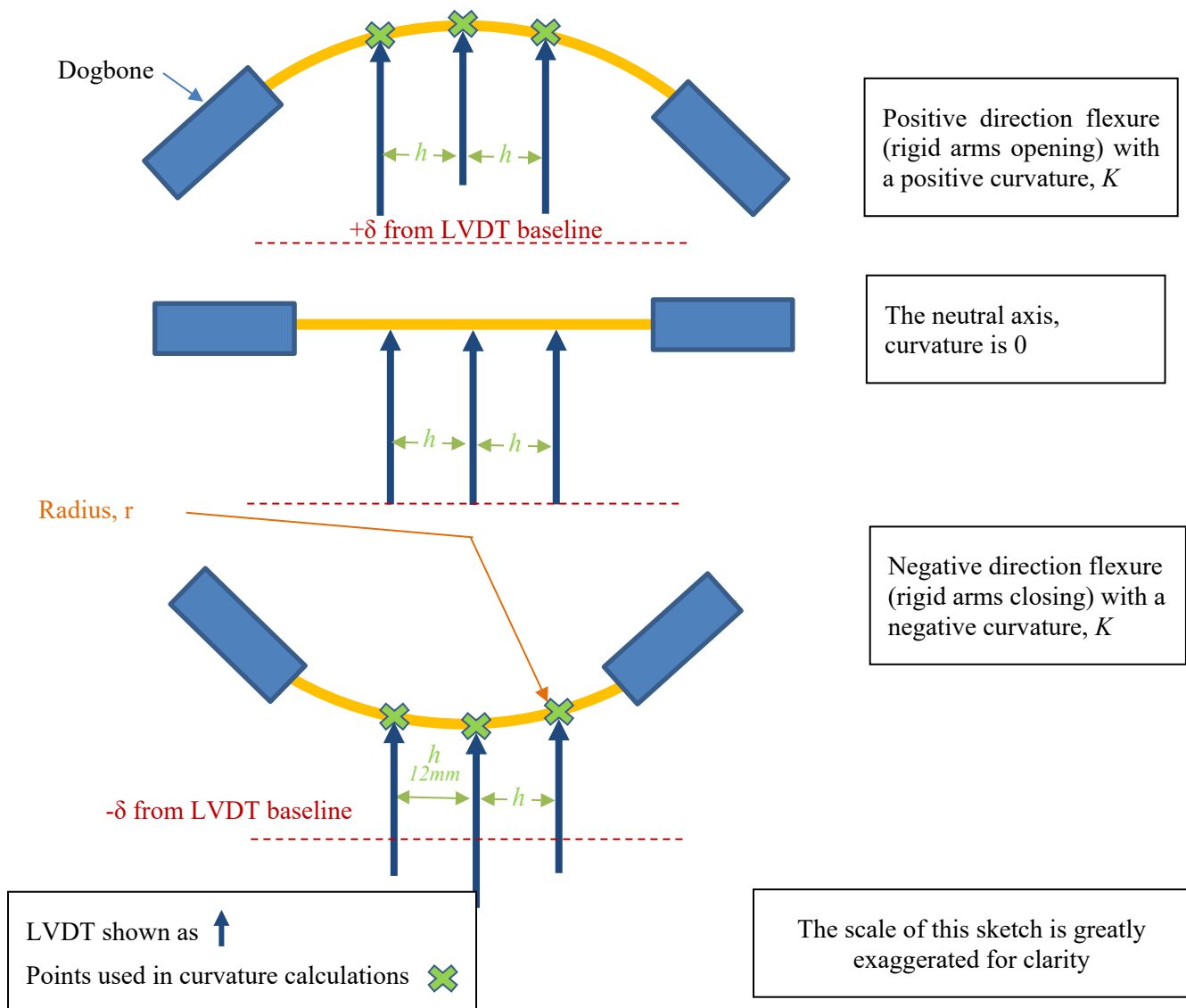
Figure F- 4. The LVDT measurements for the curvature calculation.

The rod curvature, K, is calculated as the inverse of the radius, assuming the SNF segment forms a short circular arc. As illustrated in Figure F- 4, the known spacing between the LVDTs (h, *12 mm*) is used with the measured LVDT deflection to determine the instantaneous curvature of the dogbone gauge section during the test. The raw data are denoised and further adjusted based on the type of LVDT used in the test and any bias observed in the LVDT measurements. An example of the processed data is provided in Figure F- 5.
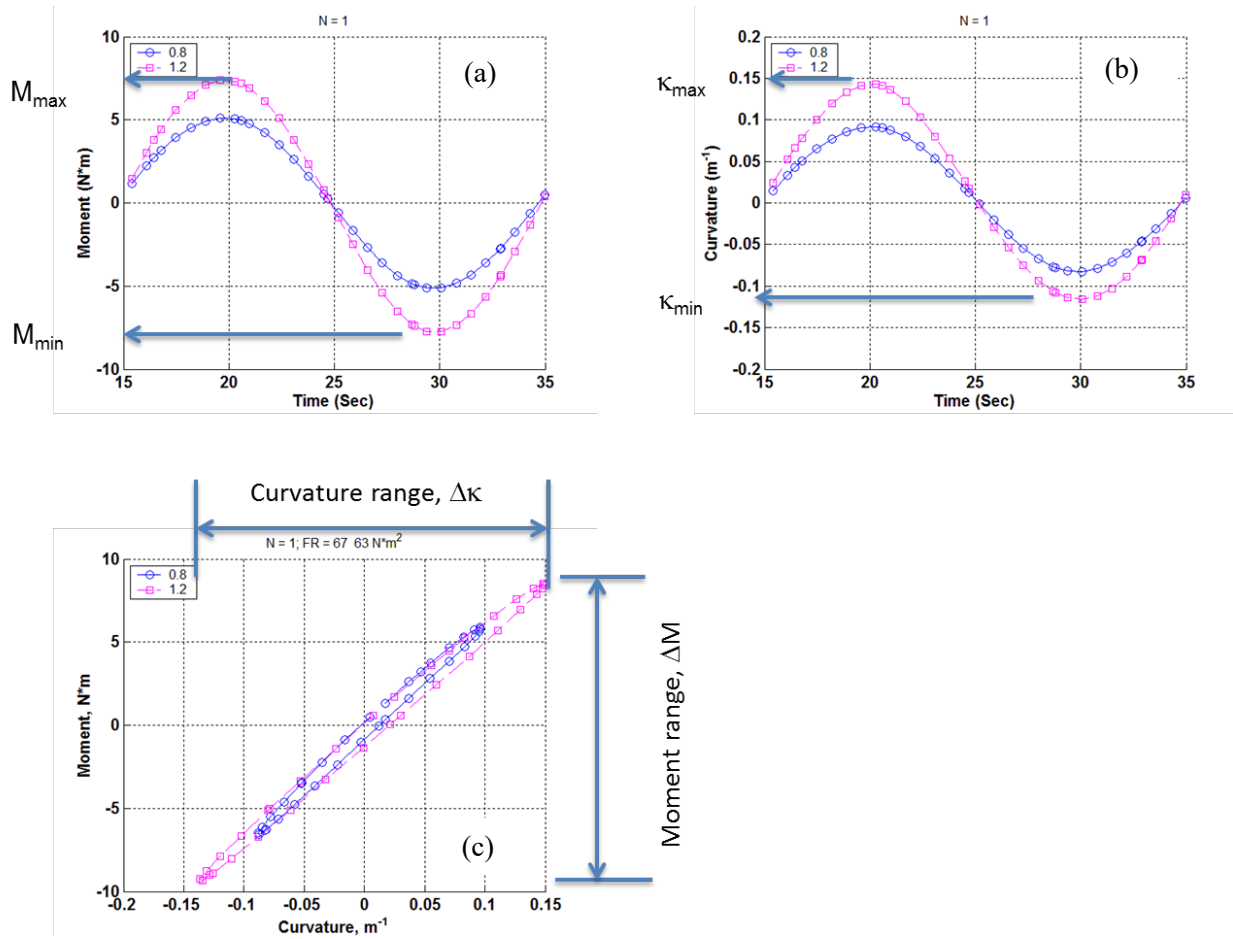
Figure F- 5. An example of a single cycle for two different applied loads showing (a) the instantaneous applied bending moment, (b) the calculated curvature, and (c) the moment-curvature hysteresis loop.

The radius, r, is calculated by determining the physical coordinates described by the measured LVDT deflections d_1, d_2, and d_3 and by scribing them with a circle:

$$\sqrt{(x_o - d_2)^2 + y_0^2} \qquad \text{(F-1)}$$

where:

$$x_0 = \frac{-2m_a m_b h - m_a(d_2+d_3) + m_b(d_1+d_2)}{2(m_b - m_a)} \qquad \text{(F-2)}$$

and

$$y_0 = -\frac{1}{m_a}\left(x_0 - \frac{d_1+d_2}{2}\right) - \frac{h}{2} \qquad \text{(F-3)}$$

where
$$m_a = \frac{h}{d_2 - d_1} \text{ and } m_b = \frac{h}{d_3 - d_2} \tag{F-4}$$

and h is the sensor distance fixed at 12 mm.

F-3.1 Basic Calculated Information

To provide a basis for comparing the performance of different fuel rod designs, it is necessary to calculate additional parameters such as the stress and strain, and they are typically discussed in terms of their maximum amplitude for CIRFT. It is also useful to look at the flexural rigidity, which tends to decrease as the test progresses. Typically, the flexural rigidity at the beginning of the test is discussed as a comparison point among rod types. The strain and stress parameters are calculated based on standard formulae for a circular beam in bending.

The maximum gauge strain, which occurs at the maximum deflections in the cycle and at the outermost radius of the rod, is calculated as the curvature multiplied by the LVDT maximum deflection:

$$\varepsilon = \kappa \times y_{max.} \tag{F-5}$$

The average moment applied to the rod is:

$$M = F \times L \tag{F-6}$$

where F is the averaged value of the load applied at the timespan of interest by the CIRFT motors and L is the fixed U-frame loading arm length (101.60 mm).

The maximum rod stress is calculated as:

$$\sigma = M \times y_{max} / I \tag{F-7}$$

where I is the area moment of inertia of the composite SNF rod calculated based on the geometry of cladding and solid pellet section.

The flexural rigidity, *EI*, provides a means to generate the stress-strain relationship associated with M-κ. The average calculated bending moment (ΔM) and average measured curvature ($\Delta \kappa$) are used to characterize the average flexural rigidity over the timespan of interest:

$$EI = \Delta M / \Delta \kappa. \tag{F-8}$$

F-3.2 Extended Calculated Information within the Context of CIRFT

In addition to the basic information discussed in Section F-3.1, other parameters of interest are developed to better understand the effect of particular rod characteristics on the fatigue.

SNF fuel rods are heterogeneous. Although the geometry of the irradiated rod can be estimated, it varies based on the type, manufacture, and operation of the rod. The irradiated rod contains cracked pellets (some with HBU rims), an inner cladding oxide layer, potentially a layer of pellet bonded with the cladding ID, cladding with radiation induced flaws, and an outer cladding oxide layer that is potentially discontinuous due to spalling. Axially, the fuel column is not continuous; it is composed of numerous short pellets. Although there could be some bonding between pellet ends as a result of an in-reactor galling process, the contacting surfaces areas are small due to the pellet chamfers and dishes, and the pellet-pellet bonding is not expected to be strong. Given these conditions, an SNF rod is far from an ideal homogeneous material, and the idealized treatment described in previous sections is not completely accurate.

To improve understanding of the rod's performance, some of these heterogeneous effects on fatigue lifetime were explored by mining the CIRFT data, including: (1) pellet-pellet and pellet-cladding bonding rod stiffening, (2) discontinuities in cladding support conditions at pellet-pellet interfaces, (3) cladding hydride reorientation, and (4) effects of the heat treatment applied to three of the SNF rods tested, as described in the following subsections.

F-3.2.1 Pellet Bonding Stiffening

Although the CIRFT data does not allow for separate effects testing, the measured flexural rigidity data can be trended to look for sudden shifts that could indicate pellet-pellet and pellet-cladding debonding. Previous testing [F-4, F-5] indicated that pellet-pellet bonding is relatively weak and likely becomes debonded after only a few CIRFT cycles. However, the pellet-cladding bond is expected to be stronger than the pellet-pellet bond. In cases where the rod was operated in-reactor at high temperature and power, a chemical bond may be developed between the pellet OD and the cladding inner diameter (ID). Wang and Wang proposed a dual flexural rigidity (i.e., before and after the bond is disrupted) with a bonding efficiency that can be applied in rod mechanical performance modeling.

F-3.2.2 Discontinuous Cladding Support

Although the LVDTs used on the CIRFT device only measure the gross rod deflection within the gauge section, several pellet lengths with several pellet-to-pellet interfaces are included in the gauge section, and any effects related to the pellet-pellet interfaces are embedded in the CIRFT data. An important observation from previous tests is the typical fracture location is at pellet-pellet interfaces, which is consistent with the reduced mechanical cross-section and potential interaction between the pellet end and cladding at those locations during bending. This was previously discussed by Wang and Wang as a fuel pellet "pinning" effect that is illustrated in Figure F- 6.

Although it is unlikely that the localized effect can be observed in the CIRFT data, Wang and Wang investigated the effects on the cladding using finite element analysis (FEA) and found that the localized strain in the cladding at the pellet-pellet-cladding interface region is three to four times higher than that in regions supported by the body of the fuel pellet due to interaction of the pellet end with the cladding and the localized axial tension applied as the gap is opened.

Wang and Wang further explored the shift in the neutral axis that occurs as pinning occurs. The neutral axis shifts constantly with each cycle, but the maximum strain still occurs at the outer radius of the cladding.
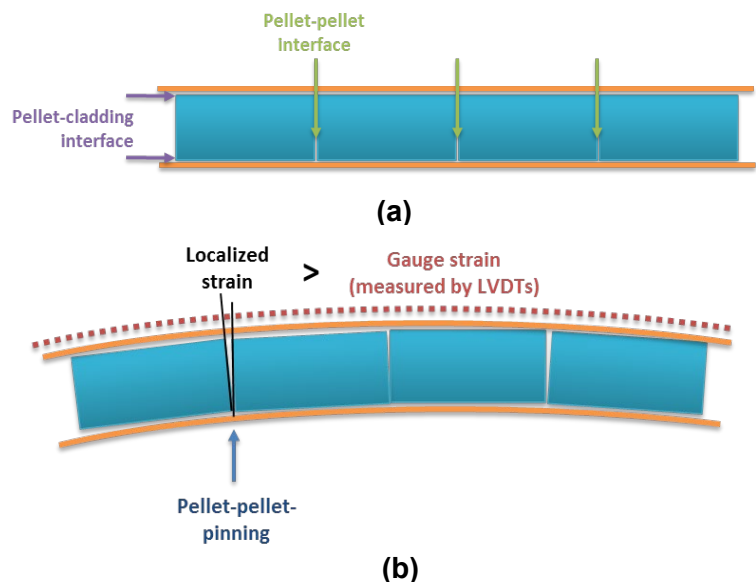
Figure F- 6. Cladding and pellet stack (a) in the neutral position and (b) in bending. [F-4]

F-3.2.3 Cladding Hydride Reorientation Effects

Hydrogen taken up by the fuel rod cladding in-reactor can be detrimental to performance when the hydrogen concentration exceeds the alloy's solubility and zirconium hydride platelets are precipitated within the cladding. Wang and Wang completed four CIRFT tests with cladding hydrides purposely

reoriented from circumferential to radial, but a large difference in performance was not observed in fatigue lifetime and no definitive statements could be made.

The sister rod tests provide additional insight with comparisons between heat-treated rods and baseline rods. However, not all sister rod heat treatments resulted in reoriented hydrides, since they were treated at more realistic temperature and cladding stress conditions. A description of the heat treatments and the degree of reorientation are provided in Appendices A and B.

F-3.2.4 Cladding Irradiation Defect Annealing

During reactor operation, the cladding is hardened and embrittled through the accumulation of irradiation defects. The baseline sister rods were tested in the as-received condition, and three rods were heat-treated, subjecting them to the potential for irradiation defect annealing.

F-3.2.5 Normal Condition Impacts

Impacts to the fuel rod are expected to reduce the fatigue lifetime because: (1) they are expected to disrupt pellet-pellet bonds and pellet-cladding bonds at the impact site leading to a reduced flexural rigidity, (2) the flexural rigidity of the rod determines the total deflection of the rod in bending, and (3) a low flexural rigidity results in larger deflections and a corresponding higher stress and strain. Thus, it is postulated that normal condition impacts could reduce the fatigue lifetime of the SNF rods.

Previous testing by Wang and Wang included non-normal impacts from a drop height of 12 in. with indeterminant results that were on the low side of the existing dataset. Future testing is expected to explore this effect with a more controlled impact method.

F-4. Comparison Data Available from Previous ORNL Tests

The NRC funded the development of the CIRFT and performed testing on HBU SNF with Zircaloy-4 (Zirc-4) and M5 cladding from pressurized water reactors (PWRs) and Zircaloy-2 (Zirc-2) from boiling water reactors (BWRs). Fifty-three cyclic fatigue tests in a range of load amplitudes were performed on PWR rod segments and 17 tests on BWR rod segments.

The burnup of the tested rod segments ranged between 45 and 67 GWd/MTU. The oxide layer thickness on the waterside surface of each segment was not specifically measured but was estimated to be between 20 to 110 μm with a corresponding estimated hydrogen concentration of 110–800 wppm. Wang and Wang completed four CIRFT tests in which the cladding hydrides were reoriented by pressurizing the segment and applying a thermal transient with the goal of understanding whether the radial hydrides reduced the fatigue lifetime.

The basic data from these tests are directly comparable with the sister rod test results and are summarized in Table F- 1 [F-4, F-5].

Table F- 1. Reference dataset [F-4, F-5].

Rod type	Cladding material	Parent rod-average burnup (GWd/MTU)	Test ID	Cycles to failure	Average moment (N-m)	Maximum average stress (MPa)	Maximum average strain (%)	Flexural rigidity (N-m^2)
15x15	Zirc-4	67	Demo1	4.0E+03	28.5	456	0.51	30.2
15x15	Zirc-4	67	Dcal	9.6E+03	28.6	366	0.41	37.9
15x15	Zirc-4	67	DL2H	1.8E+03	34.1	362	0.40	45.6
15x15	Zirc-4	67	S1	4.6E+03	28.5	327	0.36	42.3
15x15	Zirc-4	67	S2	7.2E+03	28.3	318	0.35	43.3
15x15	Zirc-4	67	DH3	7.1E+03	33.7	282	0.31	57.9
15x15	Zirc-4	67	R1	5.5E+03	29.0	227	0.25	61.9
15x15	Zirc-4	67	S3	2.5E+04	24.1	214	0.24	54.8
15x15	Zirc-4	67	DH2	6.5E+04	18.9	170	0.19	53.9
15x15	Zirc-4	67	DL1	1.1E+05	14.1	104	0.12	65.6
15x15	Zirc-4	67	DH1	2.5E+05	11.6	99	0.11	56.7
15x15	Zirc-4	67	S5	1.8E+05	11.6	84	0.09	66.4
15x15	Zirc-4	67	R3	1.3E+05	12.6	73	0.08	82.6
15x15	Zirc-4	67	R2	3.9E+05	10.0	70	0.08	69.3
15x15	Zirc-4	67	DL3	1.0E+06	9.2	60	0.07	73.4
15x15	Zirc-4	67	DM2	2.3E+06	8.2	56	0.06	71.9
15x15	Zirc-4	67	R4	2.7E+05	7.8	54	0.06	70.0
15x15	Zirc-4	67	HR1a[1]	4.2E+04	15.2	207	0.28	29.3
15x15	Zirc-4	67	HR2a[1]	9.5E+03	14.7	191	0.26	30.8
15x15	Zirc-4	67	HR4b[1]	5.5E+04	14.8	158	0.21	37.5
15x15	Zirc-4	67	HR3a[1]	2.4E+05	9.0	107	0.14	33.6
15x15	Zirc-4	67	DM3	1.3E+07[2]	7.7	51	0.06	73.8
15x15	Zirc-4	67	DM1	1.1E+07[2]	6.7	44	0.05	75.6
15x15	Zirc-4	67	R5	2.2E+07[2]	6.6	42	0.05	76.3
15x15	Zirc-4	67	DL2	6.4E+06[2]	4.2	22	0.03	91.5
17x17	M5	45	TH5	2.8E+04	11.2	312	0.32	16.6
17x17	M5	45	TH6	1.3E+04	13.4	308	0.32	20.1
17x17	M5	45	MOX17	1.2E+04	11.1	266	0.28	19.3
17x17	M5	45	TH3	1.5E+04	10.6	264	0.27	18.5
17x17	M5	45	TH2	5.7E+04	11.0	255	0.14	20.1
17x17	M5	45	MOX14	8.7E+04	6.2	254	0.26	11.3
17x17	M5	45	MOX7	1.6E+04	13.9	239	0.25	26.9
17x17	M5	52	NA7	1.3E+04	13.5	232	0.30	27.1
17x17	M5	45	MOX8	1.3E+04	11.0	206	0.21	24.9

Rod type	Cladding material	Parent rod-average burnup (GWd/MTU)	Test ID	Cycles to failure	Average moment (N-m)	Maximum average stress (MPa)	Maximum average strain (%)	Flexural rigidity (N-m²)
17x17	M5	45	TH1	5.7E+04	8.8	204	0.21	19.9
17x17	M5	52	NA1	1.6E+04	11.0	194	0.25	26.2
17x17	M5	45	MOX13	2.7E+04	8.7	171	0.18	23.6
17x17	M5	45	MOX15	2.0E+04	8.5	167	0.07	23.5
17x17	M5	45	MOX2	3.7E+04	8.5	161	0.17	24.3
17x17	M5	45	MOX12	4.2E+04	8.7	158	0.16	25.6
17x17	M5	45	TH4	2.5E+06	6.3	151	0.16	19.2
17x17	M5	52	NA2	2.2E+04	8.8	149	0.19	27.4
17x17	M5	45	MOX10	3.9E+04	8.7	144	0.15	28.2
17x17	M5	45	MOX11	4.2E+04	8.7	142	0.15	28.1
17x17	M5	45	MOX9	9.0E+04	6.3	121	0.13	24.0
17x17	M5	52	NA4	6.1E+04	6.3	84	0.11	35.0
17x17	M5	45	MOX16	3.7E+03	13.2	78	0.39	16.3
17x17	M5	45	MOX5	4.5E+05	4.8	68	0.07	32.6
17x17	M5	45	MOX6	5.4E+05	3.8	64	0.07	27.6
17x17	M5	45	MOX4	2.2E+06	3.9	50	0.05	36.1
17x17	M5	52	NA6	4.3E+05	4.0	46	0.06	40.3
17x17	M5	45	TH2	3.8E+06[2]	6.2	134	0.14	21.6
17x17	M5	52	NA5	5.1E+06[2]	4.0	54	0.07	34.0
9x9	Zirc-2	57	LM1	9.4E+03	23.4	386	0.42	31.7
9x9	Zirc-2	57	LM17	1.3E+04	28.1	365	0.10	40.1
9x9	Zirc-2	57	LM16	1.4E+04	28.6	280	0.31	53.3
9x9	Zirc-2	57	LM13	2.1E+04	21.4	228	0.25	49.0
9x9	Zirc-2	57	LM10	5.2E+04	18.9	210	0.23	47.0
9x9	Zirc-2	57	LM7	1.2E+05	13.9	149	0.16	48.9
9x9	Zirc-2	57	LM2	1.7E+05	11.5	114	0.12	52.6
9x9	Zirc-2	57	LM3	4.9E+05	9.0	104	0.11	45.3
9x9	Zirc-2	57	LM15	4.4E+05	9.0	96	0.11	48.6
9x9	Zirc-2	57	LM9	7.3E+05	9.1	92	0.10	51.2
9x9	Zirc-2	57	LM14	3.9E+05	9.0	85	0.09	55.9
9x9	Zirc-2	57	LM5	2.5E+05	7.6	71	0.08	56.1
9x9	Zirc-2	57	LM11	3.6E+05	7.7	69	0.08	57.6
9x9	Zirc-2	57	LM6	1.8E+06	6.5	66	0.07	51.5
9x9	Zirc-2	57	LM8	4.7E+06	6.6	55	0.06	62.9
9x9	Zirc-2	57	LM12	7.6E+06[2]	6.1	88	0.10	36.3
9x9	Zirc-2	57	LM17	3.4E+06[2]	7.5	87	0.10	44.7

1   The specimens were pressurized and subjected to a thermal transient to induce cladding hydride reorientation prior to conducting the unpressurized CIRFT test.
2   The test was discontinued without specimen fracture.
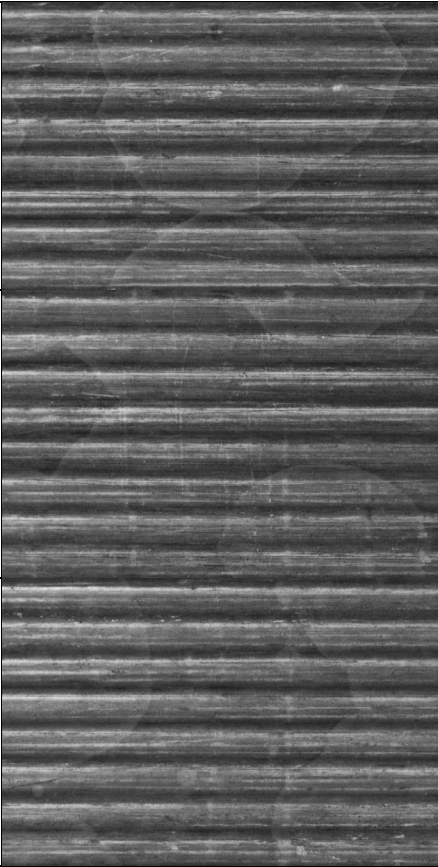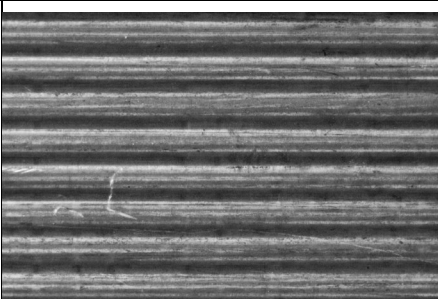
F-5. Description of the Sister Rods Tested
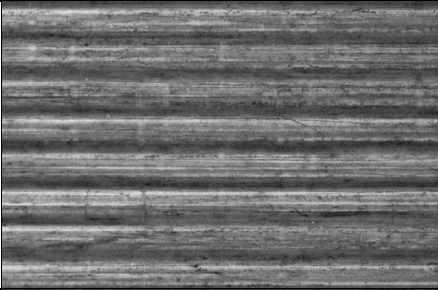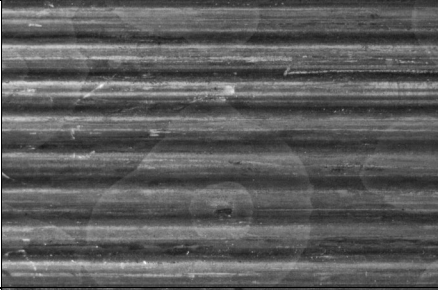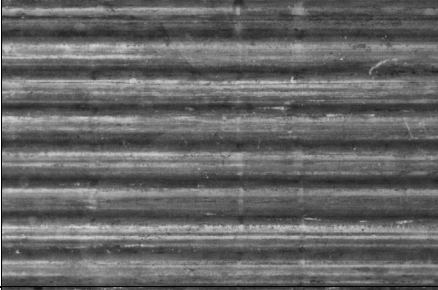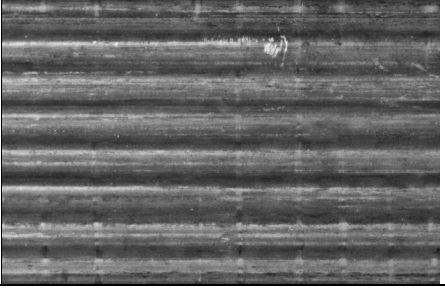
An additional description of the rods used in the tests is provided in the sister rod test plan [F-3] and the nondestructive test results [F-6]. All rods were operated by Dominion Energy at the North Anna Power Station to high rod average burnup (>45 GWd/MTU). Table F- 2 summarizes the sister rod's parent assembly operation and lattice location for the rods test using CIRFT.
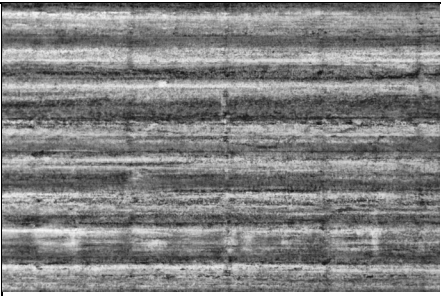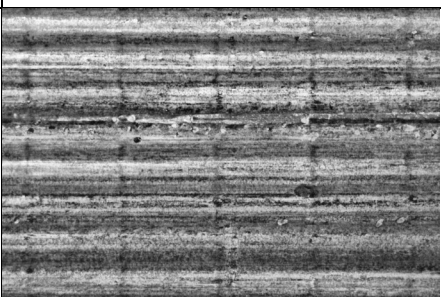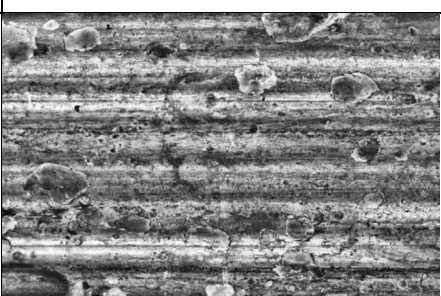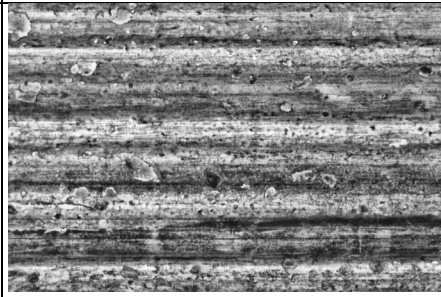
In Phase 1 of the sister rod test program [F-1, F-2], seven of ORNL's 15 sister rods were selected for paired testing: one baseline fuel rod and one heat-treated fuel rod of each cladding type (M5, ZIRLO, and Zirc-4/LT-Zirc-4), plus an extra ZIRLO-clad rod for additional datapoints since no ZIRLO-clad rods were tested in previous campaigns. Baseline rods are tested in the condition in which they were received at ORNL and full length heat-treatment (FHT) rods are subjected to a thermal transient before testing, as described in Appendix A, to simulate dry storage conditions. Three full-length fuel rods have been heat-treated to date— one Zirc-4-clad (F35P17), one ZIRLO-clad (3F9N05), and one M5-clad (30AE14)—and the results from the heat-treated rods were compared with the results from the baseline rods to determine whether the fatigue lifetime is affected by dry storage thermal transients.
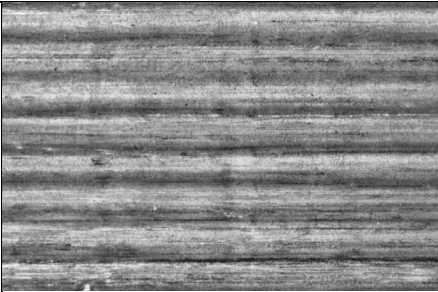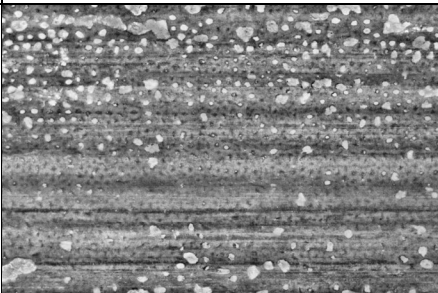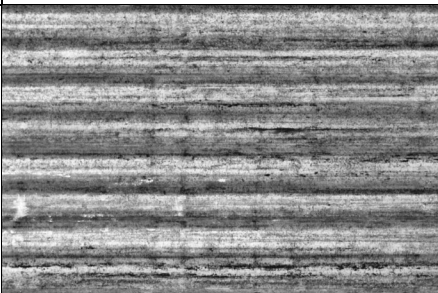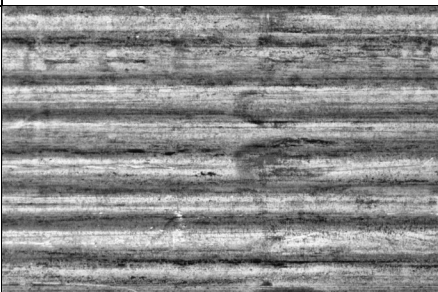
The CIRFT uses152.4 mm (6 in.) long specimens taken from various elevations of the SNF rods. Because the rod burnup varies as a function of elevation, the rod average burnup is used in conjunction with the gamma scans of the rod [F-6] to estimate the average burnup of the CIRFT segment, as listed in Table F- 2. Full-circumference flattened—as defined in nondestructive examination (NDE) report [F-6]—images of the pretest waterside surface condition of the CIRFT segments are also provided in Table F- 2.
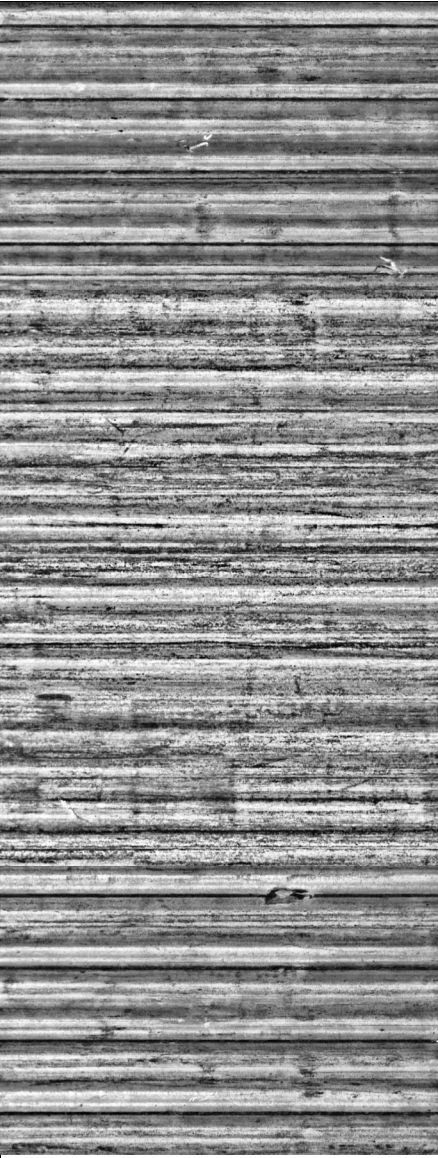
Table F- 2. Sister rod segments selected for CIRFT.
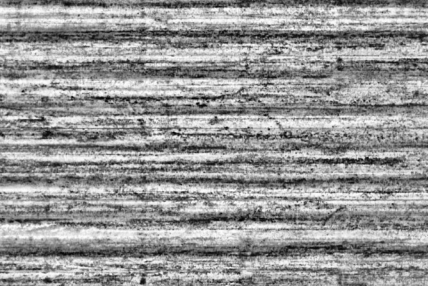
Clad material	Donor assembly	Sister rod lattice location	Assembly average burnup (GWd/MTU)	Rod average burnup (GWd/MTU)	Heat treatment applied to the rod	Measured rod internal pressure (MPa)	Measured rod void volume (cc)	Specimen lower elevation (mm)	Specimen upper elevation (mm)	Average specimen burnup (GWd/MTU)	Rod 360° appearance near the CIRFT gauge section pretest
M5											The M5-clad rods exhibited very light waterside oxide visible as irregular, somewhat circular patches, with some areas including an interior patch that appears to have peeling oxide. Grid-to-rod-fretting (GTRF) marks are visible in some grid elevations along with rod removal scratches.
	30A	D05	52.0	54	No	3.46	10.63	697	850	58	
	30A	D05	52.0	54	No	3.46	10.63	2,050	2,203	59	
	30A	D05	52.0	54	No	3.46	10.63	2,630	2,783	59	
	30A	D05	52.0	54	No	3.46	10.63	3,732	3,886	24	Pellet-pellet gaps throughout
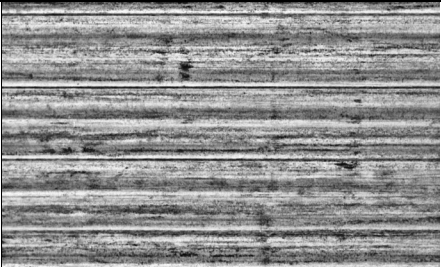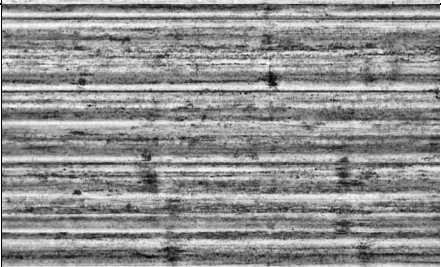
Clad material	Donor assembly	Sister rod lattice location	Assembly average burnup (GWd/MTU)	Rod average burnup (GWd/MTU)	Heat treatment applied to the rod	Measured rod internal pressure (MPa)	Measured rod void volume (cc)	Specimen lower elevation (mm)	Specimen upper elevation (mm)	Average specimen burnup (GWd/MTU)	Rod 360° appearance near the CIRFT gauge section pretest
M5	30A	D05	52	54	No	3.46	10.63	3,452	3,605	38	
	30A	E14	52	54	Yes	3.22	10.99	672	825	56	
	30A	E14	52	54	Yes	3.22	10.99	2,850	3,003	60	
	30A	E14	52	54	Yes	3.22	10.99	3,156	3,309	56	
	30A	E14	52	54	Yes	3.22	10.99	3,003	3,156	58	

Clad material	Donor assembly	Sister rod lattice location	Assembly average burnup (GWd/MTU)	Rod average burnup (GWd/MTU)	Heat treatment applied to the rod	Measured rod internal pressure (MPa)	Measured rod void volume (cc)	Specimen lower elevation (mm)	Specimen upper elevation (mm)	Average specimen burnup (GWd/MTU)	Rod 360° appearance near the CIRFT gauge section pretest
											Assemblies 3A1 and F35 (Zirc-4 / LT Zirc-4 cladding types) appeared to have the greatest amount of oxide buildup/spalling among the sister rods. No visible signs of through-wall damage or large areas of clad degradation were found, but some areas of significant oxidation have a flake-like appearance and spalling is evident at some elevations. Some shallow GTRF marks are visible, and some features that appear to be GTRF marks oxidized in later cycles are visible.
LT Zirc-4	3A1	F05	50	51	No	3.73	12.94	1,853	2,006	56	
	3A1	F05	50	51	No	3.73	12.94	2,025	2,178	56	
	3A1	F05	50	51	No	3.73	12.94	3,214	3,367	48	 Under grid location, no fretting marks visible.
	3A1	F05	50	51	No	3.73	12.94	3,367	3,520	44	

Clad material	Donor assembly	Sister rod lattice location	Assembly average burnup (GWd/MTU)	Rod average burnup (GWd/MTU)	Heat treatment applied to the rod	Measured rod internal pressure (MPa)	Measured rod void volume (cc)	Specimen lower elevation (mm)	Specimen upper elevation (mm)	Average specimen burnup (GWd/MTU)	Rod 360° appearance near the CIRFT gauge section pretest
	Assemblies 3A1 and F35 (Zirc-4 / LT Zirc-4 cladding types) appeared to have the greatest amount of oxide buildup/spalling among the sister rods. No visible signs of through-wall damage or large areas of clad degradation were found, but some areas of significant oxidation have a flake-like appearance and spalling is evident at some elevations. Some shallow GTRF marks are visible, and some features that appear to be GTRF marks that have oxidized in later cycles are visible.										
Zirc-4	F35	P17	58	60	Yes	4.68	13.32	2,027	2,180	52	
	F35	P17	58	60	Yes	4.68	13.32	1,855	2,008	53	
	F35	P17	58	60	Yes	4.68	13.32	3,159	3,312	47	
	F35	P17	58	60	Yes	4.68	13.32	3,312	3,465	43	

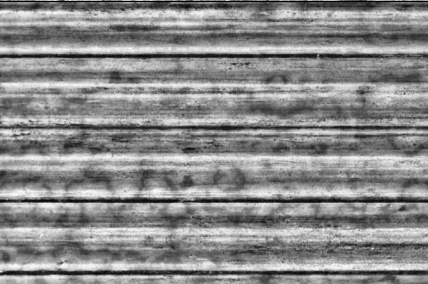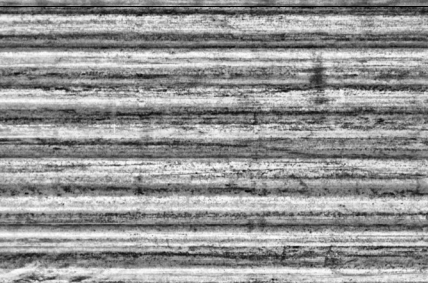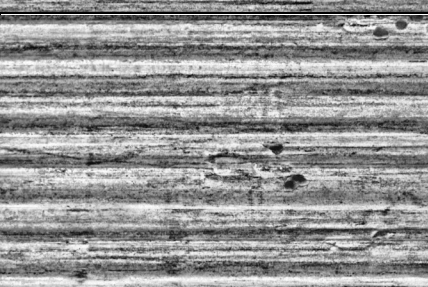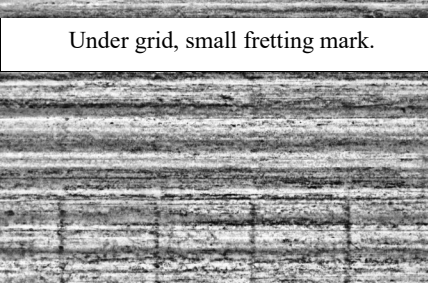| Clad material	Donor assembly	Sister rod lattice location	Assembly average burnup (GWd/MTU)	Rod average burnup (GWd/MTU)	Heat treatment applied to the rod	Measured rod internal pressure (MPa)	Measured rod void volume (cc)	Specimen lower elevation (mm)	Specimen upper elevation (mm)	Average specimen burnup (GWd/MTU)	Rod 360° appearance near the CIRFT gauge section pretest
ZIRLO											The ZIRLO-clad rods have a moderate-to-heavy oxide layer, with some oxide peeling observed. GTRF marks are present on most rods and range in severity from shallow to deep. No visible signs of through-wall cladding damage were observed. Darker regions are present at grid elevations, indicating either CRUD or possibly a thinner oxidation layer (attributed to better heat transfer in those areas due to flow turbulence).
	3D8	E14	55	59	No	4.18	11.73	719	872	64	
	3D8	E14	55	59	No	4.18	11.73	2,412	2,565	64	
	3D8	E14	55	59	No	4.18	11.73	2,963	3,116	62	
	3D8	E14	55	59	No	4.18	11.73	1,178	1,331	63	Under grid location, GTRF mark aligned at maximum strain location

Clad material	Donor assembly	Sister rod lattice location	Assembly average burnup (GWd/MTU)	Rod average burnup (GWd/MTU)	Heat treatment applied to the rod	Measured rod internal pressure (MPa)	Measured rod void volume (cc)	Specimen lower elevation (mm)	Specimen upper elevation (mm)	Average specimen burnup (GWd/MTU)	Rod 360° appearance near the CIRFT gauge section pretest
ZIRLO	3D8	E14	55	59	No	4.18	11.73	3,225	3,378	56	
	3F9	N05	52	54	Yes	3.98	12.74	719	872	59	
	3F9	N05	52	54	Yes	3.98	12.74	2,329	2,482	59	
	3F9	N05	52	54	Yes	3.98	12.74	2,710	2,863	57	Under grid, small fretting mark.
	3F9	N05	52	54	Yes	3.98	12.74	3,440	3,593	45	

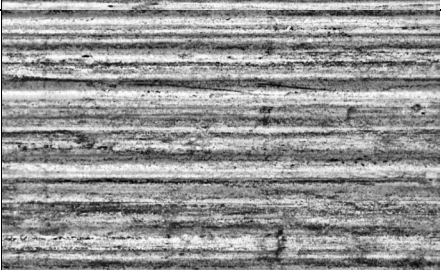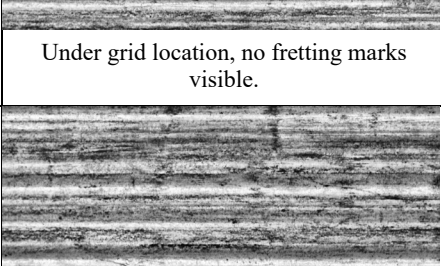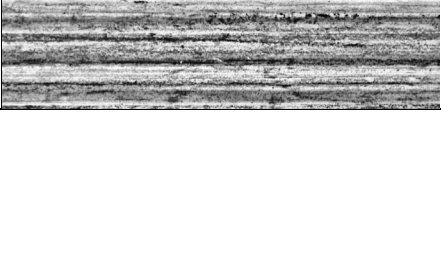| Clad material	Donor assembly	Sister rod lattice location	Assembly average burnup (GWd/MTU)	Rod average burnup (GWd/MTU)	Heat treatment applied to the rod	Measured rod internal pressure (MPa)	Measured rod void volume (cc)	Specimen lower elevation (mm)	Specimen upper elevation (mm)	Average specimen burnup (GWd/MTU)	Rod 360° appearance near the CIRFT gauge section pretest
ZIRLO	6U3	K09	53	55	no	3.64	11.78	2,310	2,463	59	
	6U3	K09	53	55	no	3.64	11.78	2,463	2,616	59	
	6U3	K09	53	55	no	3.64	11.78	2,635	2,788	58	
	6U3	K09	53	55	no	3.64	11.78	3,200	3,353	50	 Under grid location, no fretting marks visible.
	6U3	K09	53	55	no	3.64	11.78	3,353	3,506	46	

F-6. Selection of CIRFT Test Conditions

In specifying the loading conditions for the CIRFT tests, the previous data for M5 and Zirc-4 clad fuel rods were surveyed [F-4,F-5] and several objectives were identified for the sister rod tests:

- Demonstrate that M5 and Zirc-4 clad sister rod fatigue performance is consistent with the data given in the established database for those cladding alloys

- Demonstrate whether FHT changes the fatigue lifetime of the cladding/rod when compared with non-FHT segments

- Demonstrate whether GTRF marks result in a reduced fatigue lifetime when they are aligned with the point of peak cladding deflection during the test

- Establish a range of tests for rods that have ZIRLO cladding consistent with the data given in the established database for other cladding alloys and demonstrate whether the ZIRLO-clad rods are consistent with other rods

The sister rods are tested statically and dynamically as paired samples that have similar burnup and oxide thicknesses.

a. **Baseline rod specimens:** one specimen tested statically followed by a dynamic test at a relatively high load (~175 N-m); one specimen tested dynamically at a moderate load (~10–12 N-m); and one specimen tested dynamically at a low load (~5–6 N-m);

b. **Heat-treated rod specimens:** one specimen tested statically followed by a dynamic test at the same load used for the baseline specimen; one specimen tested dynamically at the same moderate load used for the baseline specimen; and one specimen tested dynamically at the same low load used for the baseline specimen.

Table F- 3 lists the selected test type, test load, and paired specimens.

Table F- 3. CIRFT specimen and test pairing

Baseline specimens				Heat-treated specimens				Test Type	Nominal test moment applied (N-m)	Notes
Specimen ID			Cladding type	Specimen ID			Cladding type	Estimated specimen average burnup (GWd/MTU)		
30AD05	0697	0850	M5	58	30AE14	0672	0825	M5	56	Static followed by Dynamic	17.8	---
30AD05	2050	2203		59	30AE14	3156	3309		56	Dynamic	6.1	---
30AD05	2630	2783		59	30AE14	2850	3003		60	Dynamic	12.2	---
30AD05	3732	3886		24						Dynamic	--	pellet-pellet gaps – not yet tested
30AD05	3452	3605	M5	38	30AE14	3003	3156	M5	58	Cumulative	--	Future test
3A1F05	1853	2006	LT Zirc-4	56	F35P17	1855	2008	Zirc-4	53	Static followed by Dynamic	17.8	---
3A1F05	3367	3520		44	F35P17	2027	2180		52	Dynamic	5.1	Replacement; originally allocated as a cumulative test specimen
3A1F05	2025	2178		56						Dynamic	10.2	Originally allocated for 5.1 N-m, but mistakenly tested at 10.2 N-m
3A1F05	3214	3367		48	F35P17	3159	3312		47	Dynamic	10.2	
					F35P17	3312	3465	Zirc-4	43	Cumulative	--	Future test
3D8E14	0719	0872	ZIRLO	64	3F9N05	719	872	ZIRLO	59	Static followed by Dynamic	17.8	---
3D8E14	2412	2565		64	3F9N05	2329	2482		59	Dynamic	6.1	---
3D8E14	2963	3116		62	3F9N05	2710	2863		57	Dynamic	10.2	---
3D8E14	1178	1331		63						Dynamic	6.1	---
6U3K09	2310	2463		59						Dynamic	14.3	Additional higher load data point
6U3K09	2463	2616		59						Dynamic	10.2	Provides a good comparison with 3F9N05-2710-2863 based on segment burnup
6U3K09	2635	2788		58						Dynamic	7.6	Provides a good comparison with 3F9N05-2329-2482 based on segment burnup
6U3K09	3200	3353		50						Dynamic	10.2	Provides a comparison with 3F9N05-2710-2863 based on segment burnup
6U3K09	3353	3506		46						Dynamic	13.3	Additional higher load data point
3D8E14	3225	3378	ZIRLO	56	3F9N05	3440	3593	ZIRLO	45	Cumulative	--	Future test

F-7. Test Results

F-7.1 Static Tests

The static test is performed to measure the range of flexure of representative specimens for each sister rod category: M5-clad, ZIRLO-clad, and Zirc-4 or LT Zirc-4-clad. Six specimens—one of each cladding type and heat treatment—were tested in static mode to measure the flexural rigidity before testing in dynamic mode. An example of the data typically acquired is shown in Figure F- 7. None of the rod segments were flexed to failure, although all were flexed beyond the knee in the curve (Figure F- 7 point B). Each static test specimen was tested in dynamic mode following the static test and additional data is available on the flexural rigidity in the dynamic test results.
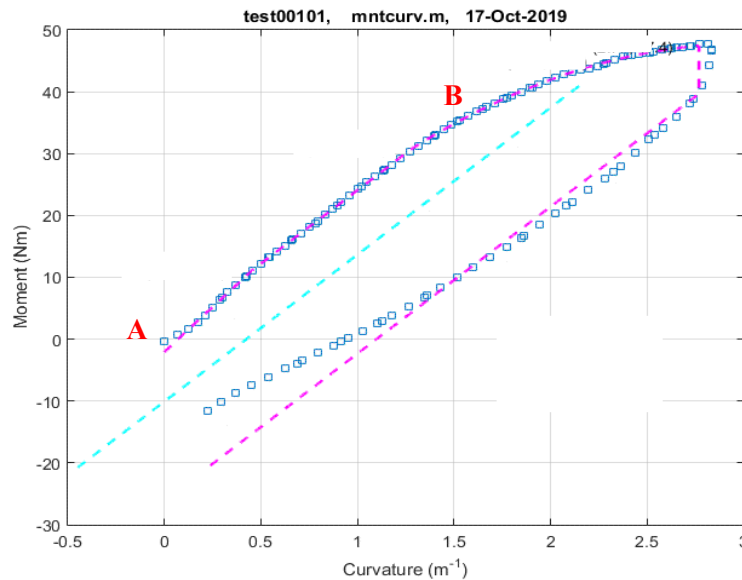
Figure F- 7. Typical static test data and transition points.

Of the six static tests performed, three static tests included suspect data. For 30AE14-0672-0825 and 3D8E14-0719-0872, the LVDTs were not responding as expected (appeared to be stuck at times) and did not provide consistent curvature (and therefore, rigidity) information. For F35P17-0719-0872, the load cell data is erratic and the measured moment is unreliable.

The results the three static tests with valid results are provided in Table F- 4. Results from the dynamic tests (Section F-7.2) are provided for comparison and are representative of the A-B region of the curve measured during the dynamic test. Generally, the dynamically measured A-B rigidity of the statically measured segments should be lower than the static measurements since the rod was flexed past the knee. The data for 30AD05-0697-0850 (M5-clad, baseline) are very consistent with the dynamic data and with other M5-clad baseline segments tested. The results for 3A1F05-1853-2006 are as expected, with the dynamic rigidity lower than the static rigidity (flexed past the knee). 3F9N05-0719-0872 is similar and consistent with expectations.

Table F- 4. Static Test Results.

Rod type	Cladding material	Heat-treated?	Estimated specimen-average burnup (GWd/MTU)	Specimen ID	Applied moment, A to B (N-m)	A to B region flexural rigidity (N-m^2)	Dynamically applied moment (N-m)[1]	Dynamically measured flexural rigidity (after static flexure) (N-m^2)[1]
17x17	M5	No	58	30AD05-0697-0850	11.11	29.10	17.78[2]	28.35[2]
17x17	M5	Yes	56	30AE14-0672-0825	Not reported due to data acquisition issue		15.55	20.48
17x17	LT Zirc-4	No	56	3A1F05-1853-2006	15.97	34.60	15.92	19.34
17x17	Zirc-4	Yes	66	F35P17-1855-2008	Not reported due to data acquisition issue		17.78[2]	28.74[2]
17x17	ZIRLO	No	64	3D8E14-0719-0872	Not reported due to data acquisition issue		17.78[2]	30.89[2]
17x17	ZIRLO	Yes	59	3F9N05-0719-0872	17.24	27.22	15.53	18.01

1. Data are discussed in Section F-7.2.
2. Values are estimated.

F-7.2 Dynamic Tests

All Phase 1 CIRFT dynamic tests were completed. Six specimens were cycled in static mode before testing dynamically, which is referred to as *static/dynamic tests*. The results from the static/dynamic tests are not strictly comparable with the other tests since some changes in the rod condition likely occurred during the static test.

Figure F- 8 plots the applied bending moment with the number of cycles to failure measured for completed tests with the available previous data [F-4,F-5]. Figure F- 9 plots the strain amplitude vs. the number of cycles to failure for tests in which an extended analysis of the test data is available (10 of the 13 tests). The stress amplitude can be plotted as a function of the number of cycles to failure to map the fatigue lifetime of the rods, as shown in Figure F- 10. Except for the two outliers from heat-treated rod F35P17, the results are consistent with previous data for the same size of fuel rods (17×17), although when trended with stress the sister rod fatigue lifetime appears to be on the lower side of other lifetime estimates [F-9, F-10,F-11]. Some data are below the simulation-based fatigue curve [34] as shown in Figure F- 10. The cycles to failure data for the F35P17 specimens are dichotomous with two specimens failing at a very low number of cycles and a third specimen having the longest number of cycles to failure within the sister rod test group. The F35P17-3159-3312 test includes some erratic load cell data, but its cycles to failure are consistent with specimen F3517-1855-2008 where no anomalous data exists.

Flexural rigidity is also measured during the dynamic test at the specific test conditions. The results of the dynamic flexural rigidity measurements are provided in Table F- 5. For three of the static tests, the data required to calculate the flexural rigidity were unavailable and the flexural rigidity was estimated for these cases. The flexural rigidity measured for the sister rod specimens is plotted as a function of the estimated specimen burnup in Figure F- 11, along with the measured flexural rigidity of other rods tested at ORNL using CIRFT [F-7,F-8]. Although there appears to be a mild trend with burnup, when considered with previous data, it could also be relatively constant with burnup. Although the estimated burnup of the sister rod segments is accurate, it is unclear whether the burnup cited for the reference dataset is a rod-average or segment-average, and this is expected to be one source of the scatter inherent in the reference dataset. The flexural rigidity of the specimen changes over the CIRFT test; a rod subjected to many bending cycles is expected to have a lower flexural rigidity than an uncycled rod, especially at large applied moments. Also, there is a mild trend in which the dynamically-measured flexural rigidity declines with increased applied bending moment, as shown in Figure F- 12.

Although the static specimens are tested in dynamic mode after the static test, the dynamic results for the static/dynamic specimens are not strictly comparable with the dynamic-only test results (as discussed in Section F-3.2.1). The results of the dynamic tests of these specimens are provided for information.

Except for F35P17, the sister rod data are self-consistent and are consistent with previous data from other 17 × 17 rods. To further evaluate the performance of the heat-treated Zirc-4 clad rod, it is recommended that an additional two tests be completed. The difference in the performance of the Zirc-4 clad rod could be a result of the main geometric difference of the rods – the pellet length – and if so, further data analysis focused on pellet length could clarify the effect.

F-7.3 Cumulative Effects Tests

No tests have been completed to date. A fixture is under development and is discussed in Section F-8.

Table F- 5. Sister rod CIRFT test results to date.

Rod type	Cladding material	Estimated specimen-average burnup (GWd/MTU)	Specimen ID	Curvature (m)	Cycles to failure	Applied moment (N-m)	Stress (MPa)	Strain (%)	Dynamic flexural rigidity (N-m^2)
17x17	M5	58	30AD05-0697-0850[1]	0.63[2]	3,368	17.78[2]	187.05[2]	0.21[2]	28.35[2]
17x17	M5	59	30AD05-2050-2203	0.18	133,000	5.09	61.87	0.08	28.73
17x17	M5	59	30AD05-2630-2783	0.38	22,300	10.67	129.55	0.18	27.97
17x17	M5	56	30AE14-0672-0825[1,3]	0.76	1,630	15.55	187.05	0.36	20.48
17x17	M5	60	30AE14-2850-3003[3]	0.46	9,800	10.56	126.99	0.22	23.63
17x17	M5	56	30AE14-3156-3309[3]	0.21	113,000	4.95	59.50	0.10	23.23
17x17	Zirc-4	66	F35P17-1855-2008[1,3]	0.62[2]	525	17.78[2]	191.51[2]	0.16[2]	28.74[2]
17x17	Zirc-4	66	F35P17-2027-2180[3]	0.15	1,340,000	4.05	47.83	0.07	26.83
17x17	Zirc-4	62	F35P17-3159-3312[3,4]	0.32	773	8.55	100.96	0.15	30.66
17x17	LT Zirc-4	48	3A1F05-3214-3367	0.41	3,450	8.80	105.88	0.19	21.56
17x17	LT Zirc-4	56	3A1F05-1853-2006[1]	0.82	1,300	15.92	191.51	0.39	19.34
17x17	LT Zirc-4	56	3A1F05-2025-2178	0.38	48,200	8.80	105.88	0.18	23.18
17x17	LT Zirc-4	44	3A1F05-3367-3520	0.14	214,000	4.04	48.55	0.06	29.74
17x17	ZIRLO	64	3D8E14-0719-0872[1]	0.58[2]	9,589	17.78[2]	186.29[2]	0.11[2]	30.89[2]
17x17	ZIRLO	64	3D8E14-2412-2565[5]	0.18	191,000	5.05	60.13	0.08	31.31
17x17	ZIRLO	62	3D8E14-2963-3116	0.31	39,700	8.74	104.20	0.15	28.06
17x17	ZIRLO	63	3D8E14-1178-1331	0.16	212,000	4.90	58.43	0.08	30.94
17x17	ZIRLO	59	3F9N05-0719-0872[3]	0.86	3,540	15.53	186.29	0.41	18.01
17x17	ZIRLO	59	3F9N05-2329-2482[3]	0.21	189,000	4.78	57.29	0.10	22.55
17x17	ZIRLO	57	3F9N05-2710-2863[3]	0.40	33,000	8.73	104.68	0.19	21.85
17x17	ZIRLO	59	6U3K09-2310-2463	0.42	1.75E+04	12.70	152.31	0.20	30.22
17x17	ZIRLO	59	6U3K09-2463-2616	0.27	3.92E+04	8.88	106.48	0.13	32.39
17x17	ZIRLO	58	6U3K09-2635-2788	0.17	1.10E+05	6.41	76.82	0.08	37.10
17x17	ZIRLO	50	6U3K09-3200-3353	0.31	3.49E+04	8.78	105.30	0.15	30.04
17x17	ZIRLO	46	6U3K09-3353-3506	0.43	1.41E+04	11.69	140.18	0.21	27.03

1. Dynamically tested following a static test.
2. Estimated.
3. Specimen from heat-treated rod.
4. Erratic load cell data were recorded during the test. The applied moment might have been higher.
5. Specimen had a GTRF mark in the gauge section that was aligned (as was possible) with the expected maximum strain location.
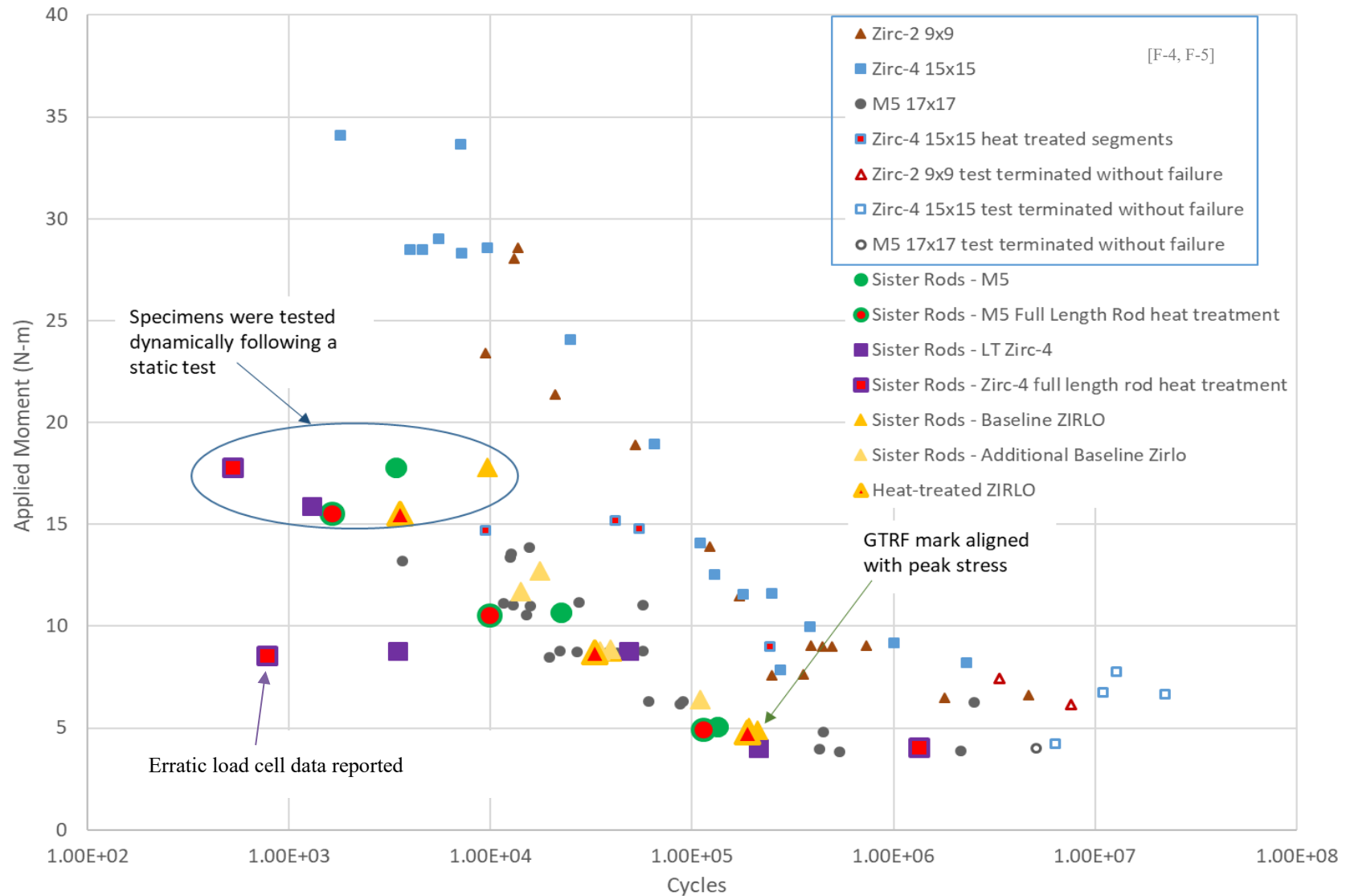
Figure F- 8. Results of sister rod CIRFT tests plotted with reference data, applied moment vs. cycles to failure.
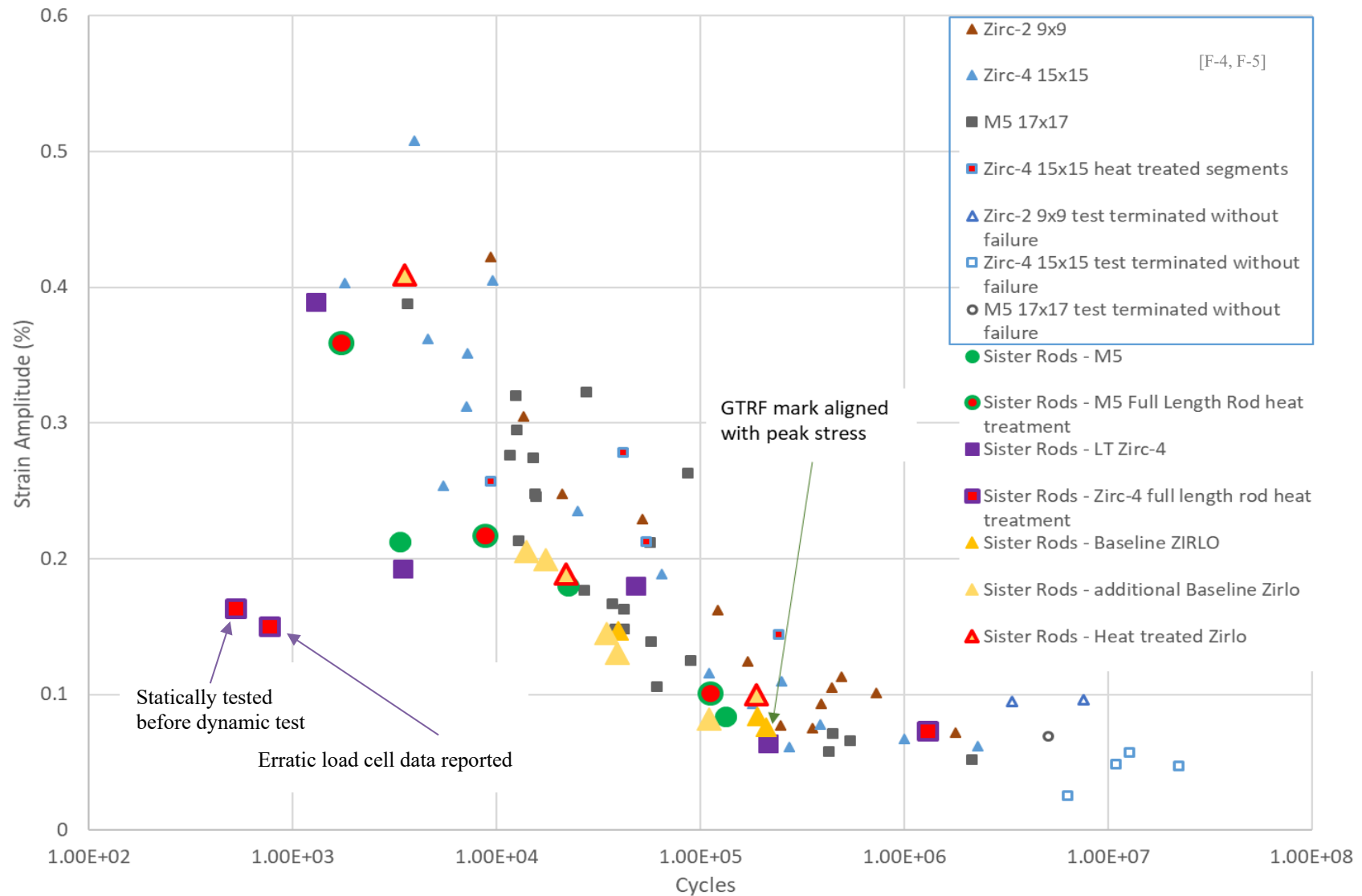
Figure F- 9. Results of CIRFT tests completed to date, strain amplitude vs. cycles to failure.
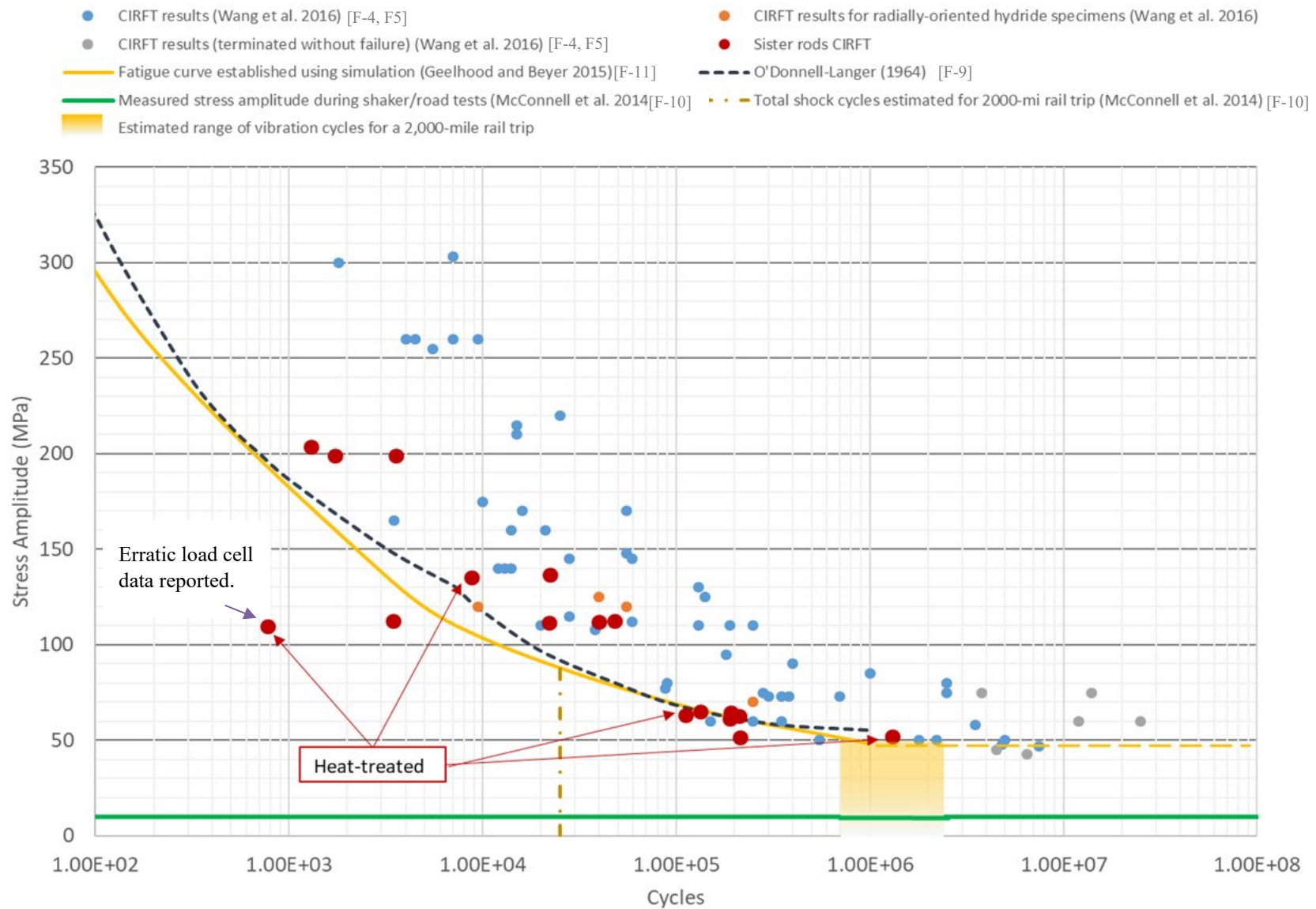
Figure F- 10. Stress amplitude as a function of cycles to failure for the sister rods.
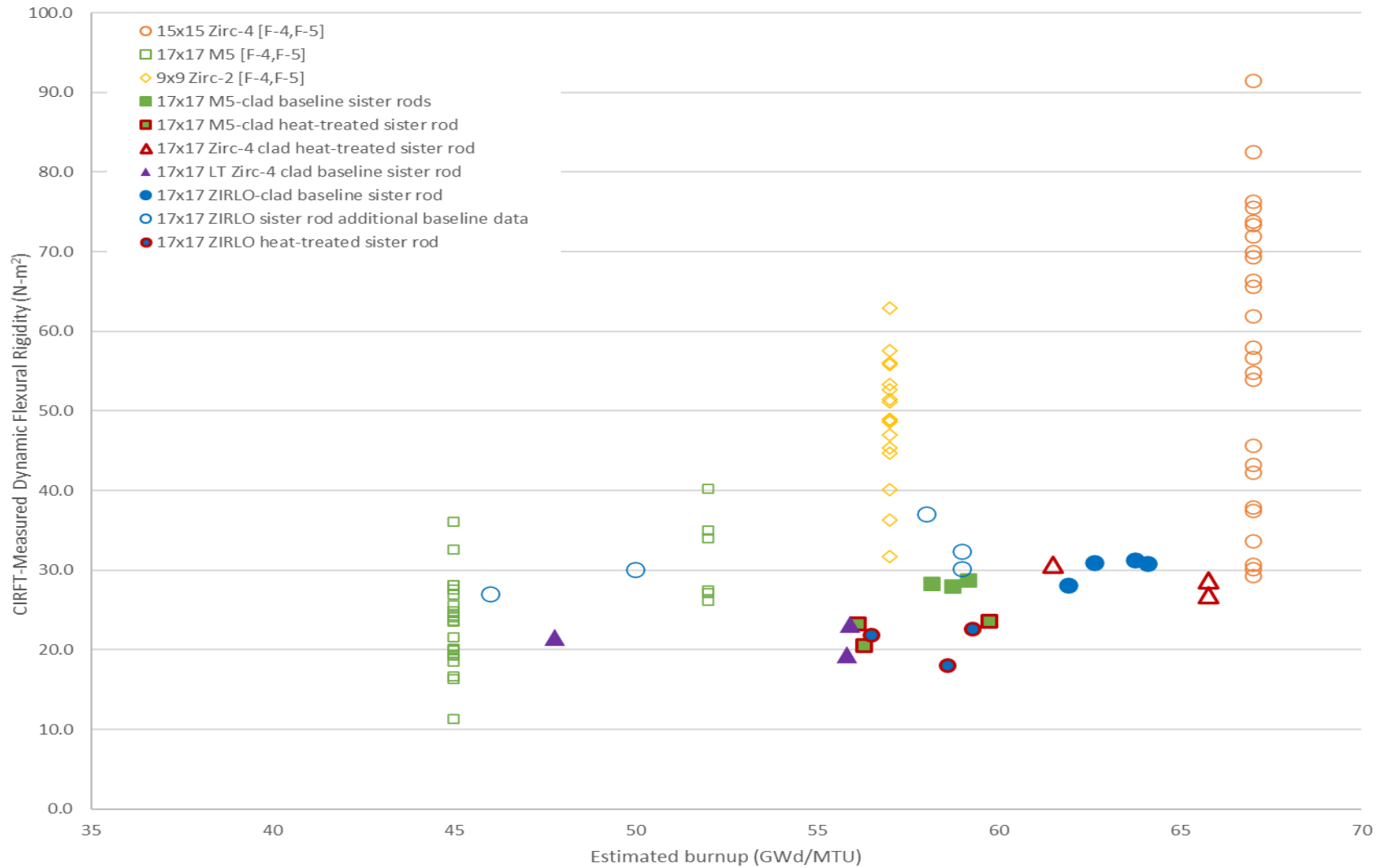
Figure F- 11. CIRFT-measured flexural rigidity of the sister rod segments tested as a function of estimated segment burnup plotted with previous CIRFT data.

Figure F- 12. Trend of CIRFT-measured dynamic flexural rigidity with applied bending moment.

F-7.4 Comparisons of Paired Specimens

The paired results are tabulated in Table F- 6. Averages are provided for burnup, cycles to failure, strain, and flexural rigidity for comparison purposes. For the M5-clad and ZIRLO-clad segments, the heat-treated rods generally have a shorter fatigue lifetime and lower flexural rigidity. Revisiting Figure F- 11, the small but consistent difference in flexural rigidity between the baseline and heat-treated rods is clear. The reverse seems to be true for the Zirc-4-clad and LT Zirc-4-clad pairs; the heat-treated Zirc-4-clad segments have a higher flexural rigidity and a longer fatigue lifetime than the baseline LT Zirc-4-clad segments. However, there are several differences in the parent rods, and these two rods are not good matches for comparing heat-treatment effects. The most likely explanation for the difference in performance is the pellet length. Referring to Table 4 of the NDE report [F-6], the pellets in the Zirc-4-clad rod were ~13.6 mm long, whereas the pellets in all other sister rods were ~10 mm long. It is very likely that the increased stiffness is related to the longer pellet length.

Figure F- 8 further illustrates a reduced fatigue lifetime related to the heat treatments. This effect is seen for all M5-clad and ZIRLO-clad heat-treated specimens. However, when the cycles to failure are plotted with the calculated strain amplitude, the offset related to the heat-treatment is eliminated, as shown in Figure F- 9. Since the rods have nearly the same geometry, the calculated strain would normally be expected to provide the same offset between baseline and heat-treated specimen results. However, for CIRFT, the strain is calculated based on the measured rod deflection and flexural rigidity. Because the heat-treated rods have a lower flexural rigidity, the stress and strain corresponding to the same bending moment are higher. Thus, plotting the fatigue lifetime by strain amplitude resolves the offset and the heat-treated specimen's fatigue lifetime is consistent with the baseline specimen's performance given the same amount of applied stress and strain.

On just the basis of the CIRFT rigidity measurements, as shown in Figure F- 11, the observed difference between the heat-treated and baseline could be considered within measurement uncertainty. However, given the good alignment of the strain-amplitude results and the results of mechanical tests (Appendix E), the heat-treatments clearly resulted in a lower flexural rigidity that led to a shorter fatigue lifetime for the same applied load. There are at least three potential sources for a reduction in flexural rigidity with FHT: (1) a permanent increase in cladding OD and a pellet-cladding gap that resulted from the increased pressure at temperature during the heat-treatment, (2) the annealing of irradiation defects resulting from the FHT, and (3) the reorientation of precipitated hydrides in the cladding during the heat-treatment that make it more susceptible to cladding fracture. The latter source is unlikely since the amount of hydride reorientation resulting from the sister rod heat treatments (Appendices A and B) varied by cladding alloy; only very short reoriented hydrides were observed on the Zirc-4/LT Zirc-4-clad rods, isolated hydrides were observed at the ID/OD on the ZIRLO-clad rods, and many reoriented hydrides on the M5-clad rods. Since reorientation was not observed for all heat-treated rods, the difference in flexural rigidity and fatigue lifetime is unlikely to be related to hydride reorientation. However, irradiation defect annealing could have occurred during FHT (particularly on the M5-clad rod as discussed in Appendix A), resulting in a lower overall rigidity of the FHT rod leading to a shorter fatigue lifetime. The other two potential sources are being investigated.

One specimen with visible GTRF marks was tested with the marks aligned (as was possible) with the highest cladding strain location, and the GTRF marks did not reduce the fatigue lifetime. The GTRF marks on this specimen are not considered representative or bounding; the specimen was selected based on availability only and further tests should be completed to fully explore the effect.

Table F- 6. Results arranged by paired specimens (baseline rods vs. heat-treated rods) for static/dynamic and dynamic CIRFT.

			Baseline rods						Heat-treated rods			
Specimen ID		Cladding type	Estimated specimen average burnup (GWd/MTU)	Cycles to failure	Flexural rigidity (N-m^2)	Applied strain amplitude (%)	Specimen ID		Cladding type	Estimated specimen average burnup (GWd/MTU)	Cycles to failure	Flexural rigidity (N-m^2)	Applied strain amplitude (%)
30AD05	0697 0850[1]	M5	58	3,368	28.35[2]	0.21[2]	30AE14	0672 0825[1]	M5	56	1,630	20.48	0.36
30AD05	2050 2203		59	133,000	28.73	0.08	30AE14	3156 3309		56	113,000	23.23	0.10
30AD05	2630 2783		59	22,300	27.97	0.18	30AE14	2850 3003		60	9,800	23.63	0.22
Average			59	52,889	28.35	0.13				57	41,477	22.45	0.23
3A1F05	1853 2006[1]	LT Zirc-4	56	1,300	19.34	0.39	F35P17	1855 2008	Zirc-4	53	525	28.74[2]	0.16[3]
3A1F05	3367 3520		44	214,000	29.74	0.06	F35P17	2027 2180		52	1,340,000	26.83	0.07
3A1F05	2025 2178		56	48,200	23.18	0.18							
3A1F05	3214 3367		48	3,450	21.56	0.19	F35P17	3159 3312[3]		47	773	30.66	0.15
Average			51	66,738	23.46	0.21				51	447,099	28.75	0.11
3D8E14	0719 0872[1]	ZIRLO	64	9,589	30.89[2]	0.11[2]							
3D8E14	2412 2565[4]		64	191,000	31.31	0.08							
3D8E14	2963 3116		62	39,700	28.06	0.15							
3D8E14	1178 1331		63	212,000	30.94	0.08							
6U3K09	2310 2463		59	17,500	30.22	0.20	3F9N05	0719 0872[1]	ZIRLO	59	3,540	18.01	0.41
6U3K09	2463 2616		59	39,200	32.39	0.13	3F9N05	2329 2482		59	189,000	22.55	0.10
6U3K09	2635 2788		58	110,000	37.10	0.08	3F9N05	2710 2863		57	33,000	21.85	0.19
6U3K09	3200 3353		50	34,900	30.04	0.15							
6U3K09	3353 3506		46	14,100	27.03	0.21							
Average			60	50,400	32.44	0.14				58	75,180	20.80	0.23

1. Dynamically tested following a static test.
2. Estimated.
3. Erratic load cell data were recorded during the test. The applied moment and strain amplitude was likely higher.
4. Specimen had a GTRF mark in the gauge section that was aligned (as possible) with the expected maximum strain location.

F-7.5 Imaging of the fractured specimens

To provide additional information regarding how the specimens fractured, magnified images were obtained using the IMGA facility at the Irradiated Fuels Examination Laboratory. The images provide information about the location at which the fatigue crack propagated to fracture and about whether the fracture occurred at a pellet-pellet interface.

In many cases, the locations of the highest strains are visible on the specimen surface as dull oval areas, as shown on Figure F- 14. Rods that had higher oxide thicknesses had some additional spalling during the test, and this is particularly visible in the LT Zirc-4 clad rods, such as 3A1F05-1853-2006 (Figure F- 27).

The M5-clad specimens tended to break cleanly around the circumference of the rod, but in the body of the pellet, rather than at the pellet-pellet interface. Three of the six specimens broke in the center third of the specimen, while the other three broke near or inside a dogbone grip.

The ZIRLO-clad specimens broke differently, depending upon the parent rod. The baseline 3D8E14 specimens tended to break cleanly around the circumference of the rod but at approximately a 30-degree angle. Three of the four specimens broke at pellet-pellet interfaces and the cladding fracture extended into the body of a pellet. Three of the four specimens broke in the center third and one broke near the dogbone. All 6U3K09 specimens broke circumferentially; three of the five broke near or inside the dogbone grip and three of the five broke at pellet-pellet interfaces. Two of the 6U3K09 specimens had double fractures—a partial circumference break in the center third with the full fracture near the dogbone. All specimens from the FHT rod 3F9N05 broke in the center third of the specimen; two had a flat circumferential break at the pellet-pellet interface, and one of the three broke in the body of a pellet at approximately a 30-degree angle.

The Zirc-4-clad specimens all broke dramatically in the same way with a flat circumferential crack around half the rod that was sheared around the half of the rod and at a pellet-pellet interface. One specimen fractured in the center third of the dogbone, and two fractured near the dogbone grip. The Zirc-4 clad fractures are jagged, and the sheared sections span a full pellet length or more, although the crack appears to have nucleated at a pellet-pellet interface. The baseline LT Zirc-4-clad specimens appear similar to the LT Zirc-4 specimens at higher rod elevations and similar to the ZIRLO rods at lower elevations. Two fractured in the center third of the specimen, and three fractured at pellet-pellet interfaces.

There does not appear to be a difference in the fracture mode from the baseline to heat-treated rods. The specimens that had fatigue lifetimes lower than other data did not fracture in an anomalous manner.

Table F- 7 summarizes the visual observations of CIRFT-fractured dogbones.

Table F- 7. Summary of visual observations of CIRFT-fractured dogbones.

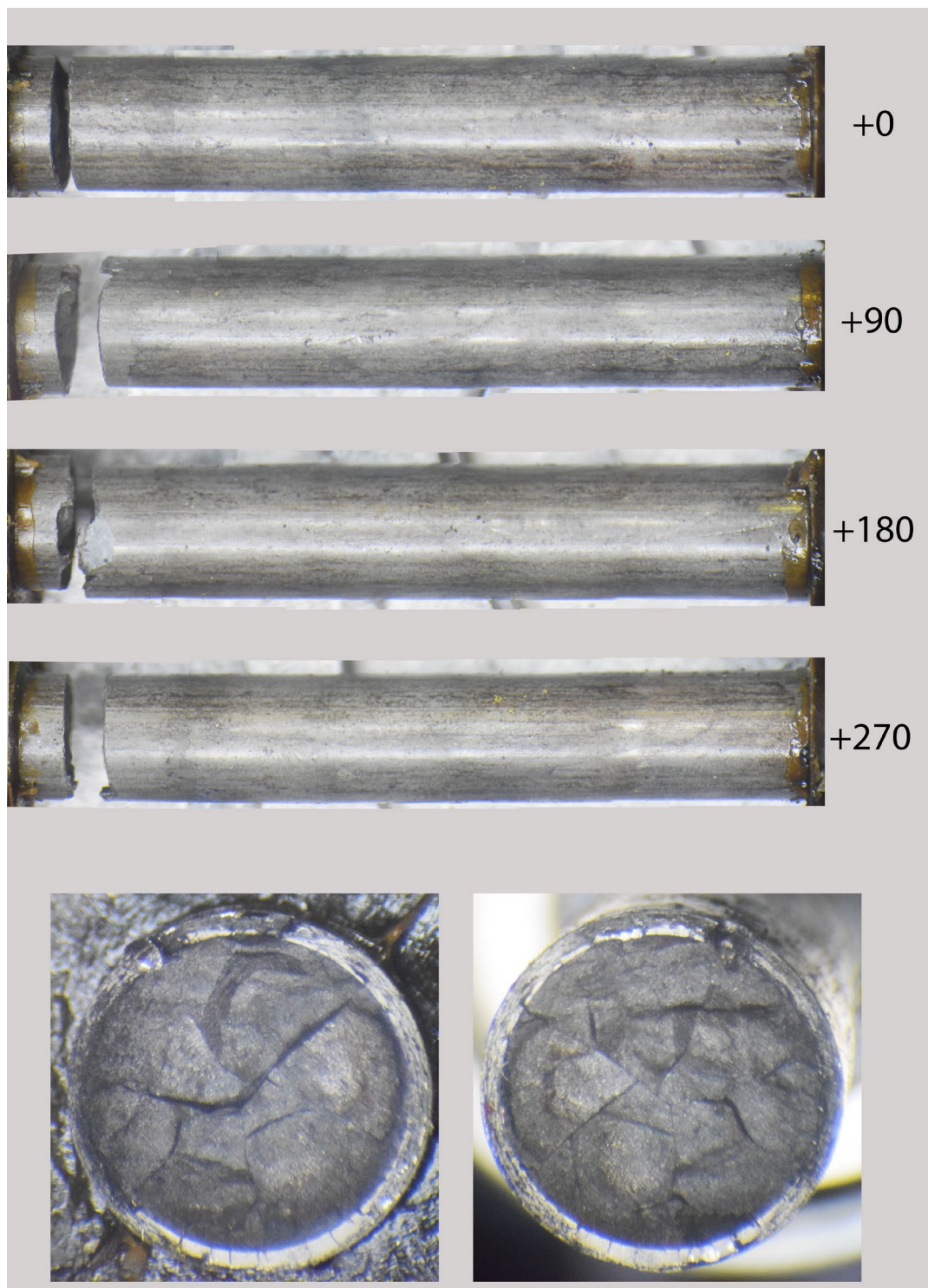| Rod type	Cladding material	Estimated specimen-average burnup (GWd/MTU)	Specimen ID	Fracture location	Cladding fracture orientation	Pellet fracture appearance
17x17	M5	58	30AD05-0697-0850	Center third	Circumferential	Pellet body
17x17	M5	59	30AD05-2050-2203	In grip	Circumferential	Pellet body
17x17	M5	59	30AD05-2630-2783	Near grip	Circumferential with some flaring and uneven ends	Pellet body but very near end
17x17	M5	56	30AE14-0672-0825	Center third	Circumferential with some flaring and uneven ends	Pellet body
17x17	M5	60	30AE14-2850-3003	Near grip	Circumferential	Pellet body
17x17	M5	56	30AE14-3156-3309	Center third	Circumferential with partial shearing	Pellet body
17x17	Zirc-4	66	F35P17-1855-2008	Center third	Partially sheared	At pellet end and through body
17x17	Zirc-4	66	F35P17-2027-2180	Near grip	Partially sheared	At pellet end
17x17	Zirc-4	62	F35P17-3159-3312	Near grip	Partially sheared	At pellet end
17x17	LT Zirc-4	48	3A1F05-3214-3367	In grip	Partially sheared	Pellet end
17x17	LT Zirc-4	56	3A1F05-1853-2006	Near grip	Circumferential at ~30-degree angle	Just off pellet end
17x17	LT Zirc-4	56	3A1F05-2025-2178	Center third	circumferential	Pellet end
17x17	LT Zirc-4	44	3A1F05-3367-3520	Center third	Partially sheared	Pellet body
17x17	ZIRLO	64	3D8E14-0719-0872	Near grip	Circumferential with partial shearing	Pellet end
17x17	ZIRLO	64	3D8E14-2412-2565	Center third	Circumferential at ~30-degree angle	Pellet body
17x17	ZIRLO	62	3D8E14-2963-3116	Center third	circumferential	Pellet end
17x17	ZIRLO	63	3D8E14-1178-1331	Center third	Circumferential. GTRF mark obliterated.	Pellet end
17x17	ZIRLO	59	3F9N05-0719-0872[3]	Center third	Circumferential at ~30-degree angle	Pellet body
17x17	ZIRLO	59	3F9N05-2329-2482	Center third	Circumferential	Pellet end
17x17	ZIRLO	57	3F9N05-2710-2863	Center third	Circumferential	Pellet end
17x17	ZIRLO	59	6U3K09-2310-2463	Center and near grip; double fracture	Circumferential	Pellet end
17x17	ZIRLO	59	6U3K09-2463-2616	Near grip	Circumferential	Pellet end
17x17	ZIRLO	58	6U3K09-2635-2788	At grip	Circumferential	Pellet end
17x17	ZIRLO	50	6U3K09-3200-3353	Center third and near grip, double fracture	Circumferential	Pellet body
17x17	ZIRLO	46	6U3K09-3353-3506	Near grip	Circumferential	Pellet body

+0

+90

+180

+270

Figure F- 13. 6U3K09-3353-3506 post fatigue test condition.

Second crack initiated but not fully separated around the circumference.

+0

+90

Dull oval area indicative of highest strain location.

+180

+270
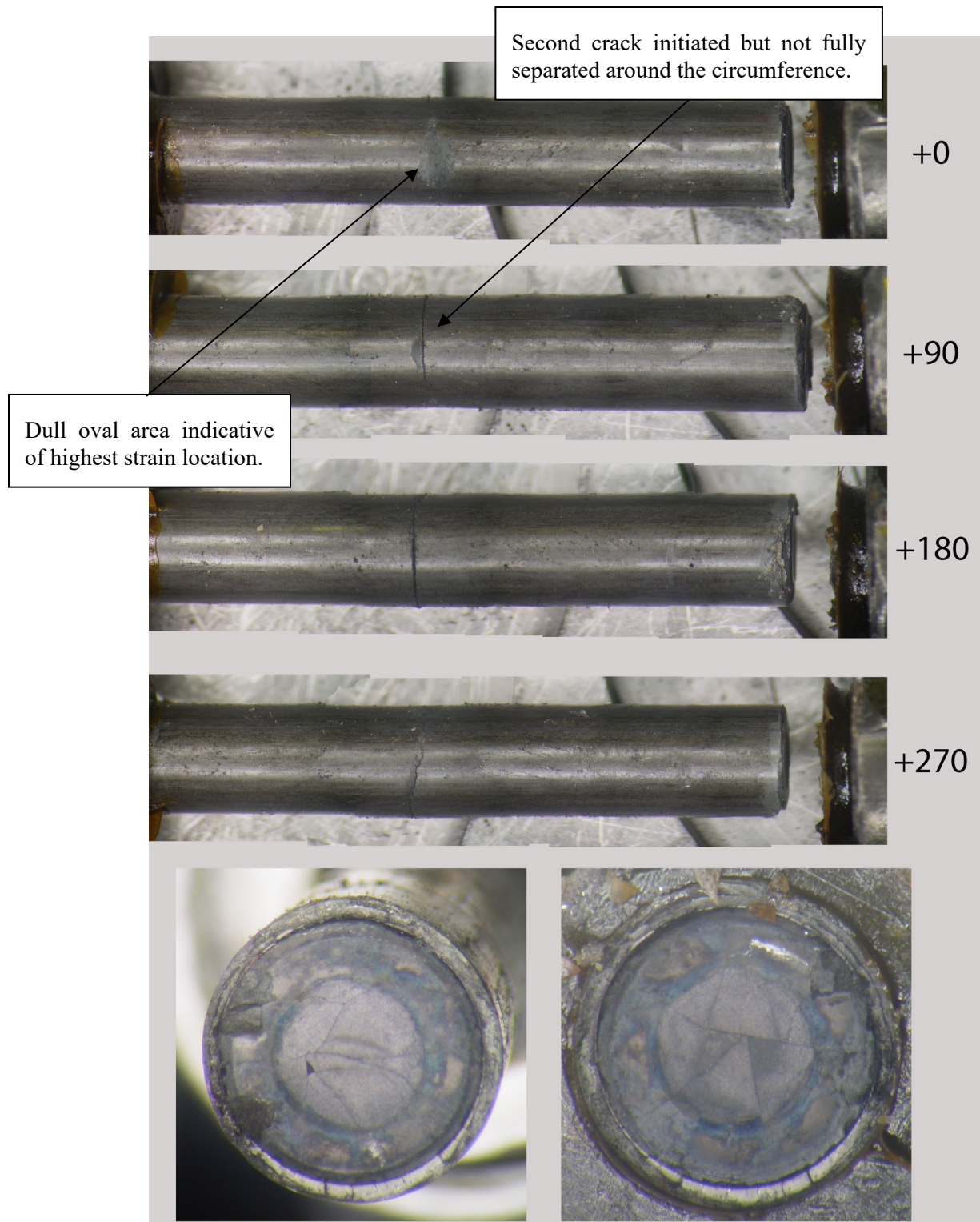
Figure F- 14. 6U3K09-2310-2463 post fatigue test condition.

Second crack initiated but not fully separated around the circumference.

+0

+45

+90

+135

+180

+225

+270

+315
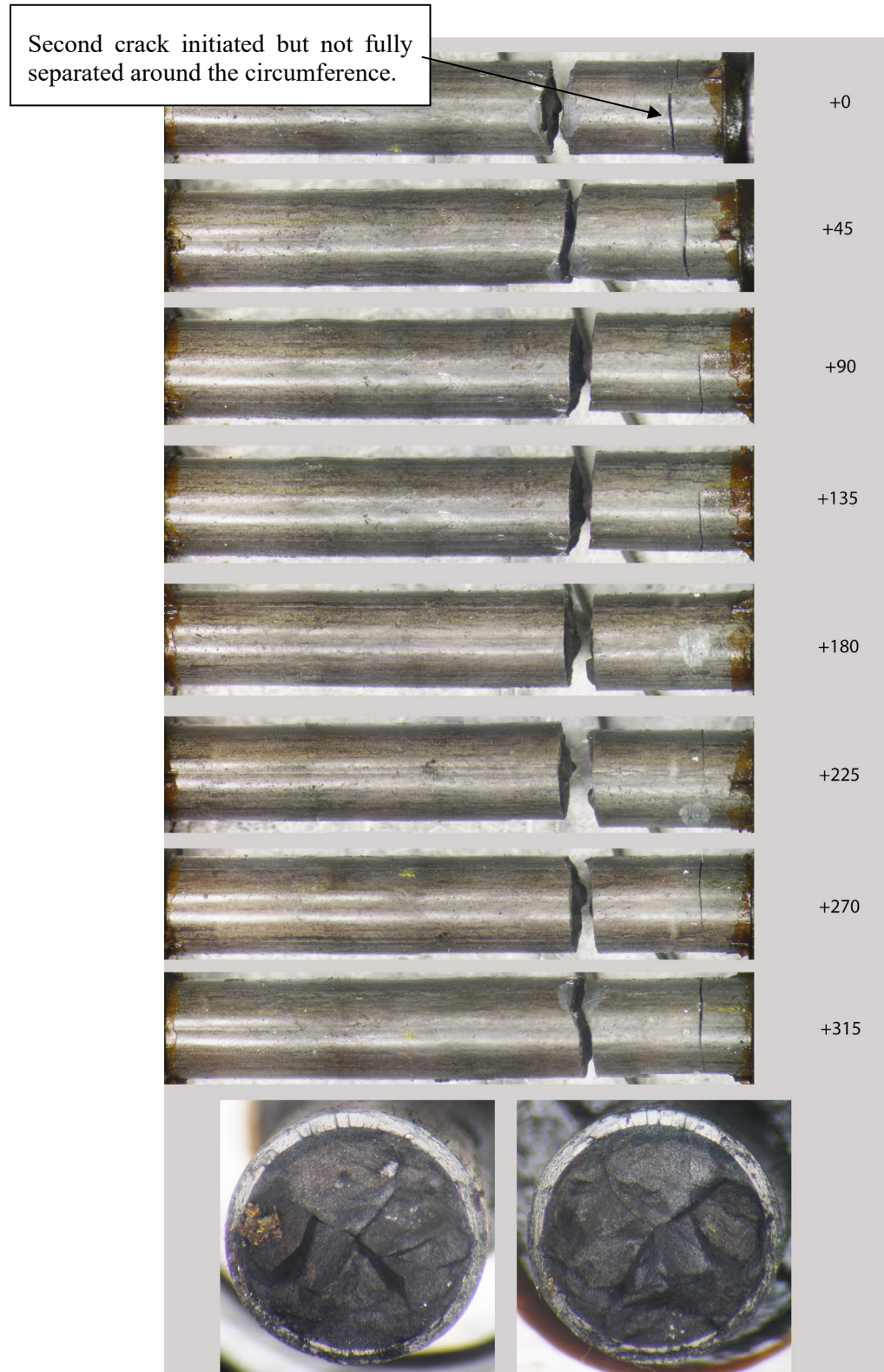
Figure F- 15. 6U3K09-3200-3353 post fatigue test condition.
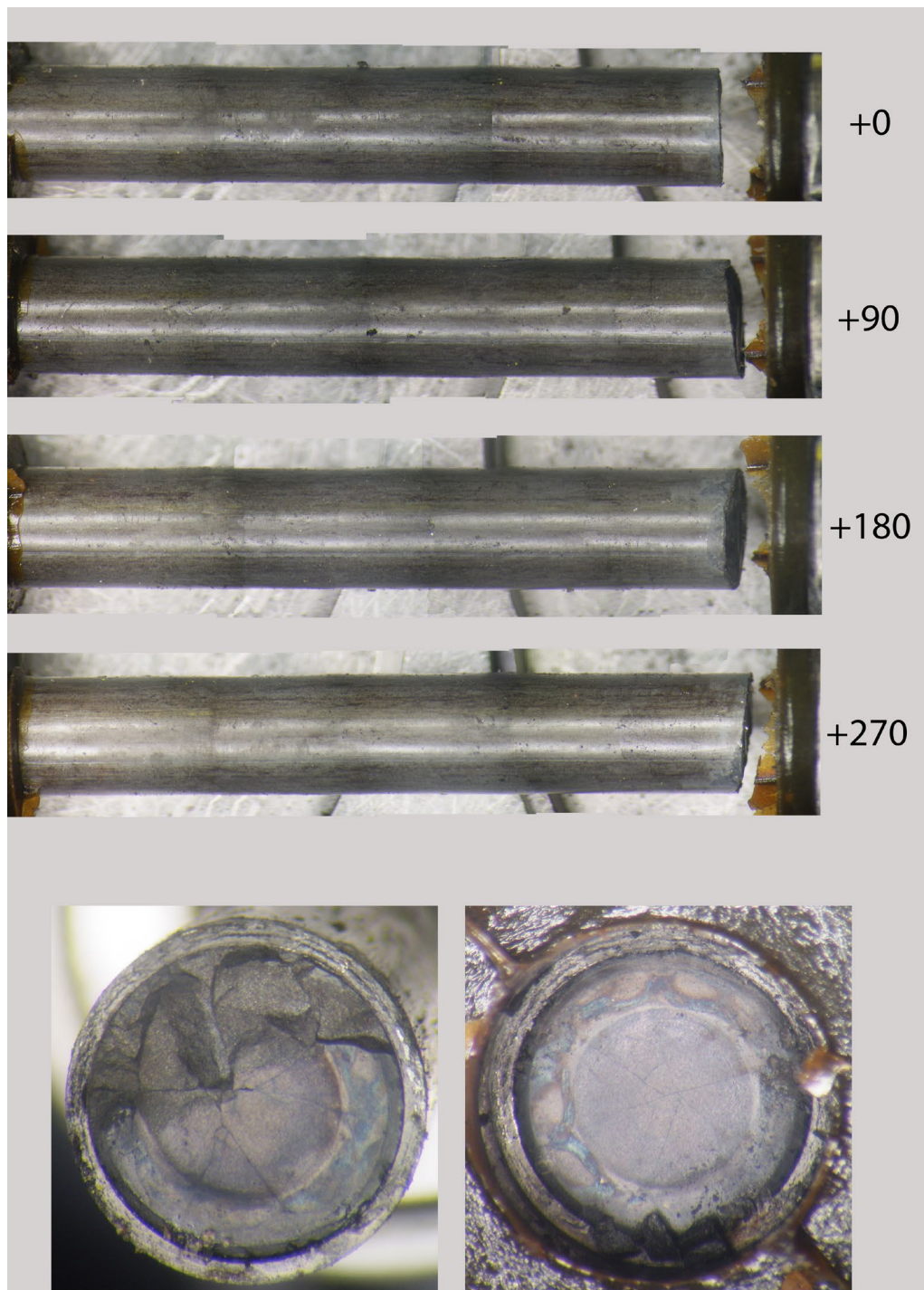
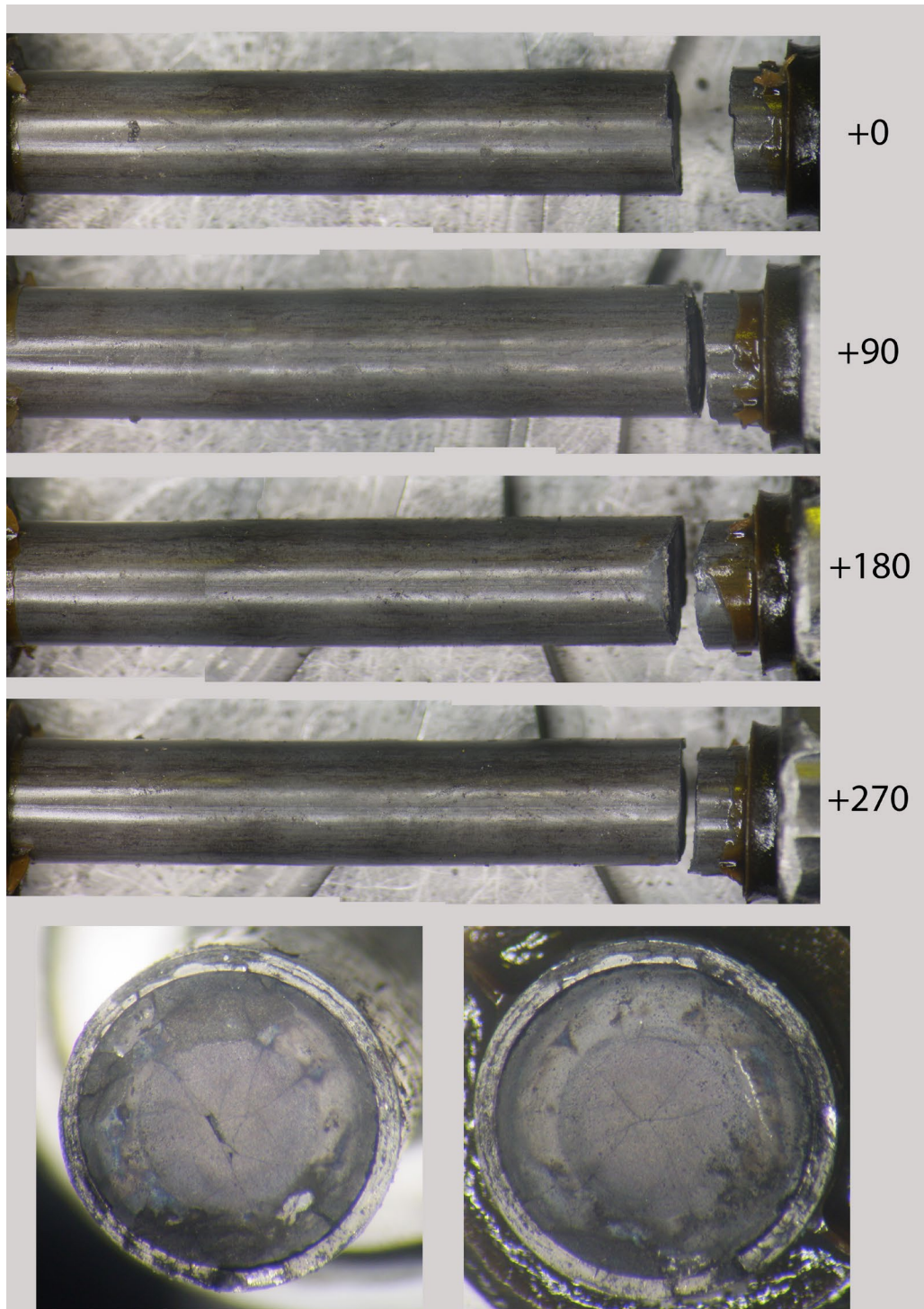**Figure F- 16. 6U3K09-2635-2788 post fatigue test condition.**

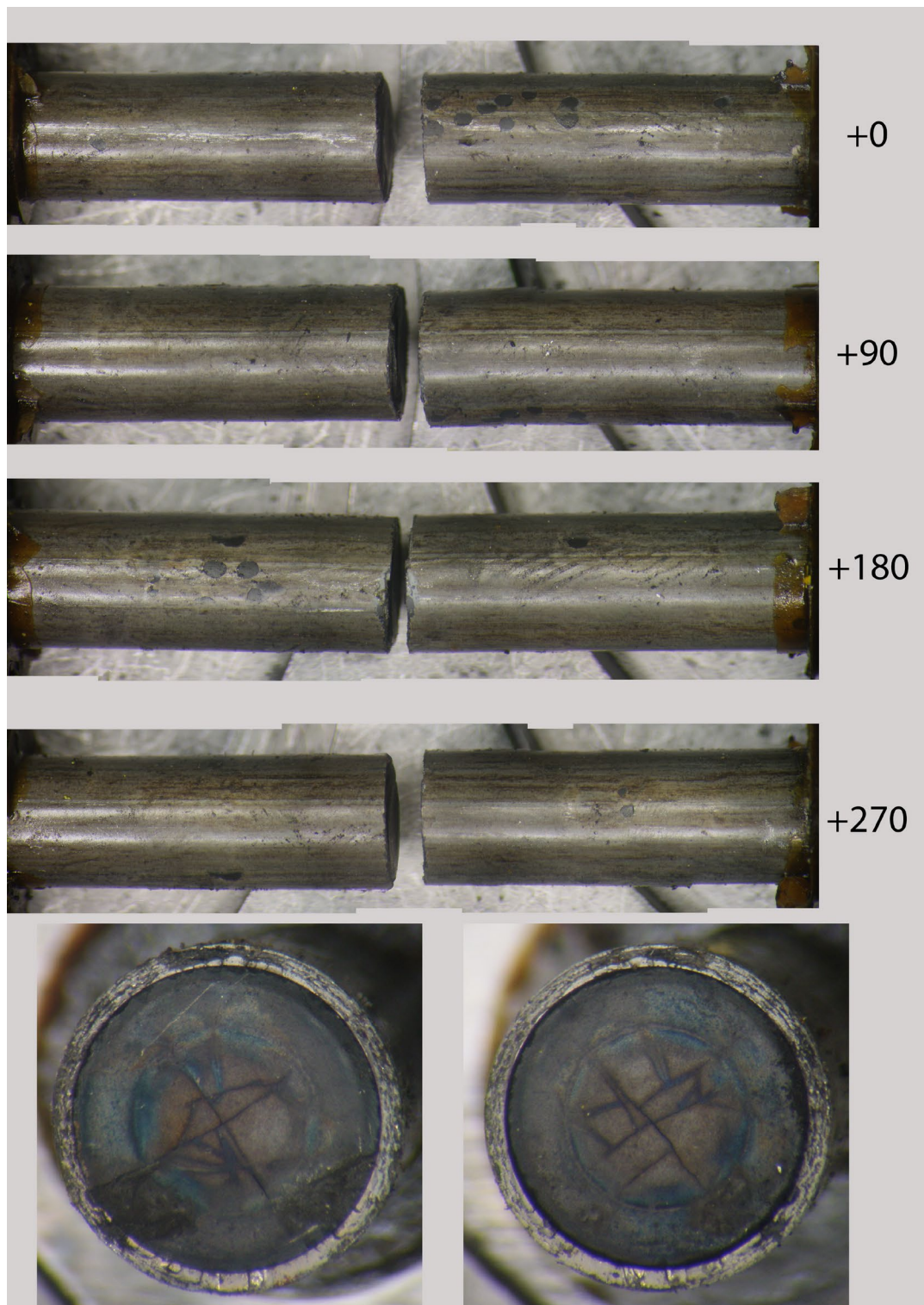**Figure F- 17. 6U3K09-2463-2616 post fatigue test condition.**

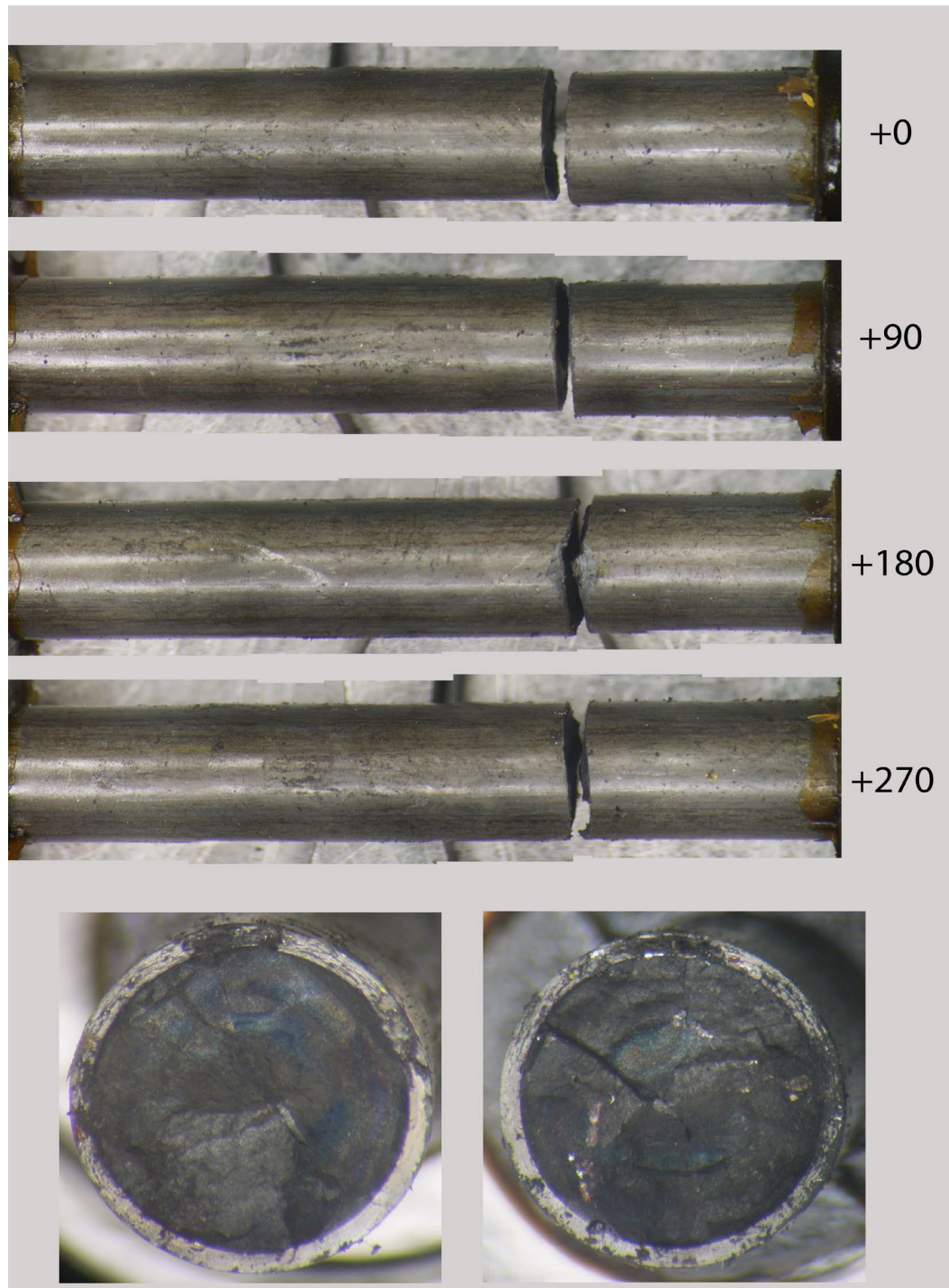**Figure F- 18. 3F9N05-2710-2863 post fatigue test condition.**

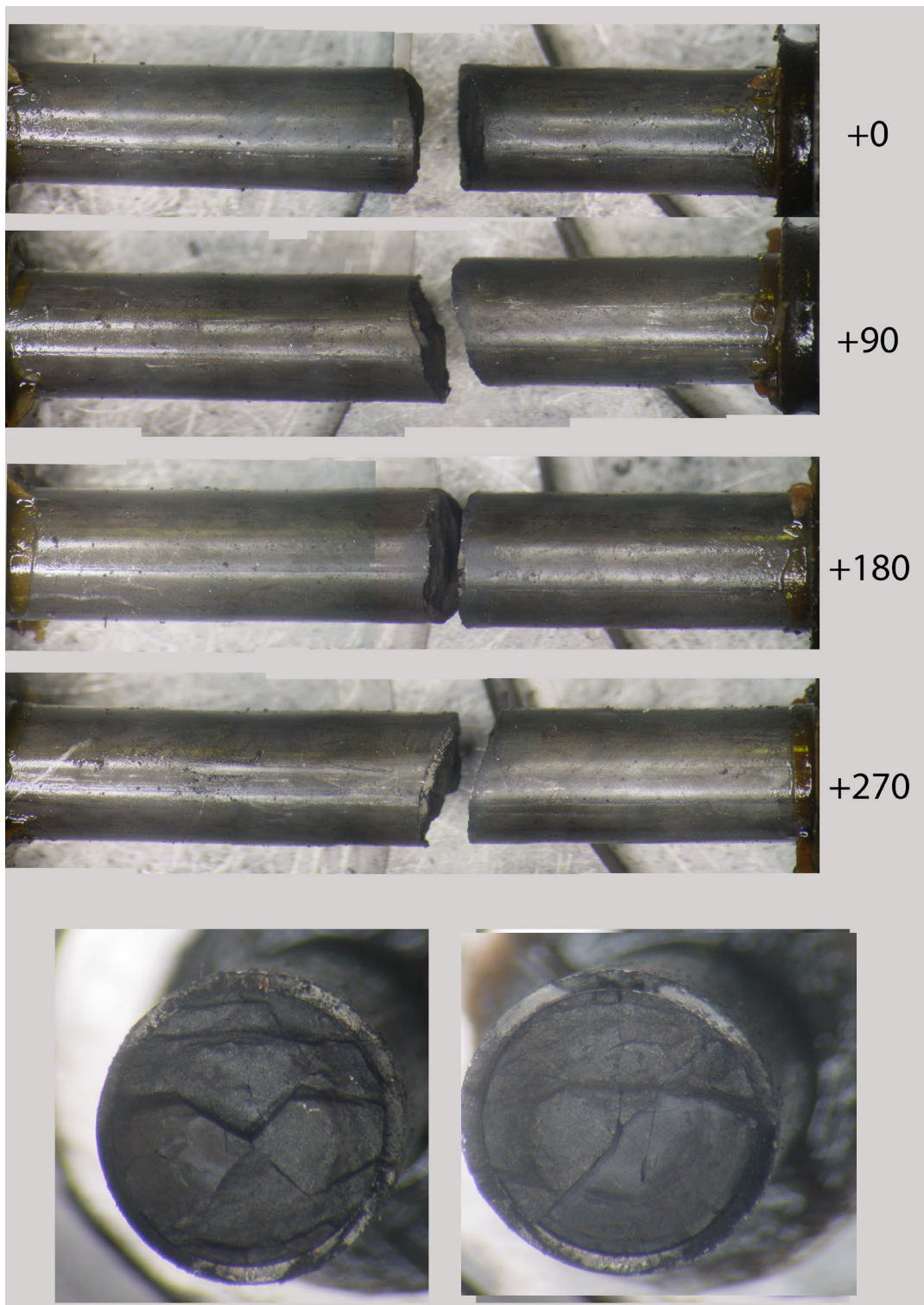**Figure F- 19. 3F9N05-2329-2482 post fatigue test condition.**

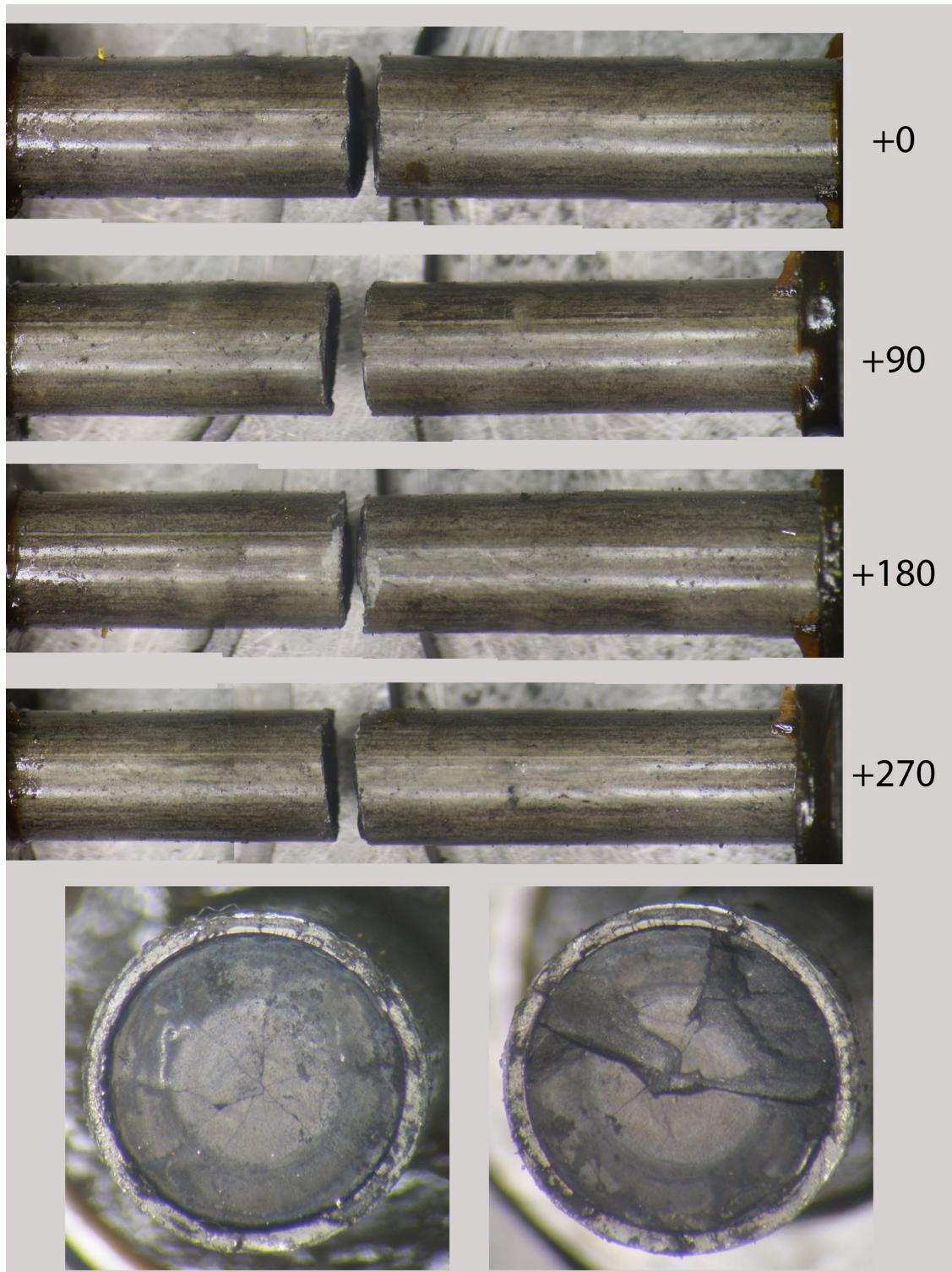**Figure F- 20. 3F9N05-0719-0872 post fatigue test condition.**

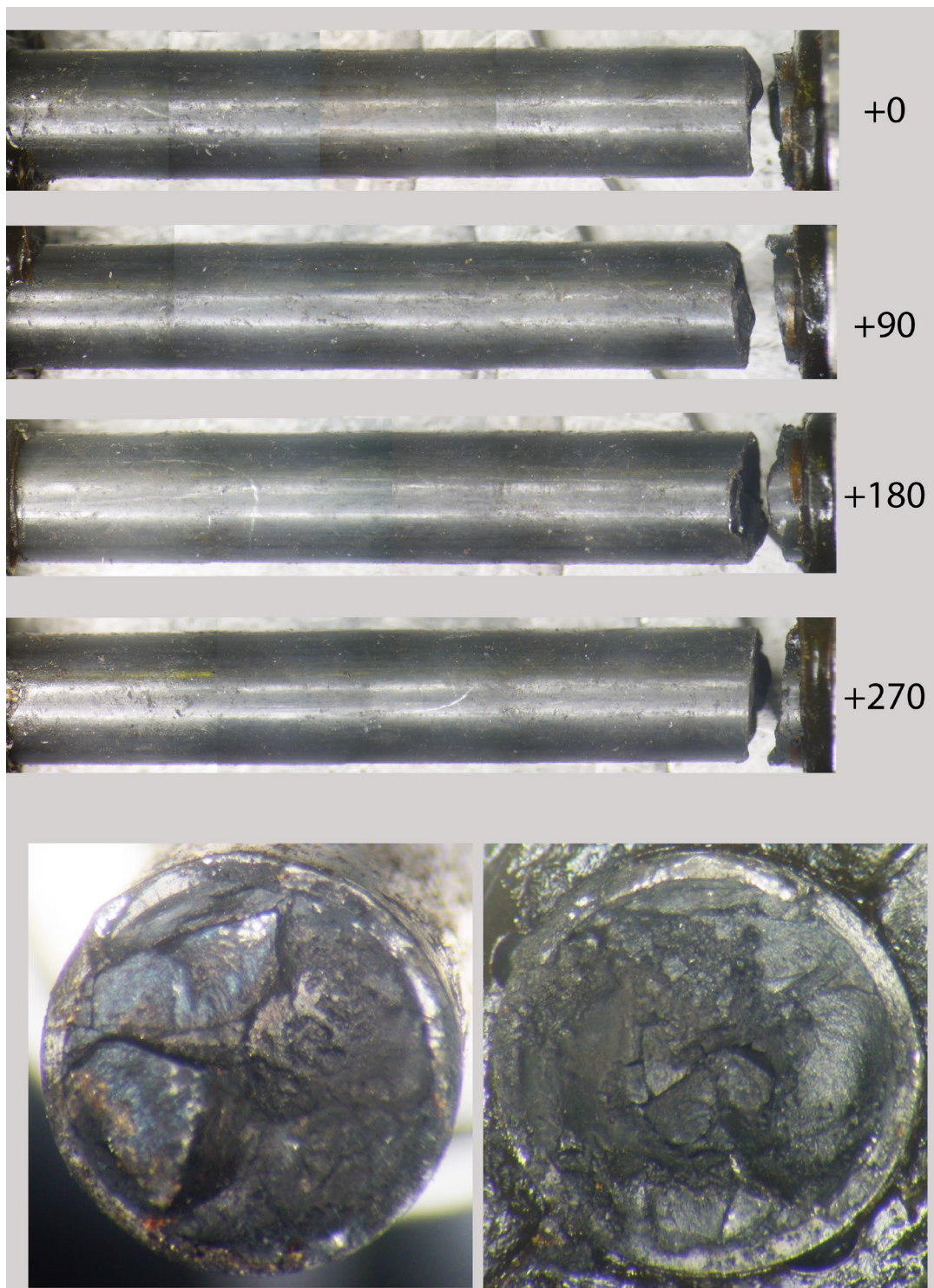**Figure F- 21. 3D8E14-2963-3116 post fatigue test condition.**

Figure F- 22. 30AD05-2630-2783 post fatigue test condition.
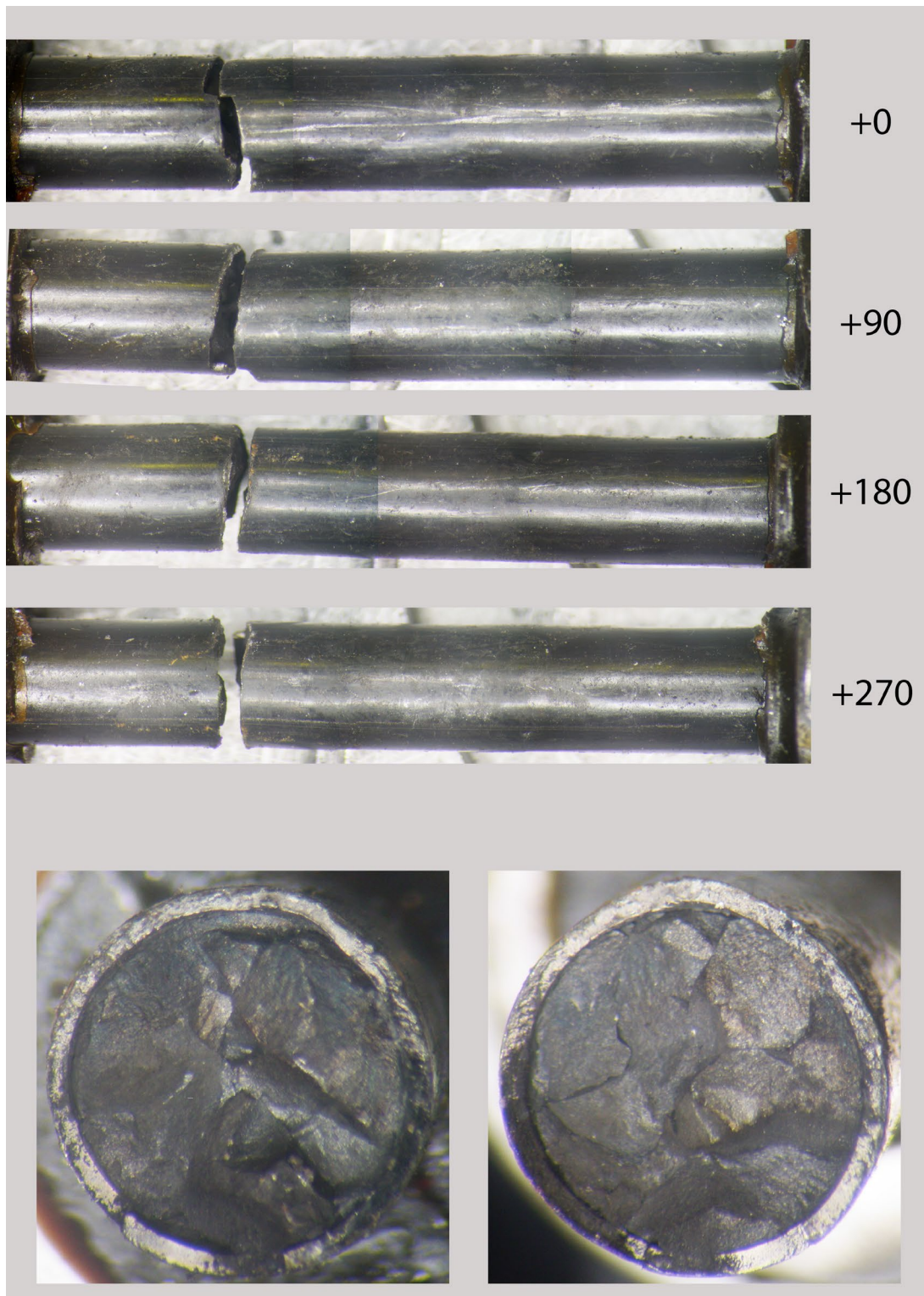
Figure F- 23. 30AE14-0672-0825 post fatigue test condition.
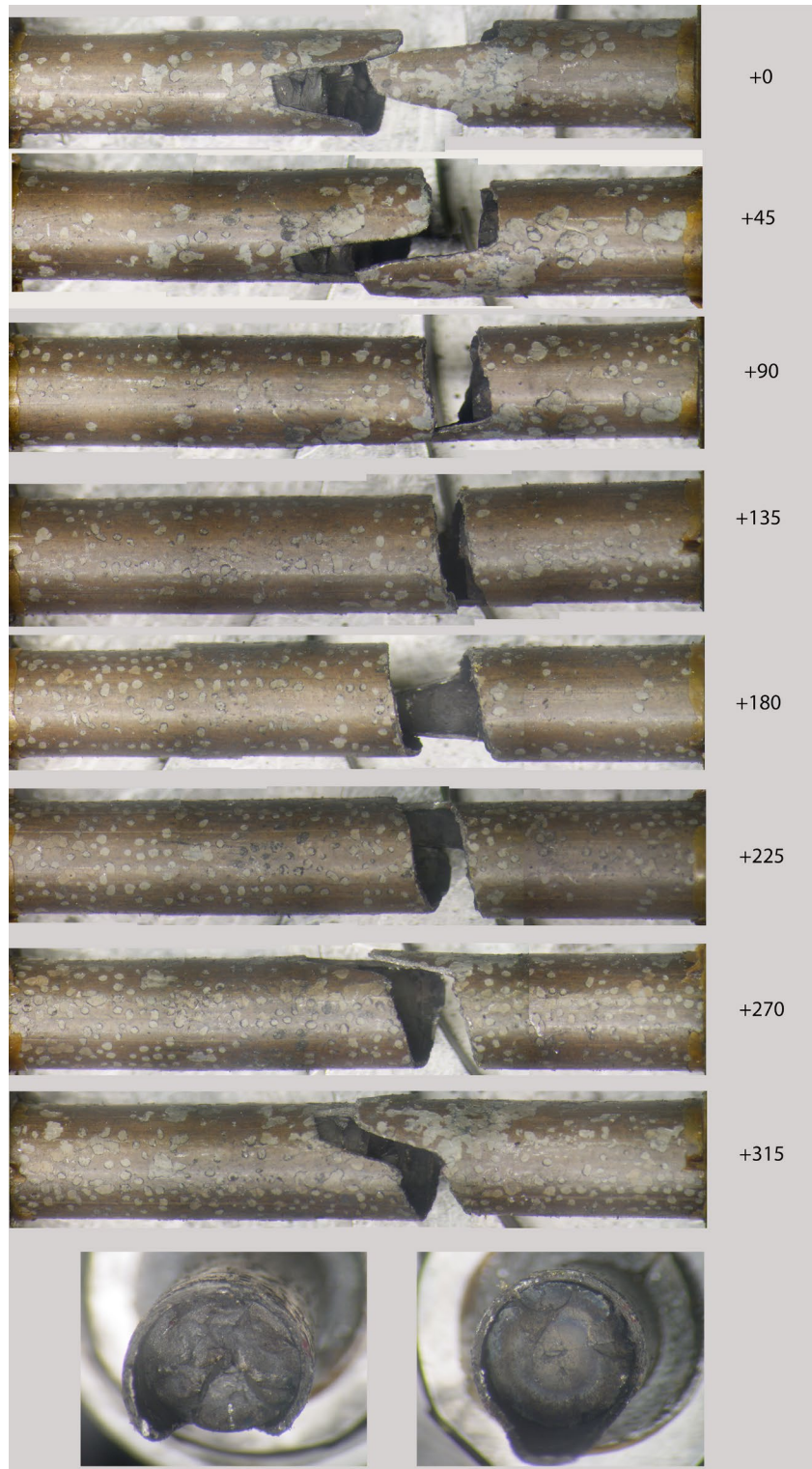
Figure F- 24. F35P17-1855-2008 post fatigue test condition.
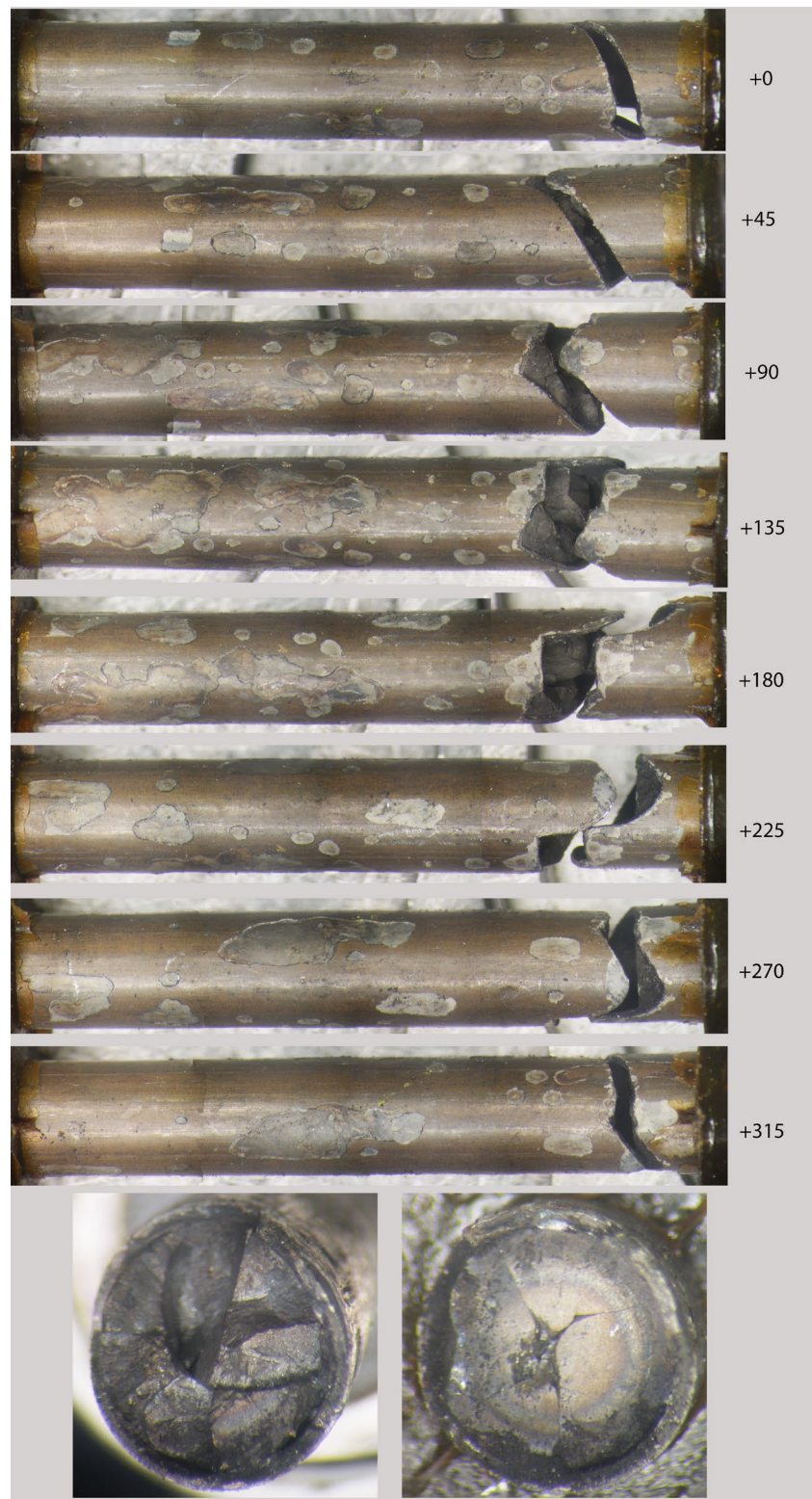
Figure F- 25. F35P17-3159-3312 post fatigue test condition.
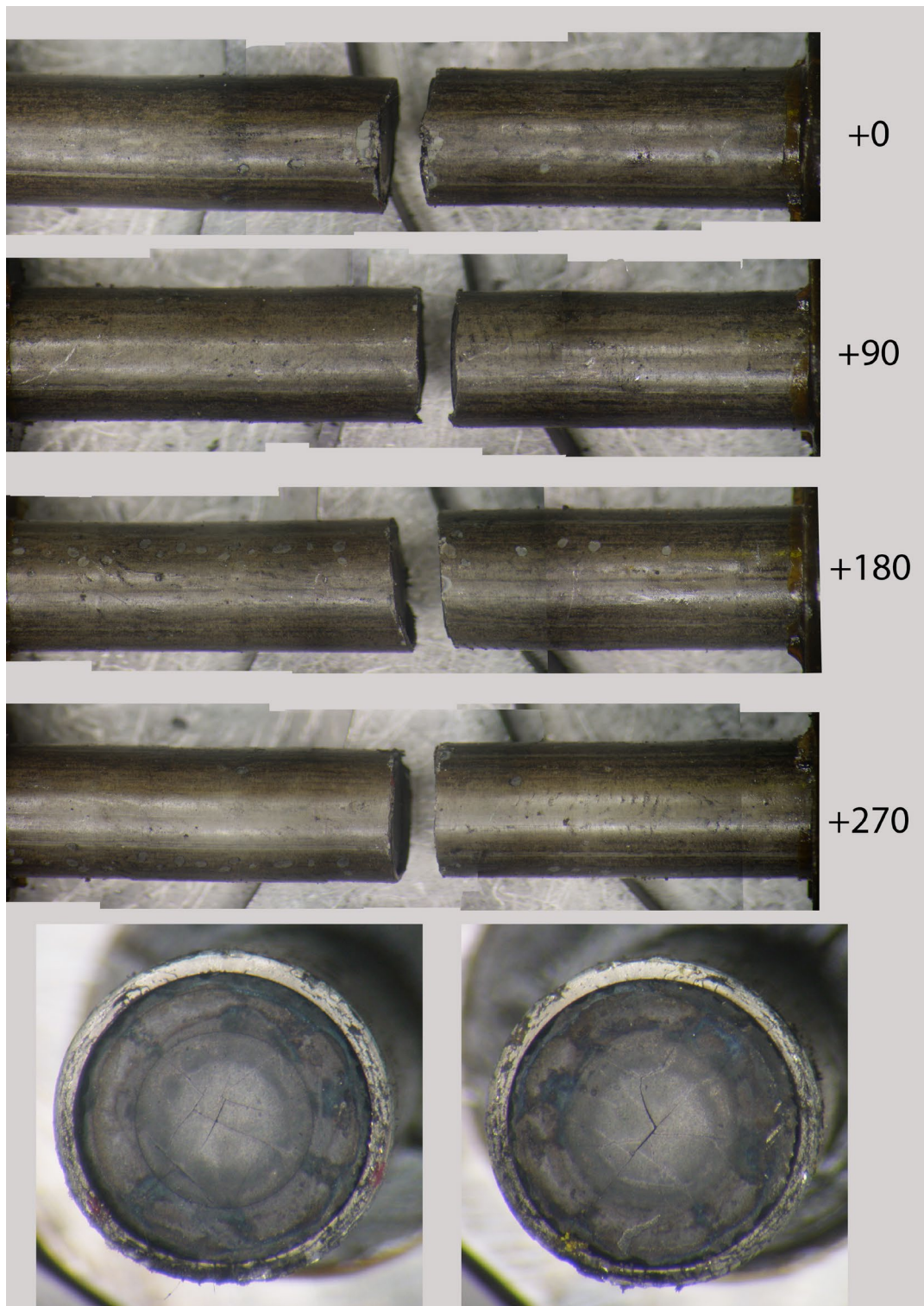
Figure F- 26. 3A1F05-2025-2178 post fatigue test condition.

+0

+45

+90

+135

+180

+225

+270

+315
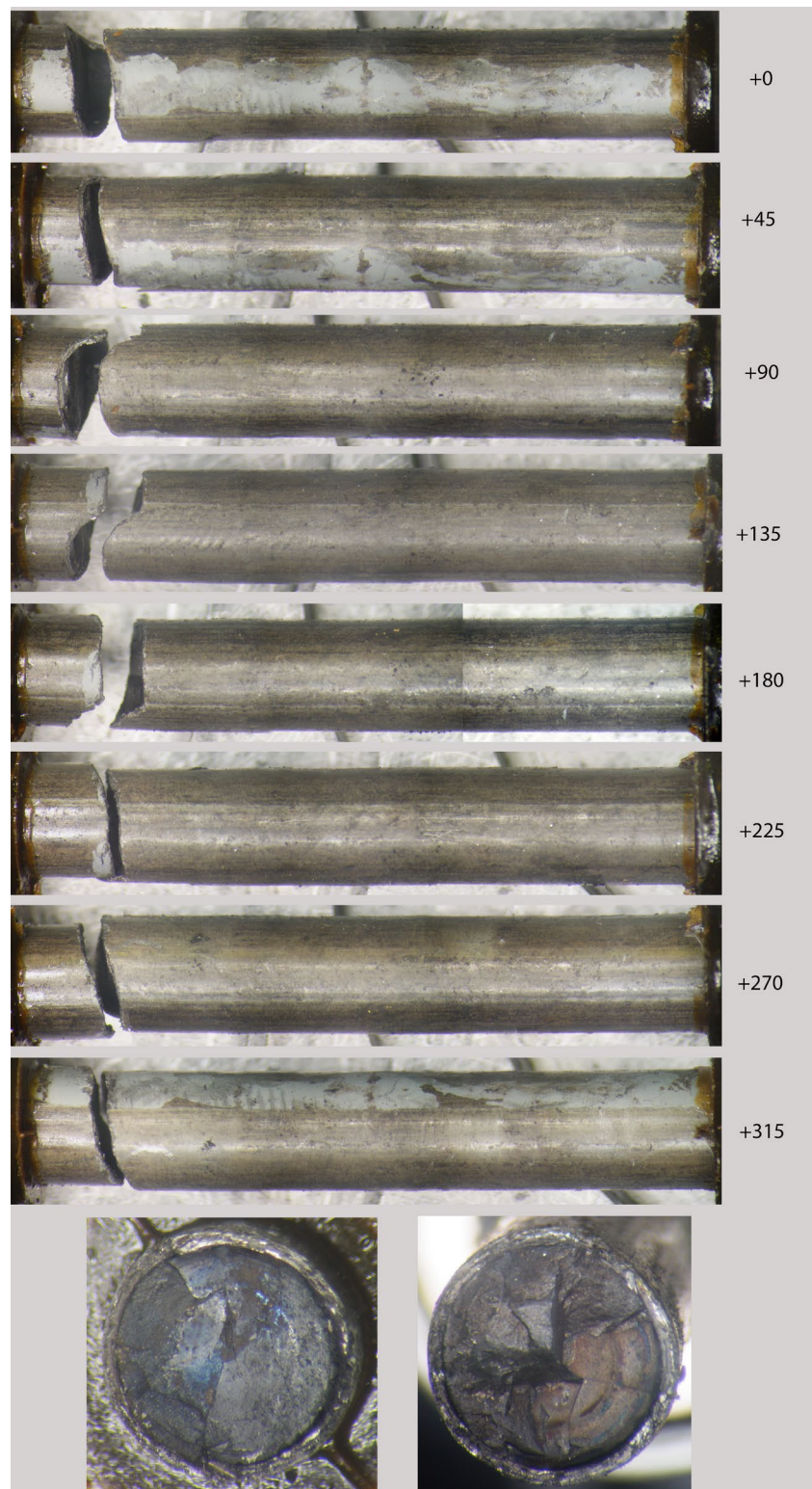
Figure F- 27. 3A1F05-1853-2006 post fatigue test condition.
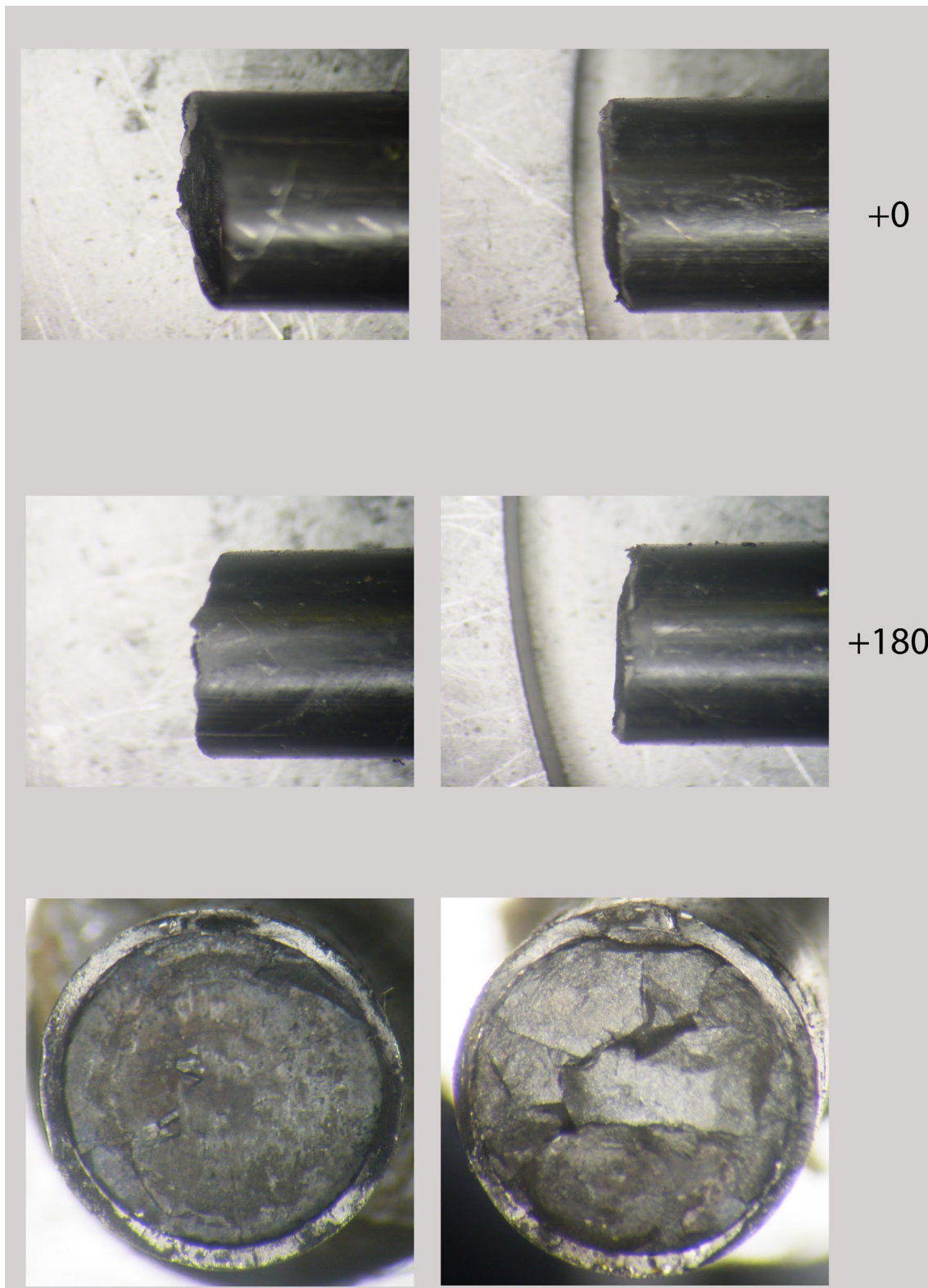
Figure F- 28. 30AD05-0697-0850 post fatigue test condition (broken ends only).
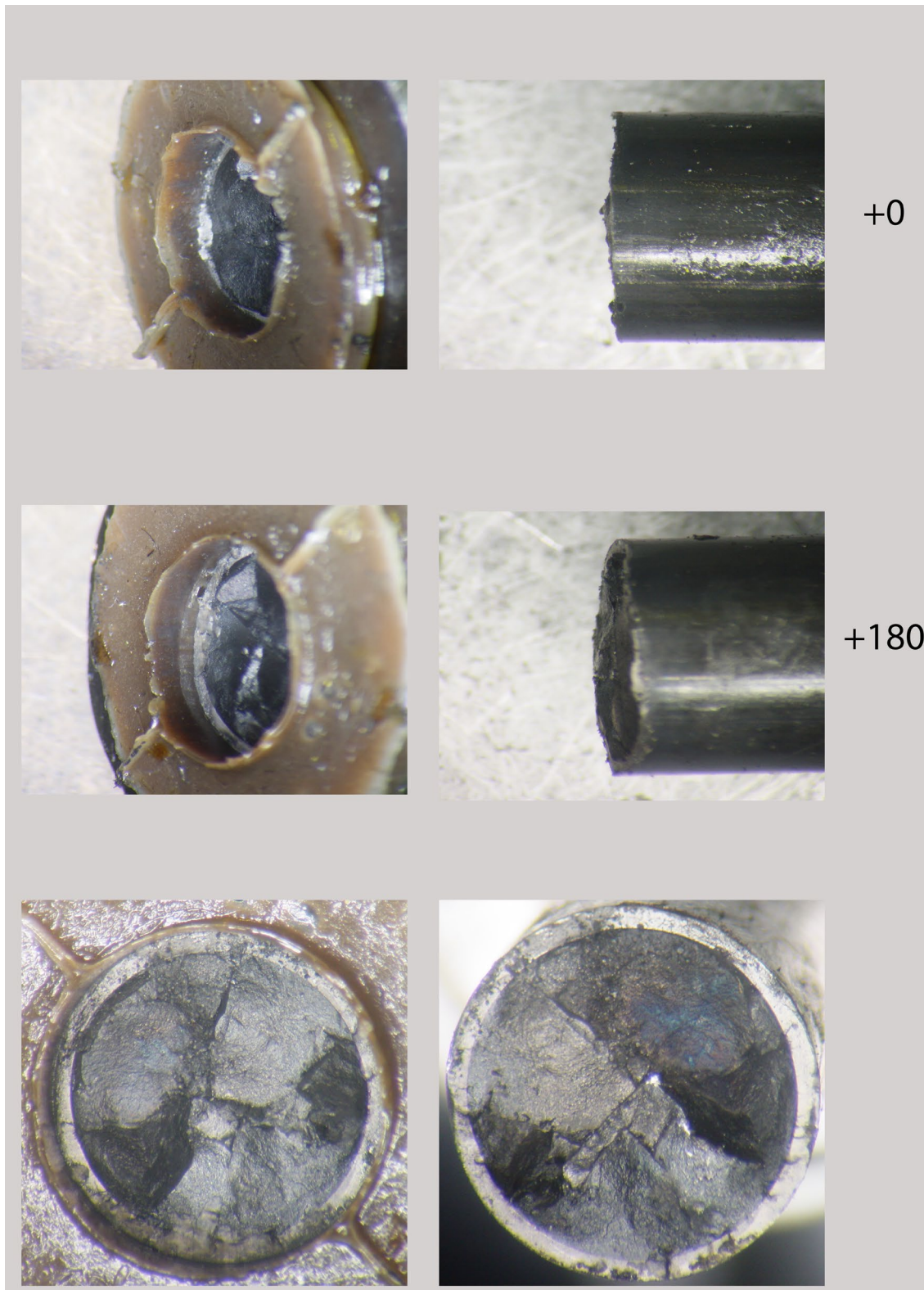
Figure F- 29. 30AD05-2050-2203 post fatigue test condition (broken ends only).
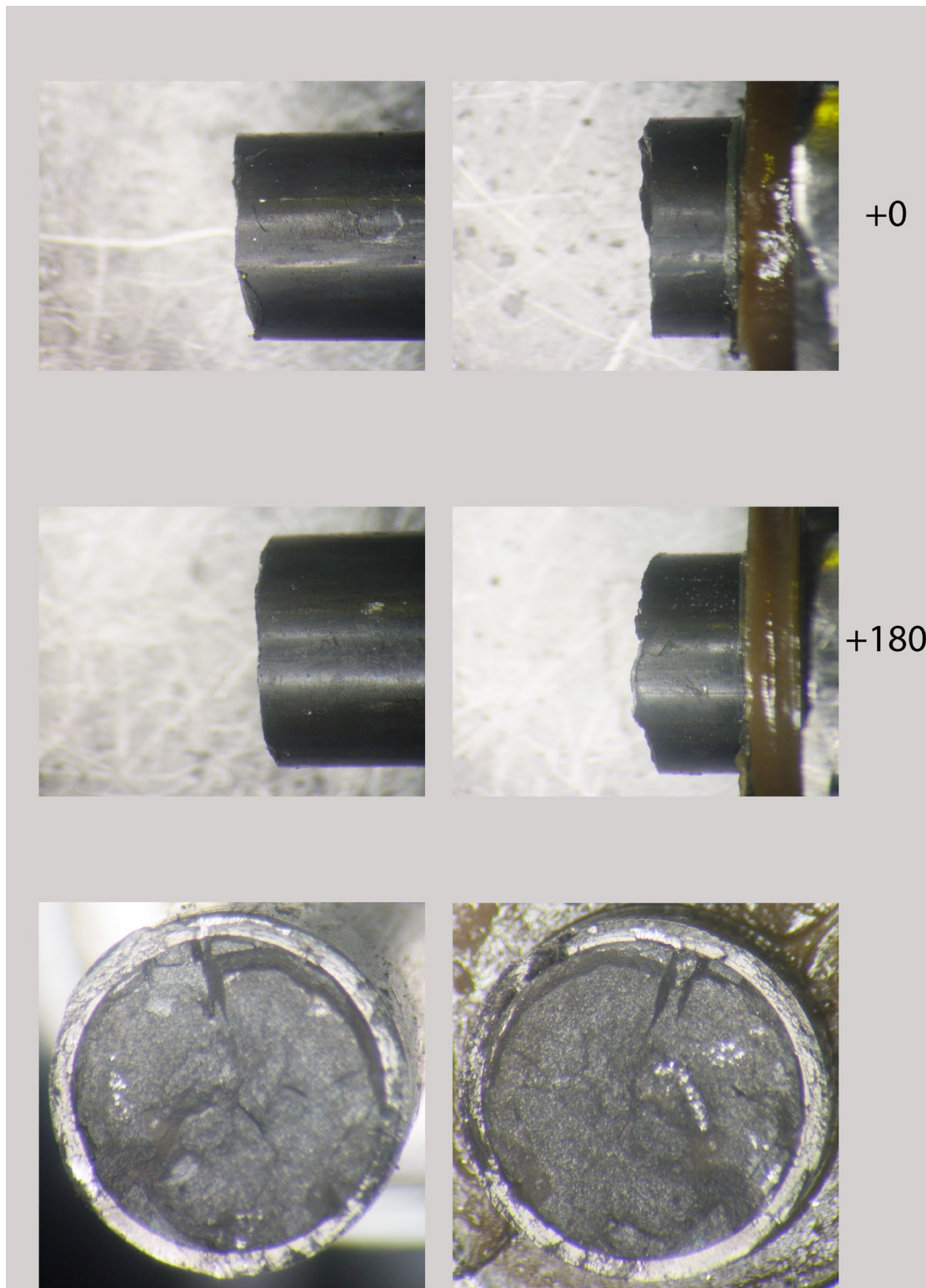
Figure F- 30. 30AE14-2850-3003 post fatigue test condition (broken ends only).

Figure F- 31. 30AE14-3156-3309 post fatigue test condition (broken ends only).
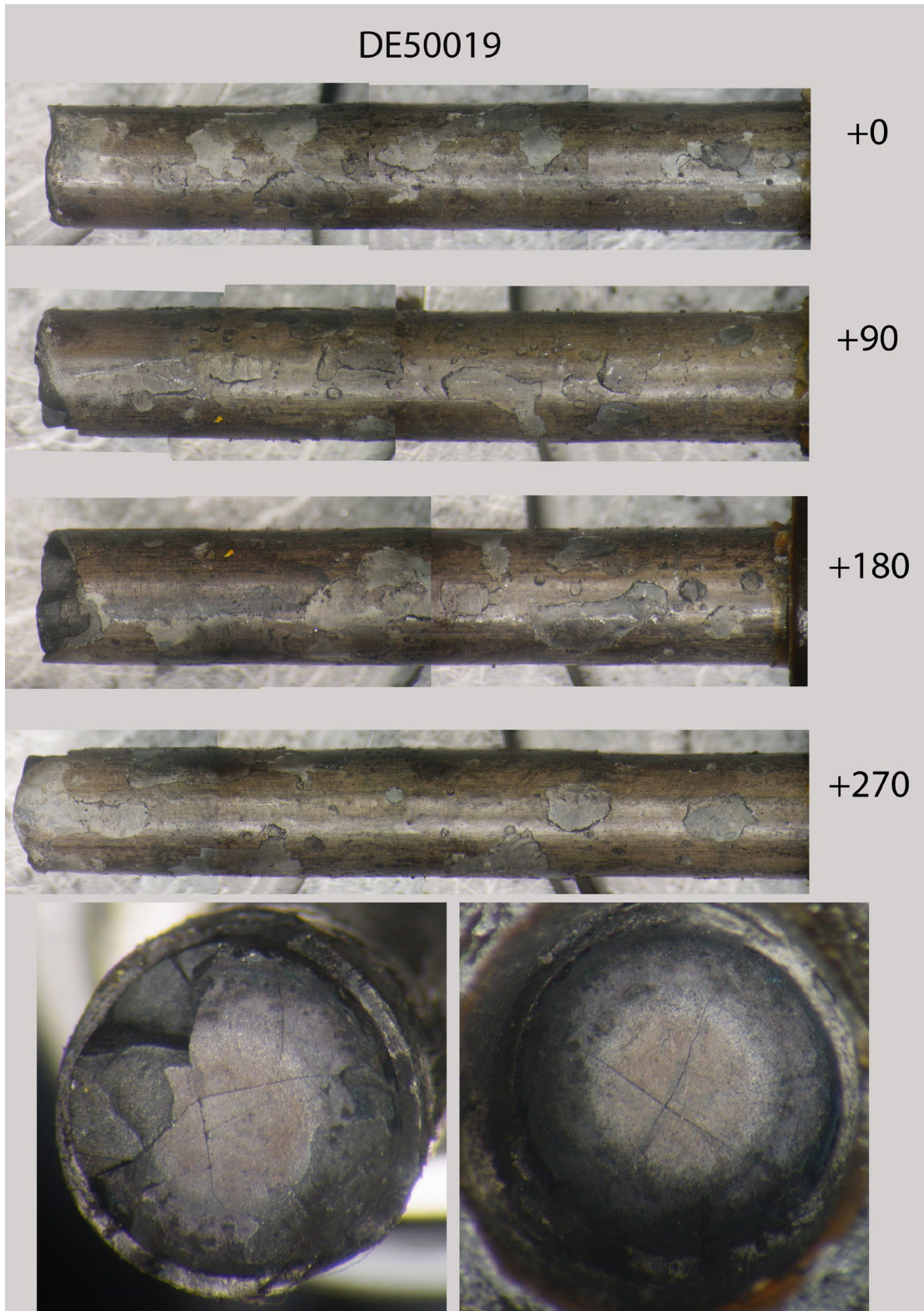
Figure F- 32. 3A1F05-3214-3367 post fatigue test condition.
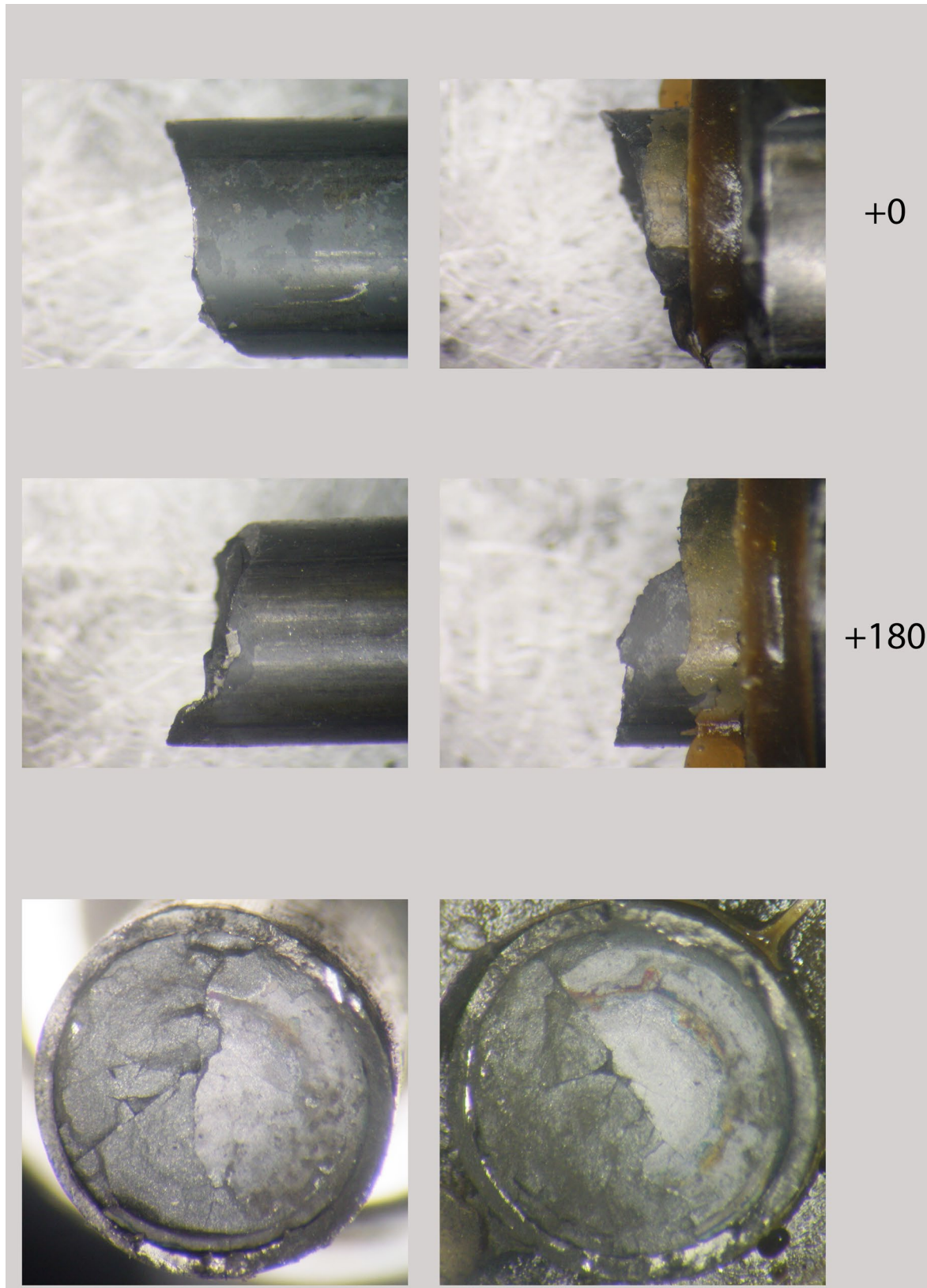
Figure F- 33. 3D8E14-719-872 post fatigue test condition.

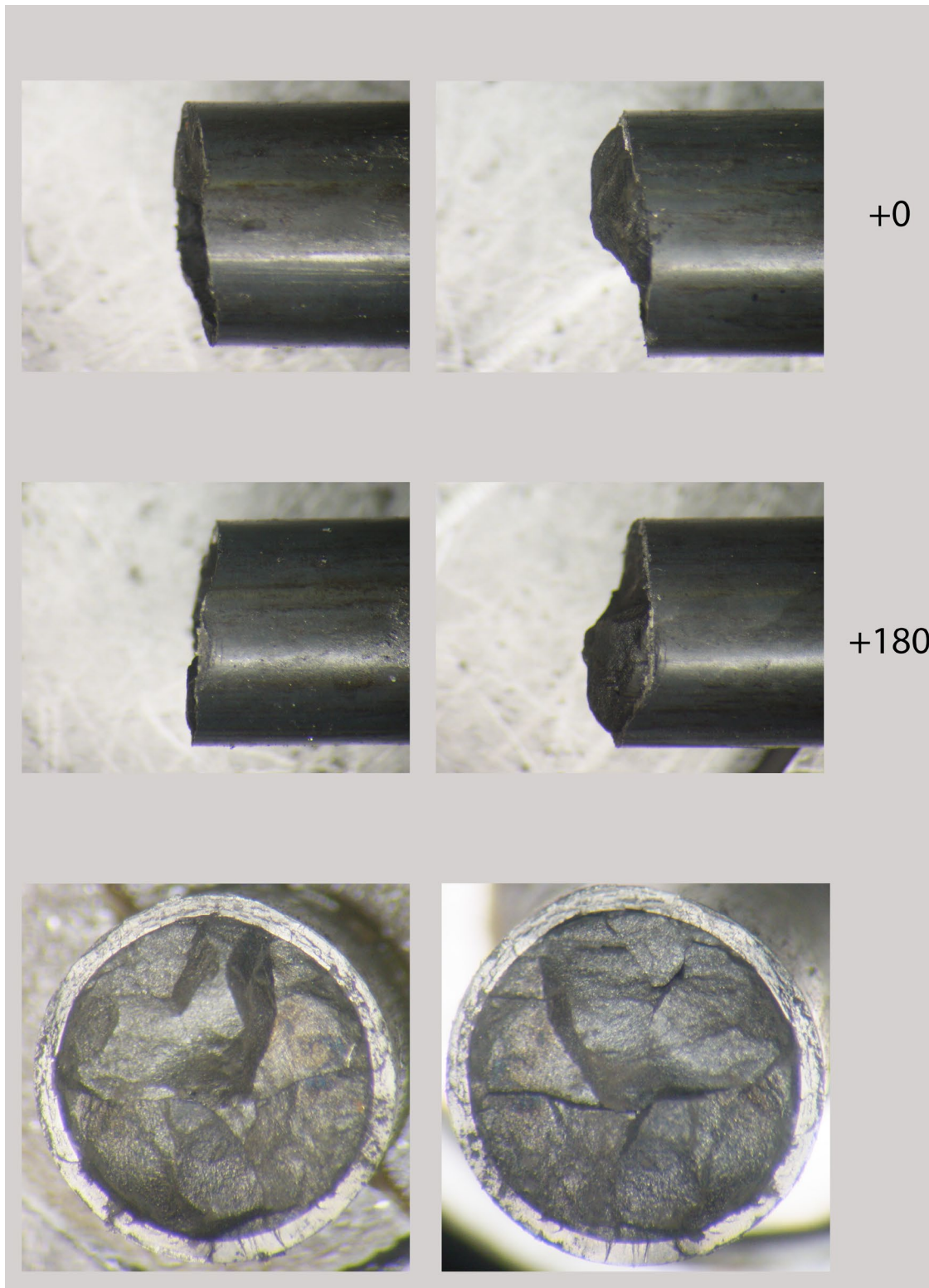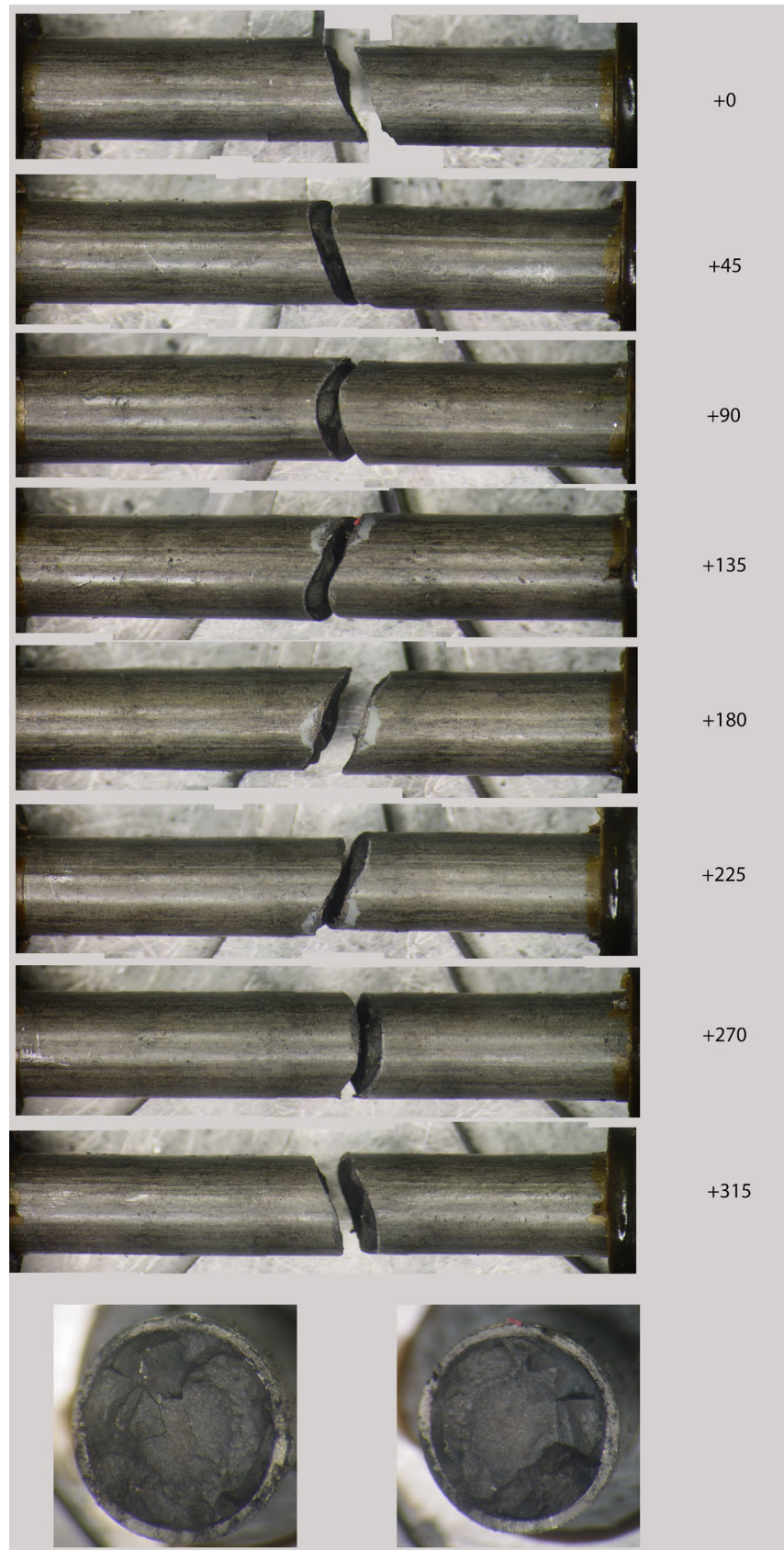**Figure F- 34. 3D8E14-2412-2565 post fatigue test condition.**
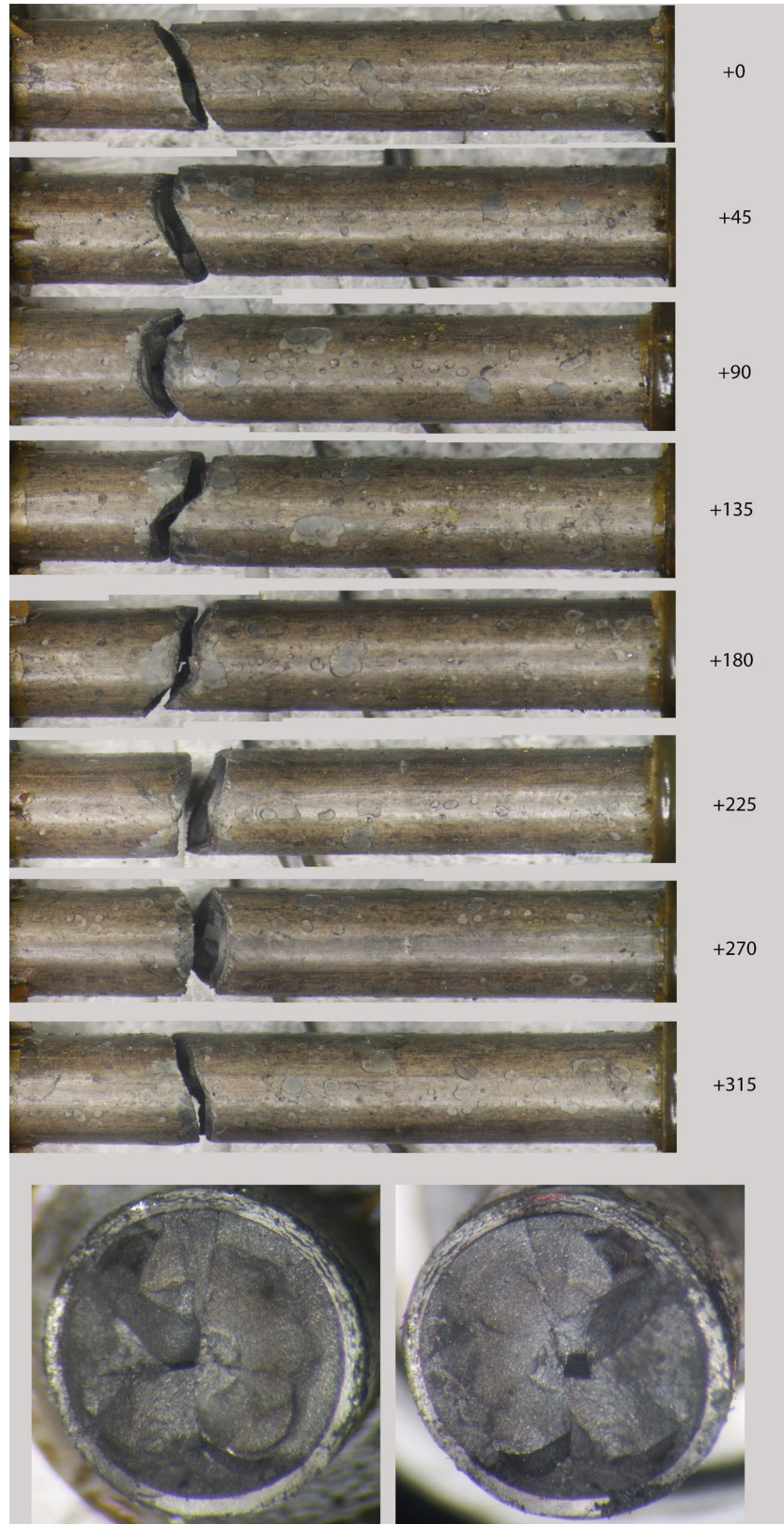
Figure F- 35. **3A1F05-3367-3520 post fatigue test condition.**
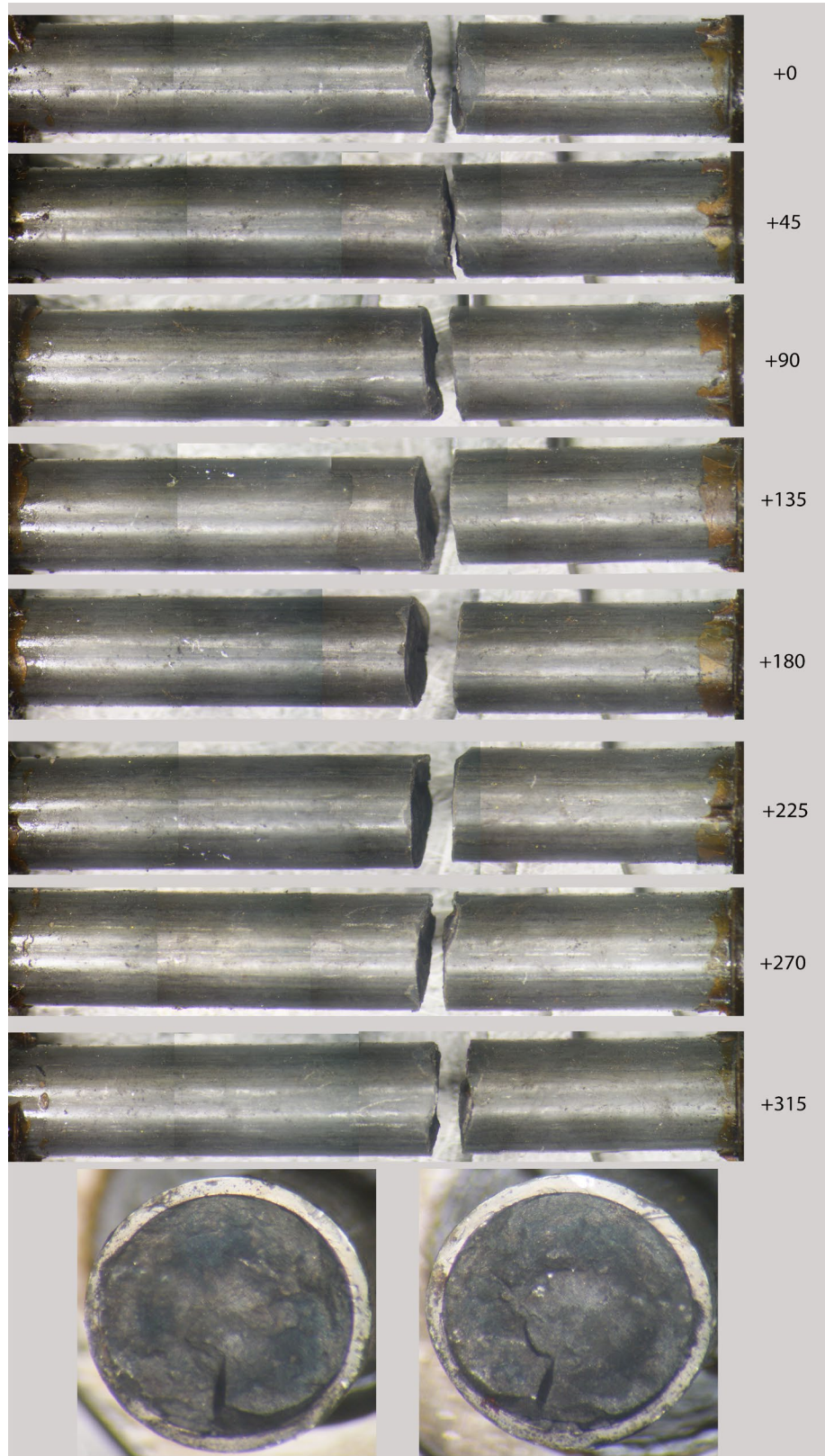
Figure F- 36. 3D8E14-1178-1331 post fatigue test condition.

F-8. CIRFT Cumulative Effects Fixture Development

Equipment for performing the cumulative shock tests, as shown in Figure F- 37, was developed and is currently being tested out-of-cell. The design incorporates an electromagnet and weight and uses gravity to deliver one or more impacts to the CIRFT specimen before fatigue testing. The parameters for the impact (e.g., impact load, number of impacts) have not yet been established. To help determine the necessary drop height, impactor weight, and impactor weight geometry for postulated normal condition impacts, a finite element model was developed for the impact system. The model and results are discussed in the following sections.

An electromagnet holds the impact weight at the appropriate height to generate the desired impact load.

A stepper motor is used to raise and lower the electromagnet.

Special fixturing is used to hold the horizontal CIRFT specimen in place, ensuring precise application of the shock to the specimen.

Figure F- 37. Cumulative shock fixture developed to apply a normal transport condition shock before fatigue testing.

F-8.1 Finite Element Modeling of the Cumulative Impactor

An impact analysis of the cumulative impactor was performed using a nonlinear dynamic FEA. Solid eight node elements and shell four node elements are used for all the models with which structure failure modes can be simulated during the impact.

The cumulative impactor model includes the impactor weight, a fuel rod test segment, and supports/restraints representing the lower bed of the impactor, as shown in Figure F- 38. The fuel rod is supported by guide blocks at both ends. The cumulative impactor weight was centered over the rod and at a variable height above the outer surface of the cladding. Several different impactor end geometries were evaluated, including:

    a. a grid strip wall with dimples (shown in Figure F- 38)
    b. a grid strip wall without dimples
    c. a rectangular weight only (the brown feature shown in Figure F- 38)
    d. a plate with dimples
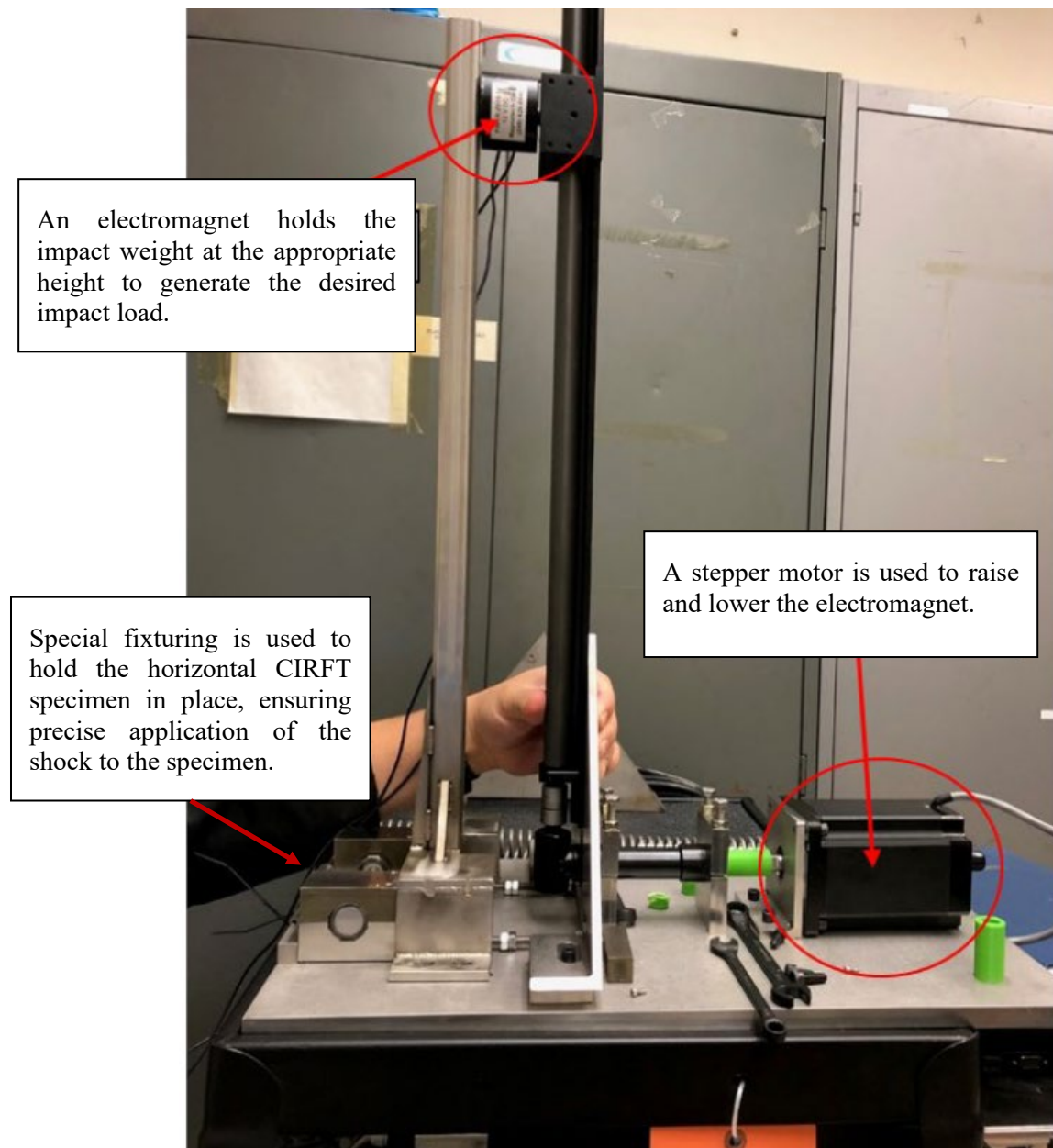   e. a plate without dimples

These studies are focused on understanding what the g-load on the rod segment is for various cumulative impactor conditions and is not related in any way to expected normal conditions of transport impacts to the fuel rods. Per Kalina et al [F14], the normal condition g-loads experienced during transport of the SNF are less than 15-g and more typically less than 3-g.

F-8.1.1 Finite Element Modeling Software

A nonlinear finite element model is developed using ANSYS Workbench. The dynamic analysis with time integration and contact configuration is used to solve the transient impact problem.

LS-DYNA, developed by Livermore Software Technology Corporation (LSTC), is a multipurpose explicit and implicit finite element program used to analyze the nonlinear response of structures. Its fully automated contact analysis and wide range of material models enable users worldwide to solve complex real-world problems. It is used by the automobile, aerospace, construction, military, manufacturing, bioengineering industries, and nuclear industries. LS-DYNA is optimized for shared and distributed memory on Unix, Linux, and Windows-based platforms, and it is fully qualified by LSTC. The code's origins lie in highly nonlinear, transient dynamic FEA using explicit time integration [F-15].

LS-DYNA has an extensive material library that includes metals, plastics, glass, foams, fabrics, elastomers, honeycombs, concrete and soils, viscous fluids, and user-defined materials.

LS-DYNA has been widely used in various applications including automotive crashworthiness and occupant safety, metal forming, aerospace (e.g., blade containment, bird strike, failure analysis), drop testing, nuclear shipping container design, metal cutting, earthquake engineering, offshore platform design, and sports equipment design.

Because impact is a transient structural dynamics problem that involves large deformation of solid structures and nonlinear material behavior, LS-DYNA is chosen to perform the impact analysis of the cumulative impactor.

F-8.1.2 Finite Element Model

Structurally insignificant features such as small curves and lines such as fillets and chamfers were omitted from the finite element model. The omitted features are small and are not expected to significantly influence

the structural response. The mesh element size near the impact zone was 0.5 mm, all other element sizes ranged from 0.5 to 2 mm. The cladding was modeled using linear shell elements.
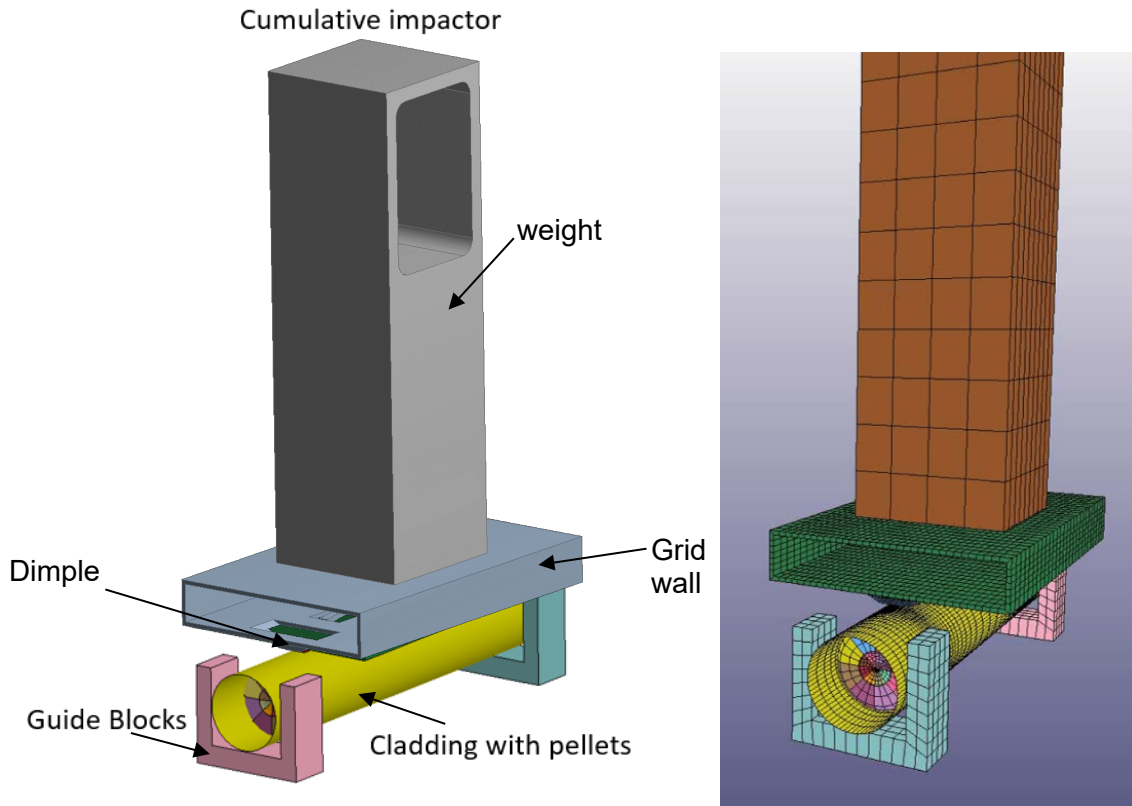
Figure F- 38. The cumulative impactor CAD model (left) and finite element model (right) include a rod segment with discrete pellets, guide blocks, and a weight with impact geometry.

The units and values used for the simulations are:

- mass, kg
- length, m
- time, s
- force, N
- stress, Pa
- energy, Joule
- density, kg/m^3
- elastic modulus, Pa

The cumulative impactor was modeled as separate parts with the surface-to-surface interfaces modeled using the bonded surface-to-surface connection. The surface-to-surface connections in the finite element model cannot deform but can break in accordance with the user-input stress criteria. The model uses various contacts to model the interaction between the elements. Automatic single-to-surface contact is an all-purpose contact used to model component interaction. Friction in LS-DYNA is modeled through the classic Coulomb friction model. In the cumulative impactor fuel rod segment model, contacts between the pellet-to-pellet and pellet-to-cladding contact were assigned a static friction coefficient of 0.95 and a dynamic

friction coefficient of 0.85 to simulate a relatively rigid system. The friction values are being investigated with other models; these values might not be entirely representative of the actual frictional contact but are considered acceptable for the purposes of this work.

F-8.1.3 Material Models

The cladding, spring, and dimples are modeled as Zirc-4, the pellets are modeled using a response profile similar to concrete, which is load-bearing in compression and has a lower strength in tension, and the cumulative impactor is modeled as stainless-steel. The pellets are modeled with a concrete material property as a surrogate for UO_2. The compression strength of the pellets was 15 MPa with an aggregate grain size of 25.4 mm.

To model the plastic deformation of metal materials, the LS-DYNA code needs the true stress–strain curve of the material. Up to the maximum point on the engineering stress–strain curve, a uniform elongation and a uniform area reduction occur. The minimum true stress–strain curve used is based on the model provided in the American Society of Mechanical Engineers (ASME) BPVC Sec. VIII Div. 2 Annex 3-D [F-16], which uses the minimum yield stress, the minimum ultimate tensile stress, and elastic modulus of the material at the specified temperature. The true stress-strain curves obtained with this model are valid up to the value of the true ultimate tensile stress at true ultimate tensile strain.

The LS-DYNA material model used in the analysis is the *MAT_PIECEWISE_LINEAR_PLASTICITY, also known as *MAT_024*. This material model prompts user to specify the elastic modulus, Poisson's ratio, yield stress, and failure strain of the material. When the calculated element's plastic strain reaches the specified failure strain, the material has failed, and the element is deleted from the analysis. Additionally, the effective stress vs. plastic strain curve must be entered as a *DEFINE_CURVE entry.

Following the ASME model, a true stress–strain curve was developed for stainless steel and Zirc-4 using the minimum yield strength, minimum ultimate tensile strength, and elastic modulus of the material in Table F- 8 [F-17]; the curve is shown in Figure F- 39. Before the true stress–strain curve was input to LS-DYNA, the elastic portion of the strain was subtracted from the total strain to develop the effective plastic strain used by LS-DYNA.

Table F- 8. Cumulative impactor model minimum material properties.

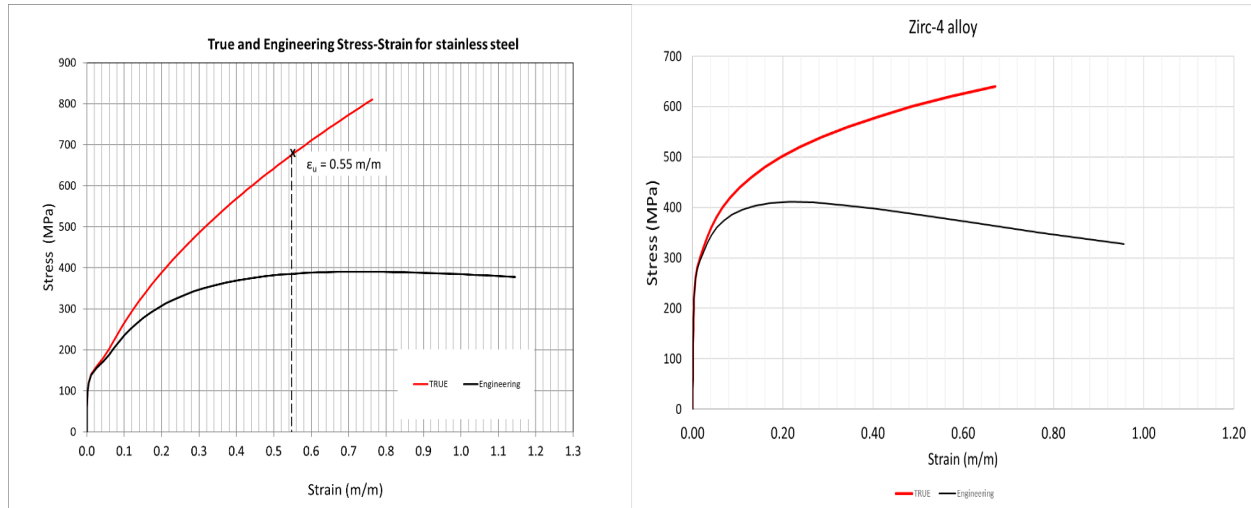|		Material Properties		
Material	Minimum yield stress (MPa)	Minimum ultimate stress (MPa)	Elastic modulus (GPa)	Reference
304	106	392	172	[F-16, F17]
Zirc-4	241	413	99.3	[F-16, F-17]

Figure F- 39. 304 stainless steel (left) and Zirc-4 (right) true stress-strain curves used.

F-8.1.4 Initial Conditions, Boundary Conditions and Load Cases

All simulations were completed using room temperature material properties. A gravity load of 9.81 m/s^2 was applied to all components in the finite element model. The guide rods were constrained in all three directions using the *BOUNDARY_SPC_SET keyword. The fuel rod segment was placed on the guide blocks with full frictional contact.

F-8.1.5 Load Cases

Impact of the weight was studied using nine load cases, as listed in Table F- 9, for each of the impactor end geometries. Load cases 1–4 correspond to a maximum cumulative impactor weight of 0.11 kg with increasing drop height from 0.15 to 0.61 m (0.5 to 2.0 ft). Load cases 5–7 correspond to a 25% reduction in the cumulative impactor weight with increasing drop height. The cumulative impactor mass for load case 8 was reduced by 50% when compared with load case 1, and the drop height was 0.15 m (0.5 ft). Finally, for load case 9, the mass for the cumulative impactor was reduced by 75% when compared with load case 1, and the drop height was 0.15 m (0.5 ft).

Table F- 9 Cumulative tester FEA load case summary.

Load case	Impactor mass (g)	Impactor height (m)
1	0.107	0.15
2	0.107	0.30
3	0.107	0.46
4	0.107	0.61
5	0.080	0.15
6	0.080	0.30
7	0.080	0.46
8	0.053	0.15
9	0.027	0.15

F-8.2 Results, Discussion, and Conclusions from the Cumulative Effects Fixture Modeling

The analysis focused on determining the g-load applied to the cladding when subjected to an impact from the cumulative impactor. The cladding g-load for each load case was extracted from the analysis and was plotted as a function of time. The system can dissipate the impact energy in three ways: 1) rebound/deflection of the impactor, 2) bending deflection of the target rod segment, and 3) absorption into the rod cladding and pellets and supporting end blocks. End configurations (described in section F-8.1) (a) and (b) resulted in a lot of rebound and the lowest g-load impacts. The concentrated load application in end configuration (c) resulted in rod segment bending, but the g-loads on the rod segment are extremely high. The plate type end configuration ([d] and [e]) resulted in high shear loads on the rod segment near the guide blocks that are not considered representative of the target g-load of <15g.

None of the combinations resulted in a g-load below 20-g. For example, the results from impactor end configuration (d), plate with dimples, is provided. The impactor-applied g-load as a function of time is provided in Figure F- 40 for load cases 1–4 and in Figure F- 41 for load cases 5–9. For this impactor geometry, the initial impact takes less than 0.3 ms, after which the weight is rebounded. The g-load on the rod during the impact ranges from 781 to 3,298-g, as listed in Table F- 10. Load case 4 has the highest drop height and heaviest weight and it resulted in the maximum g-load because it had the largest potential energy when compared with the other load cases. Load case 1, 8, and 9 resulted in a cladding g-load less than 800-g's. All load cases resulted in g-loads greater than 500-g's with multiple shock waves on the cladding and localized plastic strain on the impactor weight dimples, as shown in Figure F- 42.
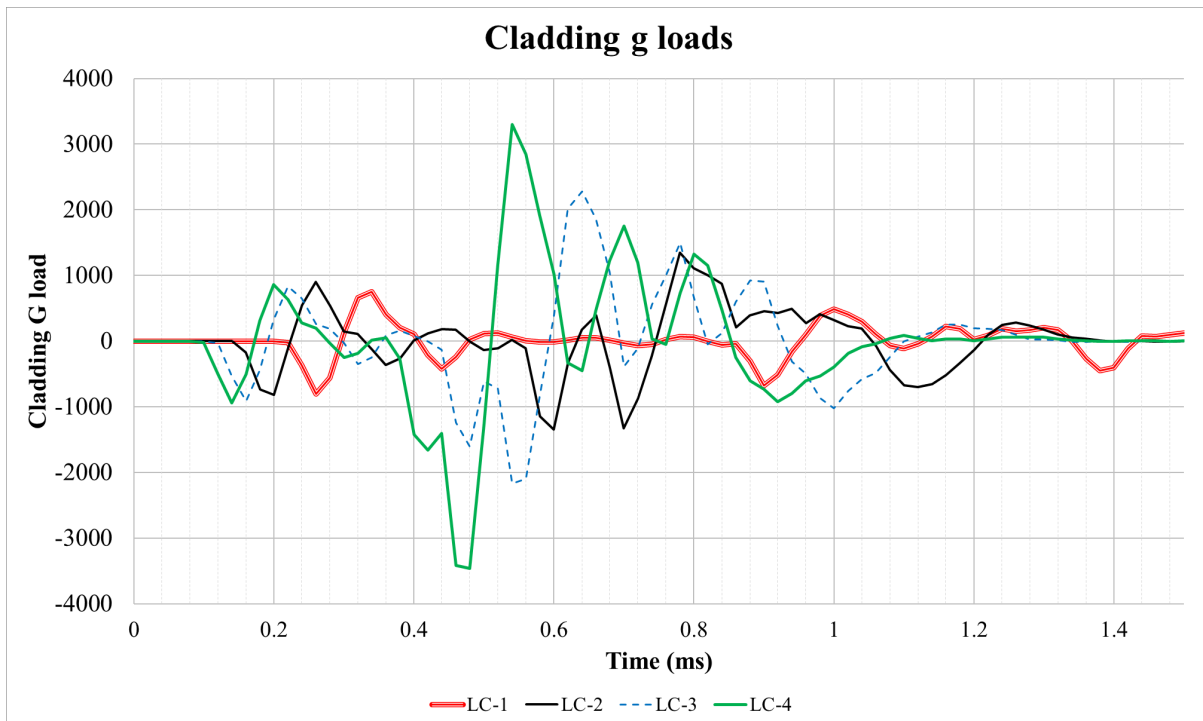
Figure F- 40. Impactor end configuration (a) results for load cases 1–4.

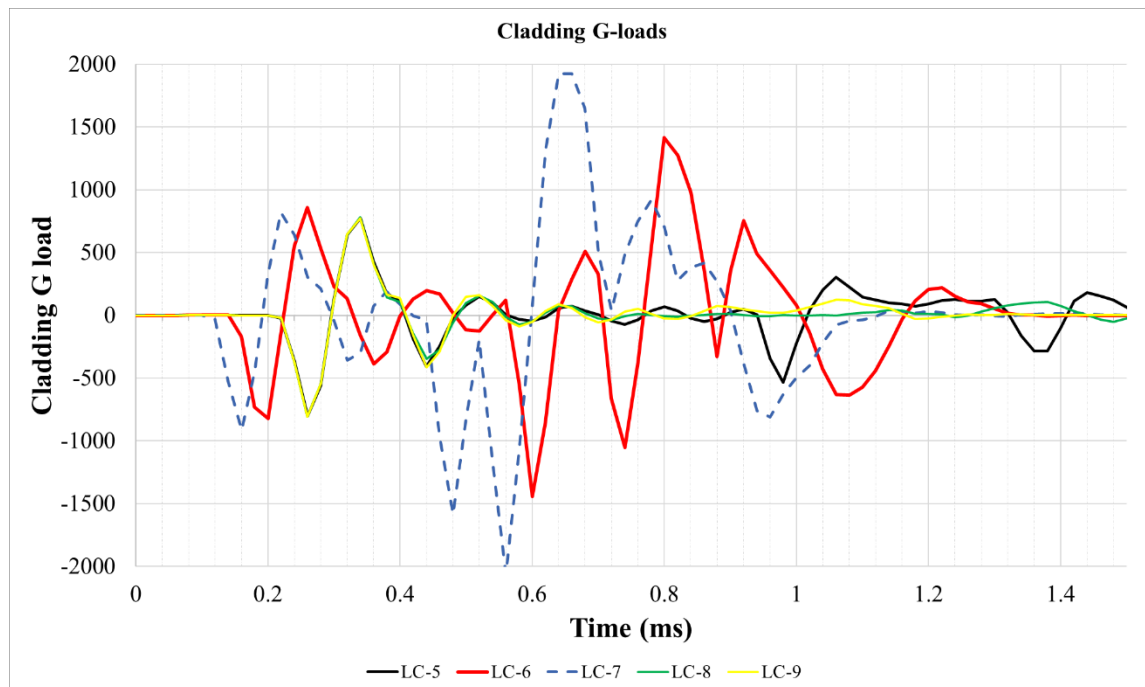**Figure F- 41. Impactor end configuration (a) results for load cases 5–9.**

Table F- 10. Summary of fuel rod maximum g-load during impact with end configuration (a).

Load case	Cladding maximum g-load
LC-1	754
LC-2	1,344
LC-3	2,279
LC-4	3,298
LC-5	774
LC-6	1,414
LC-7	1,925
LC-8	781
LC-9	773

Effective Plastic Strain

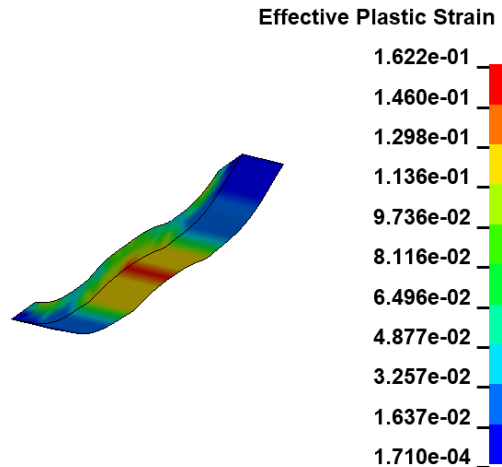|	
1.622e-01	
1.460e-01	
1.298e-01	
1.136e-01	
9.736e-02	
8.116e-02	
6.496e-02	
4.877e-02	
3.257e-02	
1.637e-02	
1.710e-04	

Figure F- 42. Plastic strain occurred on the dimples for impactor end configuration (a).

In addition to the permanent deformation of the impactor end dimples, configuration (a) also resulted in large rebound and fluttering of the grid wall portion of the impactor. Since these effects would produce uncontrolled variation in the impacts, this configuration was not usable for the intended purpose.

Based on the FEA, the main reason that the target g-load range cannot be achieved has nothing to do with the impactor itself. Rather, the problem is that the target rod segment is very stiff. It is necessary to prepare the segment for CIRFT testing by installing the heavy dogbone grips on each end. Only 50 mm of segment length is exposed for impact, as shown in Figure F- 43. The dogbone provides a very stiff target that does not deflect in bending and any impact will result in a high g-load, even with very low drop height, low impactor weight and a soft impactor end configuration such as the dimples with grid wall. Given the dogbone as the target, low g-load impacts are not possible with the current fixture.

Figure F- 43. CIRFT dogbone.

F-8.3 Verification of FEA Results Using the Cumulative Effects Fixture

Physical tests using the cumulative effect fixture were completed as a verification of the FEA. A CIRFT dogbone surrogate with stainless-steel cladding and ceramic pellets was constrained in the specimen holder, as shown in Figure F- 44. Various impactors with masses ranging from 355 to 47 g were used for the tests. These impactors had end geometries designed to mimic grid dimples, but they were solid, as shown in Figure F- 45.
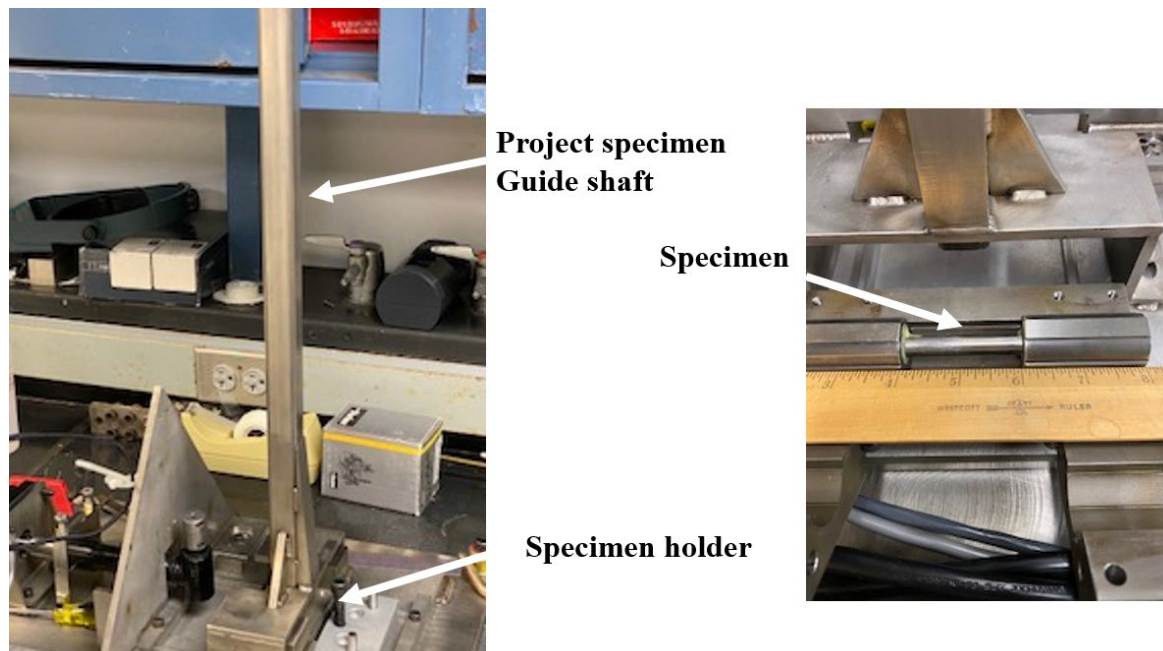

Project specimen
Guide shaft

Specimen

Specimen holder

Figure F- 44. Physical test configurations with the cumulative effects fixture.

Figure F- 45. Impactors used in the physical tests.

To record the maximum g-load on the specimen, a single axis accelerometer was mounted on the specimen with epoxy adhesive. The maximum recordable load for the accelerometer used is 1,100-g. The 85-g projectile was dropped from two different heights: 127 and 25 mm. The mounted accelerometer on the specimen recorded its maximum acceleration of 1,100-g for all tests, indicating a load greater than 1,100-g for all test. Some attempts were made to reduce the impact load by adding compliant layers to the impact surfaces, but this was unsuccessful.

Because there was not an accelerometer available that ranged to higher loads, the results were well beyond the target g-loads, and the information circumstantially confirmed the FEA, no further investigations were completed.

REFERENCES

[F-1].   *High Burnup Dry Storage Cask Research and Development Project: Final Test Plan*, contract no. DE-NE-0000593, Electric Power Research Institute, Palo Alto, California (2014).

[F-2].   S. Saltzstein et al., *Visualization of the High Burnup Spent Fuel Rod Phase 1 Test Plan*, SAND2018-8042-O (2018).

[F-3].   R. A. Montgomery et al., *Post-Irradiation Examination Plan for High Burnup Demonstration Project Sister Rods*, SFWD-SFWST-2017-000090 ORNL/SR-2016/708, Oak Ridge National Laboratory (2016).

[F-4].   J.-A. Wang and H. Wang, *FY 2017 Status Report: CIRFT Data Update and Data Analyses for Spent Nuclear Fuel Vibration Reliability Study, Revision 1*, ORNL/SPR-2017/521, SFWD-SFWST-2017-000030/R1 (2017).

[F-5].   J.-A. Wang and H. Wang, *Mechanical Fatigue Testing of High Burnup Fuel for Transportation Applications*, NUREG/CR-7198/R1 (2017).

[F-6].   R. A. Montgomery et al., *Sister Rod Nondestructive Examination Final Report*, SFWD-SFWST-2017-000003 Rev. 1 (M2SF-17OR010201021) / ORNL/SPR-2017/484 Rev. 1 (ORNL/SPR-2018/801), Oak Ridge National Laboratory (2019).

[F-7].   J.-A. Wang and H. Wang, *FY 2017 Status Report: CIRFT Data Update and Data Analyses for Spent Nuclear Fuel Vibration Reliability Study, Revision 1*, ORNL/SPR-2017/521, SFWD-SFWST-2017-000030/R1 (2017).

[F-8].   J.-A. Wang and H. Wang, *Mechanical Fatigue Testing of High Burnup Fuel for Transportation Applications*, NUREG/CR-7198/R1 (2017).

[F-9].   W. J. O'Donnell and B. F. Langer, "Fatigue Design Basis for Zircaloy Components," *Nuclear Science and Engineering* 20 (1964): 1–12.

[F-10]. P. McConnell et al. *Normal Conditions of Transport Truck Test of a Surrogate Fuel Assembly*, SAND2014-20495/FCRD-UFD-2014-000066, Revision 0.1, Sandia National Laboratory, December 2014.

[F-11]. K. Geelhood et. al. "Modeling Structural Loading of Used Nuclear Fuel under Conditions of Normal Transportation," *Ceramic Materials for Energy Application IV*, The American Ceramic Society, 2015.

[F-12]. J.-A. Wang and H. Wang, *FY 2017 Status Report: CIRFT Data Update and Data Analyses for Spent Nuclear Fuel Vibration Reliability Study, Revision 1*, ORNL/SPR-2017/521, SFWD-SFWST-2017-000030/R1 (2017).

[F-13]. J.-A. Wang and H. Wang, *Mechanical Fatigue Testing of High Burnup Fuel for Transportation Applications,* NUREG/CR-7198/R1 (2017).

[F-14]. E. A. Kalinina et al., *Data Analysis of ENSA/DOE Rail Cask Tests*, SFWD-SFWST-2018-00049/ SAND2018-13258R (2018).

[F-15]. LS-DYNA. "LS-DYNA." http://www.lstc.com/products/ls-dyna, (9/1/2020).

[F-16]. ASME BPVC Sec VIII Div. 2 *Annex 3-D Rules for Construction of Nuclear Facility Components*, 2013

[F-17]. ASME BPVC Sec II, Part D *Rules for Construction of Nuclear Facility Components*, 2013.